LIÈGE université
Urban & Environmental Engineering

LIÈGE université

Quantitative interpretation of geophysical data in anthropogenic waste deposits and disposal sites for resource recovery and remediation

by

Itzel Isunza Manrique

A thesis submitted in partial fulfillment of the requirements for the degree of Doctor of Philosophy (PhD)

Faculty of Applied Sciences, Urban and Environmental Engineering

University of Liege

Promoter:
Prof. Nguyen Frédéric, University of Liege

Jury:
Prof. Dassargues Alain (President), University of Liege
Dr. Caterina David, University of Liege
Prof. Hermans Thomas, Ghent University
Prof. Van De Vijver Ellen, Department of Environment and Spatial Development at the Government of Flanders and Ghent University
Prof. Garré Sarah, ILVO Instituut voor Landbouw, Visserij en Vodingsonderzoek and KU Leuven

August 2023

ABSTRACT

The increasing generation of anthropogenic waste highlights the need to integrate a sustainable dynamic management that evolves with time according to the site context and needs. This management can range from the development of an interim use of a landfill surface to ultimately support remediation strategies that aim for the prevention (or reduction) of pollutants into the environment and the reduction of waste volumes. Simultaneously, the need of critical raw materials, metals and minerals enhance the need to find alternative sources of materials. Therefore, remediation strategies that aim to mitigate environmental risks and reduce the amount of waste, can also be tailored to enhance secondary resource recovery. To this aim, it is crucial to have in-depth knowledge of these residues such as the composition, physical properties and quantities.

Geophysical methods have proved useful to characterize landfills and waste deposits in terms of geometry delineation, zonation and volume estimation, to infer the waste composition and for monitoring. However, the heterogeneity that can be found in the waste materials and the dynamic processes that may occur within them can lead to complex data acquisition and processing as well as complex bulk geophysical signatures that can be challenging to interpret.

This contribution aims first, to present a state of the art on the applicability and limitations that several surface geophysical methods have, for the investigation of different types of landfills and in particular metallurgical residues. We discuss its applicability focusing on investigations that aim to provide decision support tools in the dynamic management of these sites. Based on these studies, we observed the need of: 1) more quantitative interpretation methodologies that integrated associated uncertainties were needed for more reliable characterization of landfills and deposits, and 2) integrated methodologies for a more comprehensive characterization of metallurgical residues in terms of metallic concentrations or mineral variations, linking laboratory and field measurements. This contribution then aims to address these issues.

First, we present a probabilistic approach to classify different types of materials or "categories" observed in borehole logs using several data sources: inverted resistivity and chargeability values, and the position of the boreholes. Using Bayes' rule and permanence of ratios, we computed joint conditional probabilities of each category in the whole domain of the inverted models. The probabilities are then compared to derive a classification model that integrates the associated uncertainty. Additionally,

we assess the classification performance of the probabilistic approach and compare it with the machine learning algorithm of multilayer perceptron (MLP). We tested both approaches using different data sources and changing the number of boreholes and its distribution in a synthetic case study based on a complex anthropogenic-geologic scenario. Lastly, we compare both approaches using real data from an old heterogeneous landfill.

Then, we present a methodology that integrates geochemical and geophysical laboratory measurements to interpret geophysical field data in terms of the geochemical composition. The final aim is to estimate volume(s) of different types of materials for potential resource recovery. This methodology is illustrated in a slag heap composed of byproducts from former iron and steel production where we carried out a 3D acquisition using electrical resistivity tomography and induced polarization. In the lab, the same methods were applied on samples collected across the site (geophysical-based sampling), along with additional spectral induced polarization and X-ray fluorescence analysis. Based on the lab measurements, groups of different chemical composition were identified. We then used the inverted resistivity and chargeability collocated with the samples to fit 2D kernel density estimation functions for each group, and derived the corresponding joint conditional probabilities in the whole field domain. Then a 3D classification model was derived by comparing the joint conditional probabilities estimated for each group. Associated uncertainties are then integrated in the classification and in the estimation of volumes.

Both the probabilistic approach applied in a heterogeneous landfill and the integrated methodology illustrated in a slag heap represent alternatives for a more quantitative geophysical (post-inversion) interpretation that integrate associated uncertainties. These methodologies can be extended to integrate geophysical data from multiple methods or/and three dimensions, as well as different types of geochemical laboratory measurements, based on which the interpretation can be developed.

RÉSUMÉ

La production progressive de déchets anthropiques met en évidence la nécessité d'intégrer une gestion dynamique durable qui évolue dans le temps en fonction du contexte et des besoins du site. Cette gestion peut couvrir le développement d'une activité provisoire de la surface d'une décharge et, en dernier ressort, soutenir des stratégies d'assainissement visant à prévenir (ou à réduire) les polluants dans l'environnement et à réduire les volumes de déchets. Simultanément, la demande de matières premières critiques, de métaux et de minéraux renforce la nécessité de trouver des sources alternatives de matériaux. Par conséquent, les stratégies d'assainissement qui visent à mitiger les risques environnementaux et à réduire la quantité de déchets peuvent également être adaptées pour promouvoir la récupération des ressources secondaires. À cette fin, il est essentiel d'avoir une compréhension détaillée de ces résidus, notamment de leur composition, de leurs propriétés physiques et de leurs quantités.

Les méthodes géophysiques se sont avérées utiles pour caractériser les décharges et les dépôts de déchets en termes de délimitation de la géométrie, de zonage et d'estimation du volume, pour déduire la composition des déchets et pour la surveillance. Cependant, l'hétérogénéité que l'on peut trouver dans les déchets et les processus dynamiques qui peuvent s'y produire peuvent générer une acquisition et un traitement complexes des données ainsi que des signatures géophysiques complexes en volume dont l'interprétation peut poser des problémes.

Cette contribution vise tout d'abord à présenter un état de l'art sur l'applicabilité et les limitations de plusieurs méthodes géophysiques de surface pour l'étude de différents types de décharges et en particulier des résidus métallurgiques. Nous discutons de l'applicabilité de ces méthodes dans le cadre d'études visant à fournir des outils d'aide aux décisions pour la gestion dynamique de ces sites. Sur la base de ces études, nous avons observé le nécessité de: 1) des méthodologies d'interprétation plus quantitatives qui intègrent les incertitudes associées sont nécessaires pour une caractérisation plus fiable des décharges et des dépôts, et 2) des méthodologies intégrées pour une caractérisation plus complète des résidus métallurgiques en termes de concentrations métalliques ou de variations minérales, reliant les mesures en laboratoire et sur le terrain. Cette contribution vise à répondre à ces questions.

En premier lieu, nous présentons une approche probabiliste pour classifier les différents types de matériaux ou "catégories" observés dans les logs de forage en utilisant plusieurs sources de données : les valeurs inversées de résistivité et de

chargeabilité, et la position des forages. En utilisant le théorème de Bayes et la permanence des ratios, nous avons calculé les probabilités conditionnelles conjointes de chaque catégorie dans l'ensemble du domaine des modèles inversés. Les probabilités sont ensuite comparées pour obtenir un modèle de classification qui intègre l'incertitude associée. Nous validons cette approche en utilisant des données synthétiques dans un scénario anthropique-géologique complexe et en utilisant des données réelles provenant d'une ancienne décharge hétérogène.

Ensuite, nous présentons une méthodologie qui intègre des mesures géochimiques et géophysiques en laboratoire afin d'interpréter les données géophysiques de terrain en termes de composition géochimique. L'objectif final est d'estimer le(s) volume(s) de différents types de matériaux pour une évaluation de la récupération potentielle des ressources. Cette méthodologie est illustrée dans un terril composé de sous-produits de l'ancienne production de fer et d'acier où nous avons effectué une acquisition 3D en utilisant la tomographie de résistivité électrique et la polarisation induite. En laboratoire, les mêmes méthodes ont été appliquées à des échantillons prélevés sur le site (échantillonnage basé sur la géophysique), en plus de la polarisation induite spectrale et de l'analyse par spectrométrie de fluorescence des rayons X. Sur la base des mesures effectuées en laboratoire, des groupes de composition chimique différente ont été identifiés. Nous avons ensuite utilisé la résistivité et la chargeabilité inversées colocalisées avec les échantillons pour ajuster des fonctions de l'estimation par noyau (KDE en anglais) en 2D pour chaque groupe, et nous avons dérivé les probabilités conditionnelles conjointes correspondantes dans l'ensemble du domaine du terrain. Un modèle de classification 3D a ensuite été dérivé en comparant les probabilités conditionnelles conjointes estimées pour chaque groupe. Les incertitudes associées sont ensuite intégrées dans la classification et dans l'estimation des volumes.

L'approche probabiliste appliquée à une décharge hétérogène et la méthodologie intégrée illustrée dans un crassier représentent des alternatives pour une interprétation géophysique (post-inversion) plus quantitative qui intègre les incertitudes associées. Ces méthodologies peuvent être étendues pour intégrer des données géophysiques provenant de méthodes multiples et/ou en trois dimensions, ainsi que différents types de mesures géochimiques en laboratoire, sur la base de laquelle, l'interprétation peut être développée.

Acknowledgments

First, I would like to thank Frédéric Nguyen for giving me the opportunity to participate in a PhD combined with a job experience of working in two multidisciplinary EU projects. It was an enriching experience that allowed me to meet several people from academia and industry and to get to know both perspectives and objectives. This experience also allowed me to travel around to nice places and to participate in conferences, workshops, meetings and several field surveys. I am deeply grateful to Fred for all the help, guidance and his amazing coolness, in particular during these last months. In addition, thanks to the jury for taking the time to read this thesis and for their help in different moments of the development of this PhD.

I would also like to acknowledge the funding provided by the program of Interreg North-West Europe and the Walloon Region for RAWFILL and NWE-REGENERATIS projects. I thank all projects partners and all the colleagues for the agreeable moments and nice experiences we shared.

When I arrived to the university I worked with Gael Dümont, who trusted me to work with the instruments, the data, reports and other administrative tasks. I am very grateful for this because it allowed me to learn about the data acquisition, processing, visualization and interpretation oriented to the short-to-mid term objectives needed as inputs for the subsequent work of other project partners. I thank the colleagues of the Applied Geophysics- UEE department, in particular to Tanguy Robert for always been willing to help. I also thank David for all the help, kindness and all the great experiences we shared during the fieldwork (most of which happened during winter, lovely season), nice conferences and so many meetings along the projects.

I am deeply grateful to Thomas Hermans for helping me when I was completely lost and frozen in the PhD. I thank Thomas for the continuous support during all this time, quickly answering my mails, giving me feedback, sharing his knowledge, making suggestions and for his active participation in the PhD follow-up meetings we had.

I am also greatly thankful to Ellen Van De Vijver for the support during the PhD and for sharing her knowledge during the work we carried out together in a couple of

field surveys and gathering material for the review on the use of geophysics in landfills. It was an academically enriching experience where I could learn about the main challenges of applying geophysical methods for the characterization of landfills and also the type of information expected by site managers/owners from the geophysical data interpretations. In addition to the mentorship, I deeply thank Ellen for caring about the individual well-being and enhance its importance for the development of a healthy PhD. I greatly appreciate the friendship that we could build.

I am deeply grateful to my friends Tamara and Nico for all their continuous support since I arrived in Liege and for sharing beautiful moments (next to their family) with me. I also thank Cristina and Walter for all their help and all the funny moments and incredible tasty meals we shared. More than once they made me feel at home. I would like to thank Jorge and Lorena for their help especially at the beginning of the PhD. I deeply thank Jorge for always been willing to help and to teach in a kind and helpful way. I thank my friends Edmundo, Laura, Tom and David for all their support and the enriching, funny moments we spent together. All of them made my stay in Liege more enjoyable.

I am deeply grateful with the colleagues from Metis, Sorbonne Université, in particular to Ludovic Bodet for sharing his office with me during all this time. I thank Damien Jougnot and Roger Guérin for their help and feedback with the manuscripts of Duferco and the critical review on geophysical methods respectively, I also thanks the kindness they always showed. I would also like to thank Jean-Marie Mouchel for the talks and his friendliness.

I am very grateful to my friends Bénédicte Sabatier and Jean-Louis for all their help, for giving me a warm welcome in Paris, and our lunch gatherings that taught me a bit about French gastronomy. I also thank my colleagues and friends Ramon, Orsi, Jose, Marie, Mariangeles, Bertille and Audre for welcoming me, I am very pleased to have met all of you. I would like to especially thank Marco, Aida and Julio, thanks for accompanying me through these almost two years, for your help, support and all the funny moments and experiences. I value our friendship and I am going to miss you and our talks during the crêpe/ice-creams afternoons.

Finally, I would also like to thank Carlos for his endless support and cooking, in particular during the last six months that have been full of greatly special findings. I am deeply grateful for sharing our lives together and for building this relationship everyday with love, patient and joy. I am happy to keep discovering with you these new experiences and all the new places. Mis agradecimientos más especiales son para mi familia, por haberme apoyado sin interrupción a la distancia durante todos estos años. Por su paciencia y consejos brindados en la infinidad de las llamadas

y mensajes que realizamos. En particular agradezco a mi mamá todo su apoyo y el arduo trabajo que siempre ha realizado, el cual nos permitió tener acceso a más oportunidades. Agradezco a mi abuela por todo lo que ha hecho por nosotros, a mi abuelo, mis hermanos y mi querido sobrino por ser fuente de alegría.

Contents

Chapter 1

Introduction

In Europe there are between 150,000 and 500,000 landfills from which, approximately 90 % predate the EU Landfill Directive of 1999, i.e., they are non-sanitary landfills. As most of these sites lack the environmental protection infrastructure, in a "doing nothing" scenario, they will eventually need a costly aftercare or a costly remediation depending on the regulations of each country. Furthermore, around 80 % of these landfills contain municipal solid waste while the rest is mostly composed of specific industrial residues (Hernández Parrodi et al., 2019b). With this motivation the concepts of landfill mining, enhanced landfill mining and dynamic landfill management emerged as an alternative to develop a vast number of activities mostly focusing on interim use, and ultimately resource recovery (materials and energy) and land restoration combined with a sustainable remediation.

More recently, the increasing need to find critical raw materials drives to also revisit the residues generated by the primary mining and metal processing industry, i.e., extractive waste (Machiels et al., 2022). First, the mining sites predating the EU Extractive Waste Directive in general lack environmental protection engineering and therefore may pose environmental/human health risks. Secondly, the need of raw materials and minerals emphasize the recent challenges faced by the mining industry, e.g., inaccessibility of deposits (Žibret et al., 2020). Consequently, the exploration of past mining and metallurgical sites offers an opportunity to mitigate the situation, integrating resource-recovery with sustainable remediation strategies in line with a circular economy.

The development of the above-mentioned strategies requires a reliable characterization and monitoring of landfills and deposits that allows the assessment of resource recovery potential. Conventional characterization techniques are based on excavations of boreholes, trenches or pits that first, may not capture the heterogeneity of a landfill and secondly, may pose additional environmental or human health risks. In this context, advances in non-invasive geophysical methods for exploration

have proved useful to identify anthropogenic wastes and associated contamination, delineate their vertical and lateral extension, image zonations within the residues, and infer in its composition. However, the strong varying physical properties that anthropogenic residues can present, together with the dynamic processes that can be developed within them, may further add ambiguity to the geophysical data interpretation (Van De Vijver et al., 2020, 2021). Therefore, more quantitative and/or high-resolution final results can be challenging even in presence of ground truth data.

The objective of this thesis is to contribute to the characterization of solid waste landfills and deposits using surface geophysical methods. In particular a quantitative characterization that can complement decision support tools to improve the management of these landfills, e.g., volume quantification. First we carried out a literature review of the geophysical methods and methodologies used in the characterization of different types of residues, targeting a broad range of applications. Based on this, we identified the need for more quantitative approaches for the interpretation of the data that take into account the associated uncertainties. Therefore, we introduce two approaches based on probability theory, that aim to interpret geophysical data quantitatively at field scale. In general, the interpretations are based on 1) a calibration between the geophysical field data and either observations or laboratory measurements from an optimized sampling and 2) a probabilistic classification in the whole domain of the geophysical coverage.

This work has been conducted within the framework of two multidisciplinary projects founded by Interreg North-West Europe and the Walloon Region, which were focused on different types of solid waste. The project RAWFILL (supporting a new circular economy for RAW materials recovered from landFILLs) was mostly focused on municipal solid waste landfills. The objective of RAWFILL was to create tools such as an enhanced inventory and decisions/prioritization tools to allow the owners of the landfills make economically informed decisions while launching a landfill mining project [1]. The project NWE-REGENERATIS (REGENERATion of past metallurgical Sites and deposits through innovative circularity for raw materials) is focused on former metallurgical sites and residues of the associated production. The objective of NWE-REGENERATIS is to valorize and potentially recover valuable materials while regenerating former metallurgical sites and deposits. It combines geophysical imaging with efficient material recovery processes and tools such as an harmonized inventory structure and an algorithm of artificial intelligence

[1] Project partners of RAWFILL were: Public Waste Agency of Flanders (OVAM), Bergischer Abfallwirtschaftsverband (BAV), SAS LES CHAMPS JOUAULT, Université de Liège, Natural Environment Research Council (NERC) – British Geological survey (BGS), Cleantech Flanders/VITO and ATRASOL

to assess the potential resource recovery [2]. Both projects largely promote the use of geophysical methods as alternative and sustainable characterization methods as compared to only intrusive conventional methods, i.e., excavations. This thesis is focused overall on the solid waste sector, which has been an evolving concept and includes types of residues such as household-derived, construction and demolition waste (CDW) and residues generated by the industry (Memon, 2010).

During the development of RAWFILL several types of sites were investigated: dumps, semi-engineered and engineered landfills composed of (or a combination of) municipal solid waste (MSW), industrial waste and ashes from MSW incineration. On the other hand, NWE-REGENERATIS is focused on metallurgical residues, where more than 6 sites have been investigated. The sites comprise deposits of slags (iron/steel production), residues from zinc production, slags from antimony and lead production, etc. During these investigations we observed that the use of surface geophysical methods for the characterization of landfills and waste deposits can be challenging at different stages of the investigation: data acquisition, data processing and data interpretation. Data acquisition of one or more methods can be limited by the topography, vegetation and infrastructure of the landfill, e.g., presence of plastic geomembrane. Data processing and interpretation can be challenging in these environments, as anthropogenic residues can have widely varying physical properties which can be very different from the properties of geological environments. In addition, most of the landfills are not composed of exclusively one type of material, but heterogeneous mixtures of waste deposited at different periods of time. This leads to a highly complex matrix of materials where variable and dynamic processes may take place (Van De Vijver et al., 2020, 2021). As a result, it is crucial to calibrate the geophysical data with ground truth data to mitigate the ambiguities and to conduct more accurate interpretations that integrate associated uncertainties.

To mitigate the above-mentioned challenges, we followed the general workflow shown in Figure 1.1, which ranges from the geophysical survey design to the final interpretation. The first step is to design an optimized geophysical survey according to the objective of the investigation (Isunza Manrique et al., 2019b). The geophysical survey is design on the basis of 1) the historical reports and all available information, 2) site visits to assess the state of the vegetation, materials on surface such as CDW, roughness of the surface, topography, etc., and 3) the objective of the investigation. While the final aim of the geophysical characterization of NWE-REGENERATIS

[2]Project partners of NWE-REGENERATIS were: SPAQuE, Public Zaste Agency of Flanders (OVAM), Bergischer Abfallwirtschaftsverband (BAV), University of Liege, French Geological Survey (BRGM), Materials Processing Institute (MPI), Centre Technologique International de la Terre et de la Pierre (CTP), IXSANE, TEAM2, Technische Hochschule Köln, Materials Processing Institute (MPI) and Cranfield University

project is the estimation of volume(s) this was not always the case in RAWFILL project. The second step is to carry out the field survey using the previously selected methods.

The third step is the targeted sampling or the sampling survey based on the results of the geophysical data. After the sampling, it can be determined if the materials of interest were found and if they represent a quantity large enough. During NWE-REGENERATIS the materials of interest were metallurgical residues. For RAWFILL project this was not a mandatory question since laboratory measurements were not carried out. When the answer to the former question is positive, then samples are collected for geophysical and geochemical measurements in the laboratory.

In the next step we carry out a calibration of the geophysical field data with the information from the sampling (ground truth data). When laboratory measurements were not conducted, the calibration was based on the lithologic or rather anthropogenic facies description of the borehole/pits. If laboratory measurements are available, we can study the correlations between the geophysical and geochemical measurements in the lab. Overall, the aim of this step is to identify groups or classes of different materials or different chemical compositions. The final interpretation leads to a resource distribution model composed of the previously identified classes, i.e., classification in the whole field data domain. In this contribution we applied a machine learning algorithm and a probabilistic approach for the classification. But unsupervised learning approaches could also be used, e.g., Whiteley et al. (2021). The case studies presented in this thesis have been investigated using this workflow.

This thesis is organized as follows. Chapter 2 presents the basic theory of the electrical resistivity and induced polarization methods as well as the inversion framework reported here for the data processing, i.e., RES2DINV (Loke, 2004) and pyGIMLi (Rücker et al., 2017). We focused on these geoelectrical methods since they were widely used during this work and proved useful to derive resource distribution models for several sites in terms of anthropogenic materials, organic content and metallurgical residues with different composition. We tested different methods but these have been the most robust in the context of most of the sites.

Seismic, magnetic and electromagnetic methods were also used during RAWFILL and NWE-REGENERATIS project. Seismic methods were useful in both MSW landfills and metallurgical residues to roughly delineate the thickness of the deposits, nonetheless, if buried refractors are present, data acquisition, processing and interpretation becomes challenging. Magnetic and electromagnetic methods were largely used to map structures or zones laterally within the deposits, nonetheless quantitative interpretation is also challenging in these environments. With this regards,

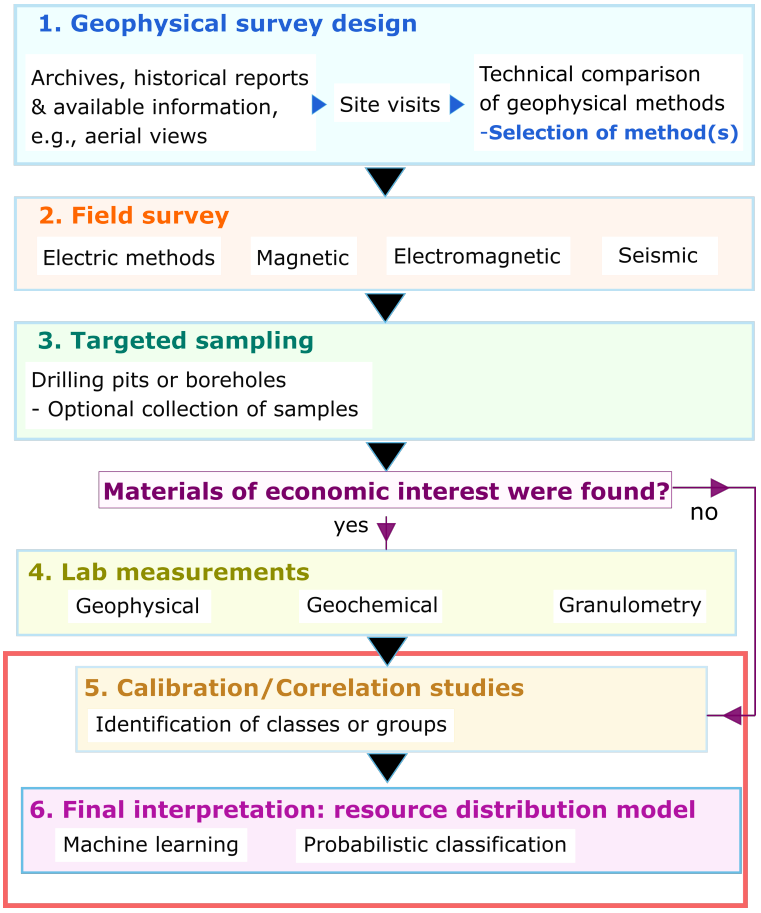

FIGURE 1.1: General workflow for the geophysical characterization of landfills and metallurgical residues. In this contribution we focused on steps 4 and 5 (marked in the red square): to calibrate geophysical data based on which a quantitative interpretation is derived.

Chapter 3 presents a critical review on the use of geophysical methods for the characterization of solid waste, in particular targeting the objectives of dynamic landfill management (DLM). It discusses case studies in several types of landfills and deposits, e.g., dumps with ashes and slags from former industrial activities/mining, engineered landfills and unauthorized fills. Even though multiple surface geophysical methods have proven useful to investigate the geometry, zonation and volume(s) of landfills and deposits, there is still a need to consider the uncertainty of the different investigation stages. In particular in investigations tailored to deploy a quantitative characterization of waste volumes.

With the above-mentioned motivation, Chapter 4, introduces a probabilistic approach for a quantitative interpretation of geoelectric data in a non-engineered landfill, composed of inert, household, and industrial waste. The probabilistic approach classifies different types of materials observed in borehole logs using inverted 2D

electrical resistivity tomography, induced polarization and the position of the boreholes. We assessed its performance for classification and compared it with an algorithm of machine learning (multi-layer perceptron).

Chapter 5 presents the geophysical investigation of a slag heap composed of secondary products from iron and steel making processes. It describes an integrated methodology to link geophysical and geochemical measurements in the laboratory and to interpret 3D geophysical field data using a probabilistic classification. The final objective is to identify different types of slags and estimate their corresponding volumes. The probabilistic classification allows to extend associated uncertainties to the derived resource distribution model and the estimation of volumes, which is useful information in the management of these sites.

Lastly, Chapter 6 presents the general conclusions of the thesis including perspectives that could be implemented in the characterization of landfills and anthropogenic deposits of different type.

Chapter 2

Employed geoelectric methods: basic principles and inversion

2.1 Electrical resistivity method

This method has been widely used in the characterization of several types of landfills and anthropogenic deposits, both for static investigations, e.g., vertical waste delineation (Dumont et al., 2017) and to monitor dynamic processes, e.g., leachate evolution (Audebert et al., 2014). Its aim is to obtain the resistivity distribution of the subsurface by injecting an electrical current into the soil with a pair of electrodes, and measuring the difference of potential with another pair of electrodes.

2.1.1 Basic principles

Consider an electrical current flowing in an homogeneous isotropic medium due to an electric field $\mathbf{E}$ in units of $[V/m]$. As the material is passive then the current density $\mathbf{J}$ in $[A/m^2]$ is controlled by the conducting properties of the medium or its conductivity $\sigma[S/m]$ (inverse of the electrical resistivity $\rho[\Omega m]$). Ohm's law relates the current density and the electric field as (Telford et al., 1990):

$$\mathbf{J} = \sigma \mathbf{E} \tag{2.1}$$

The flow of a current in a medium is based on the principle of conservation of charge, which can be derived by taking the divergence of the second Maxwell equation or Ampere's law, and it can be expressed as $\nabla \cdot \mathbf{J} = 0$ for stationary currents (Bhattacharya, 2012). This equation can be rewritten, considering that the electric field is the gradient of a scalar potential ($\mathbf{E} = -\nabla V$) and using Eq. 2.1, as $\nabla\sigma \cdot \nabla V + \sigma\nabla^2 V = 0$. Furthermore, if the medium is homogeneous and σ is constant, the former expression simplifies into Laplace's equation for the potential:

$$\nabla^2 V = 0 \tag{2.2}$$

This means that the electric potential distribution of a DC electric current flowing into an homogenous isotropic medium satisfies Laplace's equation.

In a homogeneous isotropic half-space where a point electrode is delivering an electrical current $I[A]$ at the surface, Laplace's equation can be used in spherical coordinates due to symmetry, i.e., the potential will be a function of the (radial) distance r from the electrode. The current flows through a hemispherical surface and therefore, the current density J can be computed for all radial directions as $J = \frac{I}{2\pi r^2}$. The solution of Equation 2.2 is given by

$$V = \frac{I\rho}{2\pi r} \quad \text{or} \quad \rho = \frac{2\pi r V}{I} \tag{2.3}$$

which indicates that the equipotentials are hemispherical surfaces below the ground (Telford et al., 1990). Note that in this case, only one electrode was considered for the current injection and the return current electrode was assumed to be located far away. However, the measurements of electrical resistivity usually require four electrodes at surface: two for the current injection (A and B) and two electrodes to measure a difference of potential (M and N). For the later generalized form of electrode configuration, the potential difference between electrodes M and N can be expressed as

$$\Delta V = V_M - V_N = \frac{I\rho}{2\pi}\left\{\left[\frac{1}{r_{AM}} - \frac{1}{r_{MB}}\right] - \left[\frac{1}{r_{AN}} - \frac{1}{r_{NB}}\right]\right\} \tag{2.4}$$

where r_{AM}, r_{MB}, r_{AN} and r_{NB}, represent the geometrical distances between electrodes A and M, M and B, A and N, and N-B respectively. Or in terms of the electrical resistivity:

$$\rho = \left[\frac{2\pi}{(1/r_{AM}) - (1/r_{MB}) - (1/r_{AN}) + (1/r_{NB})}\right]\frac{\Delta V}{I} = K\frac{\Delta V}{I} \tag{2.5}$$

where K is the geometrical coefficient that depends on the configuration of the four electrodes A, B, M and N. In an homogeneous isotropic media, the resistivity will be constant for any current and electrode configuration. However, in reality the ground is non-homogeneous and when the position of the electrodes is changed, both the ratio $\Delta V/I$ or the resistance R and the values of ρ will be different for

each measurement. This magnitude, which is not the "true" resistivity, is known as apparent resistivity (ρ_a) and it is strongly related to the electrodes' configuration (Reynolds, 2011). Then, Eq. 2.5 can be rewritten in terms of ρ_a as

$$\rho_a = K\frac{\Delta V}{I} = KR \tag{2.6}$$

2.1.2 Conduction processes

The main processes of charges transport in the near surface are primarily due to the movement of ions and the electron conducting minerals. The conduction of ionic transport of charge can be via the ions dissolved within the pore fluids and via the ions in the electrical double layer (EDL) at the mineral-fluid interface, also known as surface conduction. The ionic conduction in the pore fluid is driven by the salinity or ionic concentration in the fluid while the ionic conduction in the EDL is mostly determined by the amount of mineral-fluid surface area.

The conductivity of any material is proportional to the number of charges and the mobility of charge carriers. Unless indicated in the text, this subsection is overall based on Binley and Slater (2020).

Ionic conduction in a fluid

The spaces between the pores in natural rocks are relatively filled with water, which contains different ions of dissolved salts. Ionic or electrolytic conduction involves the transport of ions through the aqueous solution in connected pore spaces, when an electric field is present (Kemna, 2000). In the presence of water, ionic conduction is the most important charge transport determining the conductivity.

In general, the conductivity increases with the ion concentration in the pore solution due to the growing number of potential charge carriers. Furthermore, the conductivity of a fluid is dependent on the mobility of ionic charges, the viscosity and the temperature of the fluid (Kemna, 2000). The mobility of a single ion is proportional to the valence of the ion and the diffusion coefficient of the charged species in the fluid, and inversely proportional to the temperature. Additionally, the mobility of ionic charges can be related (inversely proportional) to the viscosity of the fluid and the radius of the hydrated ion. This means that anions are less mobile than smaller cations.

The electrical conductivity of an ionic solution can be described by relationships that highlight how the conductivity is proportional to the charge concentration and the mobility of the charge carrier among other contributions from individual ionic

constituents. However, extrapolating this, to determine the total conductivity of natural groundwater is not straightforward as groundwater typically has a complex ionic composition. Consequently, empirical formulas are used to explain how the conductivity of a solution varies with easily measurable properties such as salinity and temperature.

In some anthropogenic environments, for example in sulfide mineral deposits, oxidation processes can generate acid drainage when these materials are in contact with water (due to groundwater rise or increase of precipitation) and atmospheric oxygen (Keller, 1988; Placencia-Gómez et al., 2015). The analysis of geoelectrical measurements reliably identifies highly conductive zones due to the high salinity of the pore water (Epov et al., 2017). Similarly in the case of a municipal solid waste when leachate is present. In general, the leachate conductivity increases with the dissolution of salts due to dissolving waste materials (Dumont et al., 2016).

The electric double layer (EDL)

The EDL is formed when the charged mineral surface of the interconnected pore space attracts (and absorbs) charged ions from the pore fluid. First, all the minerals that are in contact with water develop a net surface charge due to the chemical reactivity. These reactions can result in positively or negatively charged zones at the surface depending on the pH of the fluid. Nonetheless, this charge is counterbalanced by charges that are relatively weekly adsorbed on the mineral surface on a monolayer called the Stern layer, and this in turn will result in the formation of a diffuse part of the double layer that will be depleted in anions or cations (Revil and Florsch, 2010). The Stern layer is located between the o-plane which corresponds to the true mineral surface and the d-plane which corresponds to the inner surface of the electrical diffuse layer (Figure 2.1).

The total surface site density represents then, the sum of the surface site densities. For a common value of groundwater pH, the mineral surface has a net negative charge that attracts cations from the bulk electrolyte and will result in a diffuse part of the double layer depleted in anions. This depletion is greater closer to the Stern layer and it decays exponentially with the distance from this plane towards the bulk electrolyte. In addition, the cations in the diffuse layer are loosely held to the surface and they can be easily exchanged for other cations, implicitly adding to the ion concentration within the electrolyte.

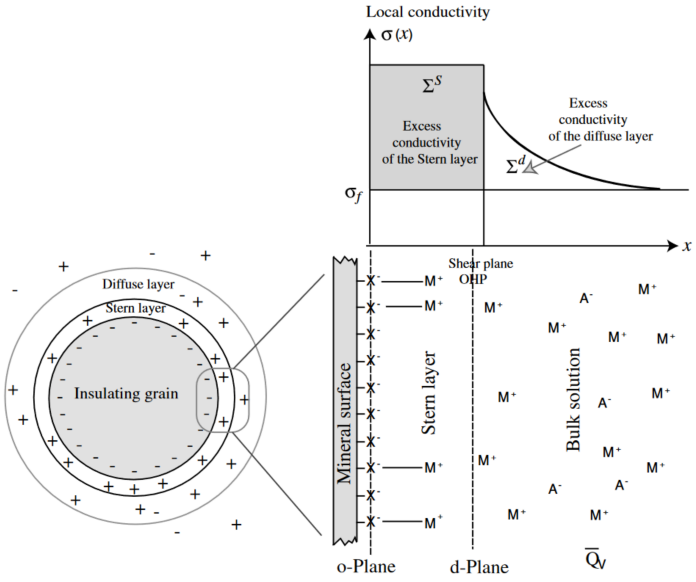

FIGURE 2.1: Sketch of the EDL and surface conduction in the pore space of a charged medium at equilibrium. Image from Revil and Florsch (2010).

Electron conduction

This mechanism is relevant in the presence of high concentrations of ore minerals and can occur in conductors as metals and also in semiconductors. The electron conductivity depends on the distance between energy gaps and temperature, as both control the electrons that are mobile (Binley and Slater, 2020). This mechanism will be further discussed in the induced polarization method.

2.1.3 Acquisition

Electrical resistivity methods can have different types of deployments such as vertical electrical sounding (at a single location in space), horizontal profiling to map lateral variations of resistivity (using a fixed electrode separation) and different borehole arrays involving receiver electrodes and/or transmitter electrodes placed either in the drillhole or on surface Butler, 2005. In this thesis, we focus on the configuration of ground based imaging or electrical resistivity tomography (ERT), which is widely used in the context of landfill investigations (Caterina et al., 2019; Dumont et al., 2017; Konstantaki et al., 2015). ERT allows to map both lateral and vertical variations of the resistivity along one or more profiles for 2D and 3D acquisitions. By changing the number of electrodes and the distances between them, as well as the configuration of the injection and potential electrodes multiple times, ERT can perform high resolution mapping of the resistivity in the near-surface at various investigation depths (Reynolds, 2011).

Multiple measurements of ERT will be collected by varying the positions of the current and potential electrodes using different geometries, i.e., electrode array, leading to the vertical and horizontal distribution of the apparent resistivity in the subsurface (Equation 2.6) or pseudosection. To avoid the polarization at the electrodes, the waveform of the injected current is usually a square wave alternating between positive and negative pulses (Figure 2.2) and generally applied at frequencies of about 0.5- 2 Hz (Binley and Kemna, 2005). Furthermore, the measurement cycle can be repeated or stacked to estimate a repetition error.

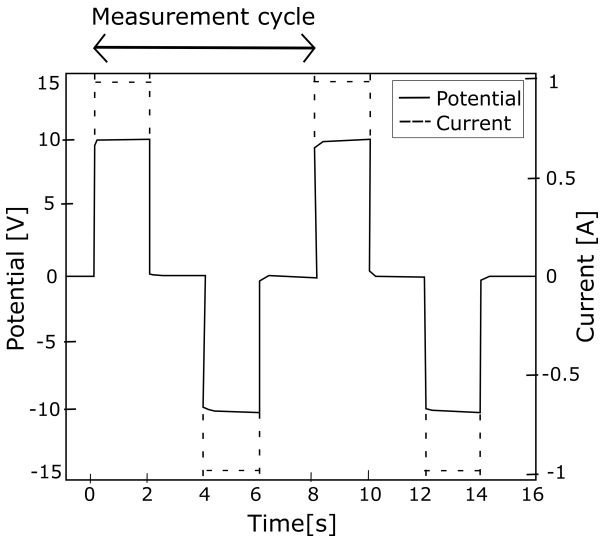

FIGURE 2.2: Square wave of the injected electrical current, using two stacks or repetitions. During the ON time of the electrical current, the resistivity data are measured. Image from TerrameterLS2 (2016).

Electrode array geometries

There are several types of electrode arrays configurations that can be used for a 2D or 3D ERT acquisition. Its selection depends on the expected geology, the objective of the survey, type of deployment and even the flexibility of the device (Binley and Slater, 2020; Dahlin and Zhou, 2004). The most common arrays are shown in Figure 2.3, where A and B refer to the current electrodes and M and N are the potential electrodes.

In general, the main features of these arrays are (Binley and Slater, 2020):

- In the **Wenner** array configuration, the electrodes are equally spaced a distance a and the current electrodes are outside the potential dipole, ensuring good measurement signal strength.

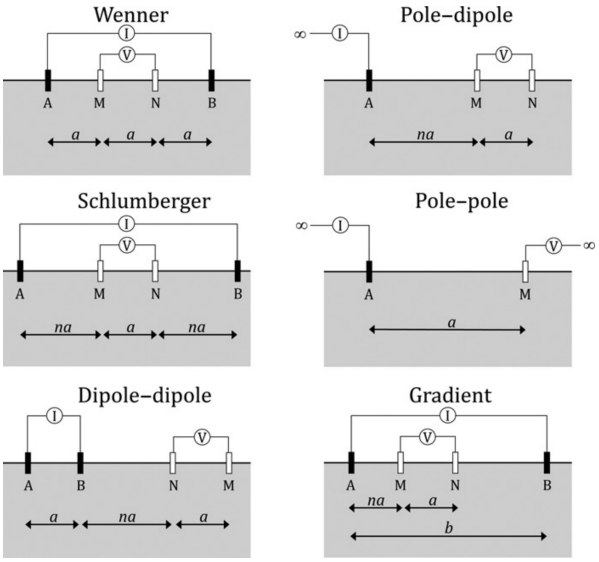

FIGURE 2.3: Most common electrode arrays for ERT acquisition. Image from Binley and Slater (2020).

- In the **Schlumberger** array, the distance between the current electrodes is much larger than the potential dipole spacing, i.e., $n > 2$, and it is relatively not sensitive to lateral variations of resistivity.
- In the **dipole-dipole** array, the current and potential electrodes are separated. This turns into a weaker signal strength (compared to Wenner and Schlumberger arrays).
- For both **pole-dipole** and **pole-pole** arrays, one or two electrodes are employed remotely, allowing a faster manual displacement of the mobile electrodes.
- The **gradient** array is carried out by using current electrodes separated a distance $b = (s + 2)a$ and measuring the potential differences with the potential electrodes with spacing a. The factor s is the maximum number of potential readings for a current injection (Dahlin and Zhou, 2006). This array takes advantage of the multi-electrode (multi-channels) measurements of devices.

The imaging resolution of the dipole-dipole array is greater than other arrays, specially for the location of vertical and dipping structures, yet the depth resolution is not the best. The gradient array is ideal for multichannel recording configurations, offering well resolved resistivity images (Dahlin and Zhou, 2004).

Noise level assessment

The data collected for ERT can be seen as data contaminated by some uncertain noise that cannot be modeled because it may arise from fluctuations in the contact

resistance, malfunction of the measuring device, misplaced electrodes, deterioration of contacts on electrode-cable connectors, intrinsic voltages within the ground an other sources of systematic and random errors (Binley and Slater, 2020).

To quantify this uncertainty and the overall noise level, first, a repetition or stack of the measured cycle (Fig. 2.2) can be recorded. During the acquisition it allows to define an error limit, based on the standard deviation of the stacks divided by the mean value of a data point. The number of stacks depends on the site conditions, electrode spread size and type of electrode array (TerrameterLS2, 2016).

Estimations of the noise level in the data are important as the inversion is a process that depends on these error parameters. An overestimation of the noise level can lead to an over-smoothed resistivity image, while an underestimation of noise level in the data can generate resistivity images with rough and irregular structures (Hermans et al., 2012). Furthermore, the noise estimates from repetition can greatly underestimate the true noise levels (LaBrecque et al., 1996) and better estimations come from comparing reciprocal measurements, which are collected by changing the current and potential electrodes from normal measurements. An example of the error that can be detected through reciprocal measurement is the case of a bad contact at a potential electrode; the difference of potential on the instrument may be recorded while changing the potential by the current electrodes would identify this problem (Slater et al., 2000).

Slater et al. (2000) proposed an alternative to assess the noise level using both the normal resistance measurement R_n and the reciprocal resistance measurement R_r, defined as:

$$e = R_n - R_r \tag{2.7}$$

which assumes that no current sources can be found in the subsurface.

As the exchange between the current and potential electrodes should not affect the measured resistivity (principle of reciprocity), then e is a measure of data noise. Slater et al. (2000) propose a Gaussian error model in which the magnitude of the reciprocal error $|e|$ increases with the magnitude of the measured resistance $|R|$ as:

$$|e| = a + b|R| \tag{2.8}$$

where a defines the minimum error and b defines the relative error increase with the resistance magnitude (see Figure 2.4). After the removal of outliers, the error parameters are defined by an envelope that contains the remaining points.

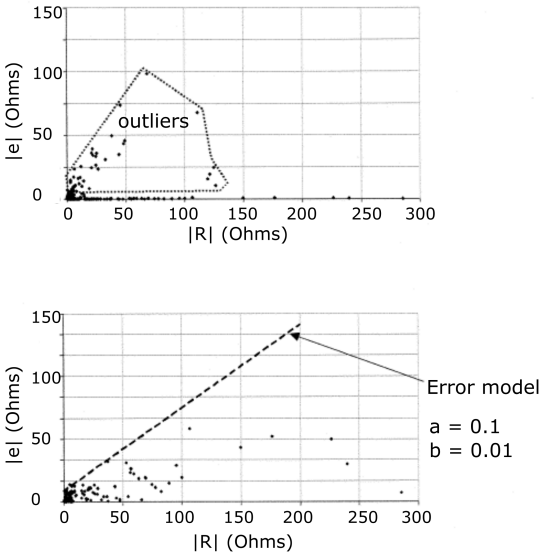

FIGURE 2.4: Outliers and error model in plots of the reciprocal error magnitude vs the resistance. Image from Slater et al. (2000).

2.2 Induced polarization method

The induced polarization (IP) method is an extension of the resistivity method and it is fundamentally, the manifestation of the frequency-dependence of resistivity reflected as a delay in the receiver response with respect to the transmitter, due to the charge storage of the medium. Then, in addition to the ability of a volume of material has to conduct electrons, IP provides information on the chargeability or the energy storage capacity of the subsurface (Butler, 2005).

IP measurements can be carried out in time-domain or frequency domain, where the method is know as complex conductivity (or resistivity) or spectral induced polarization (SIP). We illustrate the basic principles of the method in frequency domain to provide a more complete framework with further discussions on polarization mechanisms in addition to the already presented conduction processes and to illustrate how the IP method is an extension of the resistivity method. Note that in theory, time domain and frequency domain are equivalent but in practice, the limited frequency band of time domain IP restricts the range of frequency available in time-domain IP measurements, as opposed to frequency data.

2.2.1 Basic principles

The complex resistivity or SIP provides the most complete set of resistivity and IP data. SIP is a frequency-domain method that measures the amplitude and phase relationship between the injected current and the difference of potential at several frequencies. This allows the generation of a database of materials that may have characteristic amplitude and phase-shift behavior over a broad range of frequencies (Butler, 2005).

In addition to Ohm's Law (2.1), it is also possible to describe the macroscopic behavior of matter upon an electrical field through the constitutive equation

$$\mathbf{D} = \epsilon \mathbf{E} = \epsilon_r \epsilon_0 \mathbf{E} \tag{2.9}$$

where ϵ refers to the dielectric permittivity of the material and $\mathbf{D}$ to the displacement field. Equation 2.9 assumes that the polarization response of the material is purely dielectric and it is usually expressed in terms of the vacuum permittivity $\epsilon_0 = 8.854 \times 10^{-12} F/m$ and the relative dielectric permittivity ϵ_r, which accounts for the microscopic displacement of bound charges.

Substituting both Ohm's Law and equation 2.9 on the right hand of Ampere's Law, we can express the total current density as

$$\mathbf{J} = \sigma \mathbf{E} + \epsilon_r \epsilon_0 \frac{\partial \mathbf{E}}{\partial t} \tag{2.10}$$

In this method an alternating current is applied into the ground and this is generated by a (complex) electric field with an amplitude and a phase or $E = E_0 e^{iwt}$. Due to the derivative properties of the exponential function, using the complex electric field in Eq. 2.10 leads to

$$\mathbf{J} = \sigma^*(w) \mathbf{E} \tag{2.11}$$

where $\sigma^*(w) = \sigma + iw\epsilon_r\epsilon_0$ is the effective complex conductivity, which describes the contributions of the conduction and displacement current. $\sigma^*(w)$ is frequency dependent due to the displacement current contribution describing the dispersive nature of the dielectric polarization (Bücker, 2019).

To better understand the macroscopic effect that the microscopic charge storage in polarizable materials have on the current density or measured current (see Figure

2.5), we substitute the complex electrical field $E(t) = E_0 e^{iwt}$ and complex conductivity $\sigma^* = |\sigma| e^{i\varphi}$ in Eq. 2.11 (Bücker, 2019),

$$J(t) = \sigma^*(w)E(t) = E_0|\sigma|e^{i(wt+\varphi)} = J_0[cos(wt+\varphi) + isin(wt+\varphi)] \quad (2.12)$$

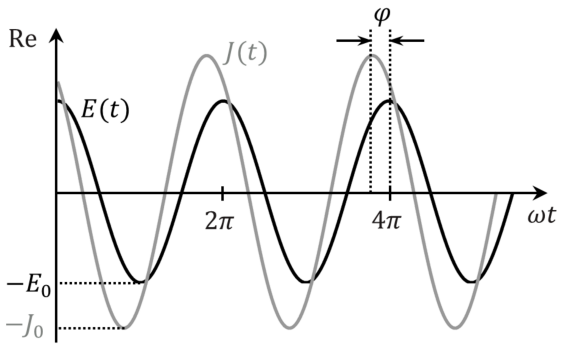

FIGURE 2.5: Harmonic variation of the real parts of the electric field E and the current density J. Image from Bücker (2019).

Note that we used a complex conductivity which can also be explained with a real (σ') and imaginary (σ'') components as

$$\sigma^* = |\sigma|e^{i\varphi} = \sigma' + i\sigma'' \quad (2.13)$$

where $|\sigma|$ is the conductivity magnitude and φ is the phase (which is positive when we work in the conductivity space). The phase represents the lag that the induced alternating current have after the injected current. σ' is associated with the conduction strength and σ'' is associated with any charge storage mechanism or polarization effect (Binley and Slater, 2020). Additionally, at low frequencies, the charge storage is small relative to conduction mechanisms ($|\sigma| \approx \sigma'$) and then

$$\varphi = tan^{-1}\frac{\sigma''}{\sigma'} \approx \frac{\sigma''}{\sigma'} \quad (2.14)$$

This approximation is valid for most applications where phase shifts are sufficiently small, i.e., $\varphi < 0.1$ radians (Flores-Orozco et al., 2020).

Finally, note that former equations can also be represented in terms of the generalized complex dielectric permittivity or the equivalent effective complex resistivity $\rho^* = 1/\sigma^*$.

2.2.2 Polarization mechanisms

There are distinct polarization mechanisms that are needed to explain the complex effective properties measured over a broad range of frequency, e.g., 10^{-3} to 10^{11} Hz (Binley and Slater, 2020). First, we describe the polarization mechanisms that can result from the ionic transport of charge: the first one is controlled by the pore volume properties (corresponding to the ionic conduction in a fluid, section 2.1.2) and the second one is controlled by the pore surface properties (corresponding to ions in the EDL at the mineral-fluid interface, section 2.1.2).

Due to the strong polarization response of metallic minerals, the IP method has been widely used in the exploration of mineral deposits and metallic ores (Revil et al., 2022) and in remediation strategies based on biostimulation (Slater et al., 2007) among other applications. Therefore, we also discuss about the polarization arising around metallic particles (electronic conduction, section 2.1.2). Lastly we briefly describe the so-called Maxwell-Wagner polarization.

Ionic transport polarization

Although this polarization may only occur at high frequencies, it is worth mentioning to understand the behavior of σ' with frequency, when measuring SIP or complex conductivity. In the electrolyte, each ion is surrounded by a charged ionic cloud of opposite charge. When the electrical field is applied, the ion's cloud can suffer a lag from the central ion when the latter moves as response to the field. This leads to a braking Coulomb force due to an asymmetric charge distribution. Then, the electrolytic conductivity increases with the frequency of the applied field, as the ionic cloud lacks more time to build up the braking charge distribution and overall, the mobility of ions increases. In turn, this leads to an ionic polarization that makes the conductivity of the pore solution to be complex. Nonetheless, for the lower frequency range ($f < 10$ kHz) the associated phase shift is virtually zero and the conductivity of the fluid can be considered as a real-valued quantity (Kemna, 2000).

EDL polarization

The two main polarization mechanisms discussed in this section are associated with the EDL and have been used to explain frequency-independent and frequency-dependent measurements. These mechanisms are associated with diffusion-driven decays of ionic concentration gradients caused by an applied electric field and measured at low frequencies. The diffusive decays results from the redistribution of ions from the excited state back to the equilibrium position (Binley and Slater, 2020). In this sense, these are diffusion-dominated and reversible EDL polarization mechanisms.

To recap, the EDL is formed at the interface between the charged grain surfaces and the electrolyte (Fig. 2.1). It is formed in electrokinetic equilibrium of diffusion and Coulombic interaction when the negative (or positive) surface charges of a particle attract cations (or anions) from the pore solution. The EDL is composed of the charged particle surface, an adjacent fixed layer of adsorbed charges known as Stern layer and a diffuse layer of mobile ions (Kemna, 2000).

The first polarization mechanism is known as Stern layer polarization. It originates from the tangential displacement of counterions in the Stern layer forming at mineral surfaces and it is controlled by the grain size distribution. The second mechanisms, known as membrane polarization, is based on the different mobility that ions present within the pore solution in the vicinity of the EDL. It is caused by the blockage of ions in the diffuse layer at the interconnected pore space where there are zones of charge excesses and deficiencies (Binley and Slater, 2020). Therefore, this polarization depends on the pore channel geometry (Kemna, 2000).

It has been suggested that the Stern layer polarization dominates the IP measurements, except at high salinities where the membrane polarization may be stronger (Binley and Slater, 2020).

Figure 2.6 presents the diagrams of both polarization mechanisms: the membrane polarization (a), where the polarizable elements block pore throats and the Stern layer polarization (b) where the polarizable elements are in parallel with the pore throats. In the membrane polarization, a clay particle is used to illustrate a blockage of anions. In general, clay minerals play an important role regarding surface complex conductivity phenomena.

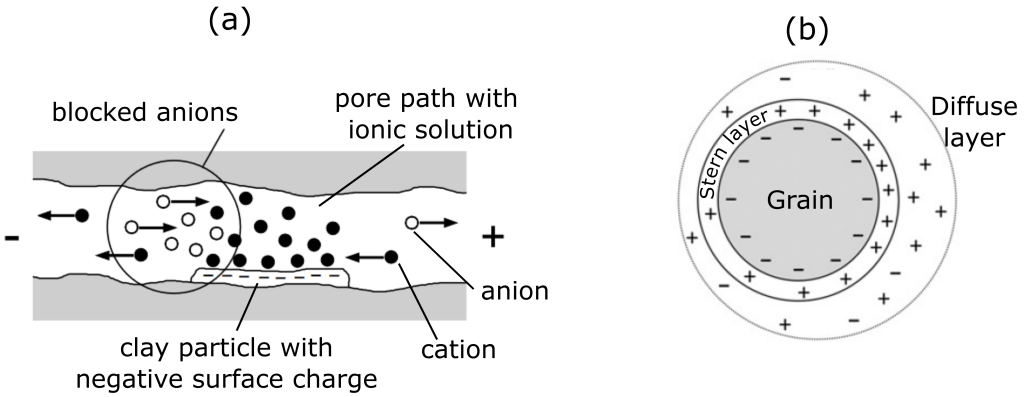

FIGURE 2.6: Diagram of (a) membrane polarization and (b) Stern layer polarization. Image modified from Kemna (2000) and Binley and Slater (2020).

Polarization around metallic particles

This subsection is focused on the role of the electron conducting particles in the IP effect. The mechanism is known as electrode polarization as the electron conducting grains have been assumed to act as electrodes throughout a rock (Binley and Slater, 2020). Furthermore, variations in the electrical properties measured (in particular with SIP), can be observed not only from the intrinsic polarization and capacitance of metallic particles but also from surface reactions such as oxidation-reduction and precipitation-adsorption of secondary minerals, which modify the surface texture of metallic particles (Placencia-Gómez et al., 2015).

Although classical models cannot fully explain the broad variety of IP signatures, first, the frequency dispersion observed in the conductivities was attributed to the polarization at the solid-liquid interface between highly conductive mineral grains and the surrounding electrolyte, i.e., electrode polarization. Then, the models from Wong (1979) and Wong and Strangway (1981), directly related the IP response to the geometrical and electrochemical properties of the highly conductive particles embeded in the electrolyte (Bücker, 2019).

The fact that several ore minerals are semiconductors was taken into account by Revil et al. (2015) and Misra et al. (2016), who noted that assuming perfectly conducting particles was not suitable. They proposed models for semiconducting particles, including additionally the contribution of non-metallic background material to the polarization response (Bücker, 2019).

Maxwell-Wagner polarization

Although the IP response of a porous medium is overall attributed to the diffusion-limited EDL polarization at the mineral-fluid interface, the Maxwell-Wagner polarization mechanism aims to (partially) explain the dispersion curves observed at high frequencies (> 100 Hz).

It has been proposed that this polarization exists due to the bulk electrical properties of soil and rock components, and it originates from the discontinuity in conductivity at interfaces between the different phases of the porous medium (solid, liquid, gas). Therefore, this mechanisms is associated with the geometric arrangement of the phases. Nonetheless, it is hard to determine if the Maxwell-Wagner polarization is truly observed, since the dispersion observed at higher frequencies in many SIP spectra can be due to electrodes and instrumentation errors (Binley and Slater, 2020). Yet, advances in the development of modern impedance tomography systems

have been made to mitigate these errors, e.g., shielded cables to avoid crosstalk between channels and integrated switches for reciprocal measurements (Zimmermann et al., 2010).

2.2.3 Acquisition

Both time-domain and frequency-domain IP have been used in environmental applications to characterize municipal solid waste landfills, mapping contamination plumes, and in remediation strategies of aquifers (Flores-Orozco et al., 2020; Kessouri et al., 2022). The method has been also applied to the mining industry, for the investigation of disseminated sulfide and nonsulfide sources and anthropogenic materials (Butler, 2005). In this section we mostly focus on time-domain measurements equal to all the field surveys that were conducted during this thesis. As DC ERT and IP are applied together, the configuration or geometry arrays of the electrodes for IP acquisition can be found in subsection 2.1.3.

Time-domain measurements

Time-domain IP method was patented by Conrad Schlumberger in 1912 and in practice, it can be surveyed together with the resistivity in DC, by measuring the voltage decay with time after the current is switched off.

Seigel (1959) introduced a model for the polarization effect, defining the apparent chargeability m_a as

$$m_a = \frac{V_s}{V_p} \tag{2.15}$$

where V_s is the secondary voltage or the voltage immediately after the current is stopped and V_p is the primary voltage recorded during the transmitter on time, see Figure 2.7a (Binley and Kemna, 2005). More recently, it has been reported that Conrad (1939) first proposed to quantify the strength of the polarization from the ratio of the secondary to the primary voltage (Binley and Slater, 2020).

It is common to report m_a with the units of mV/V as V_s is typically 2-3 orders of magnitude smaller than V_p, except in the case of metals. Yet, in practice it is not easy to measure V_s and commonly the IP effect is quantified through the integral of the decay curve broken into time windows, see Figure 2.7b (Binley and Slater, 2020). For a single time window, defined between times t_1 and t_2 after shut-off, the apparent chargeability can be expressed as

$$m_a = \frac{1}{t_2 - t_1} \frac{\int_{t_1}^{t_2} V_s dt}{V_p} \tag{2.16}$$

In some cases the apparent chargeability can also be expressed as $m_a = \frac{\int_{t_1}^{t_2} V_s dt}{V_p}$, which has units of time.

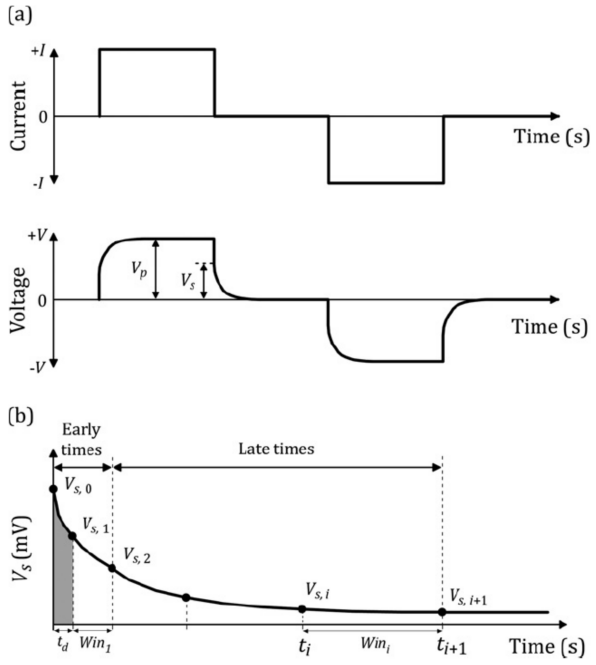

FIGURE 2.7: Time-domain IP acquisition with a conventional 50% duty cycle mode, i.e., measurement periods are divided into two equal parts, where the (secondary) voltage decay is measured during the OFF part. t_d is the delay time to start recording after the current is off. Image from Binley and Slater (2020).

Note that the value of m_a depends on the integration times t_1 and t_2 of the decaying curve. For a fixed t_1, shorter decaying periods of time will lead to smaller apparent chargeabilities. In addition, the effect of inductive coupling between the cables into the ground may be predominant at shorter times and decay relatively fast (Dahlin et al., 2002). Therefore, it is important to select a delay time t_d before recording the IP signal ($\sim$ 80- 240 ms). Mao et al. (2016) studied a porous media with metallic particles at lab scale and observed that the electromagnetic coupling affected the IP response considering a delay time up to 20 ms, yet larger time delays were expected for the field (with values of t_d up to 400 ms).

Noise level assessment

In analogy with Eq. 2.7, the error based on the apparent chargeability can also be estimated. This error as a function of the resistance will show a non-linear behavior, with higher errors occurring both for low apparent chargeability values (due to the resolution of V_s) and for large resistances, see Figure 2.8a. If the chargeability error is represented as a function of the apparent chargeability, then a similar tendency is observed with larger chargeability errors for small and large values of chargeability, see Fig. 2.8b (Binley and Slater, 2020). Nonetheless, in time-domain surveys is essential to check before the quality of the decay curves measured and filter out the ones which are not consistent, e.g., by fitting an exponential decay curve.

In terms of frequency-domain measurements, Orozco et al. (2012) proposed an inverse power-law model to quantify the phase error as a function of the resistance. Overall, the authors observed that the phase error decreases with the resistance or impedance values values, e.g., Figure 2.8c.

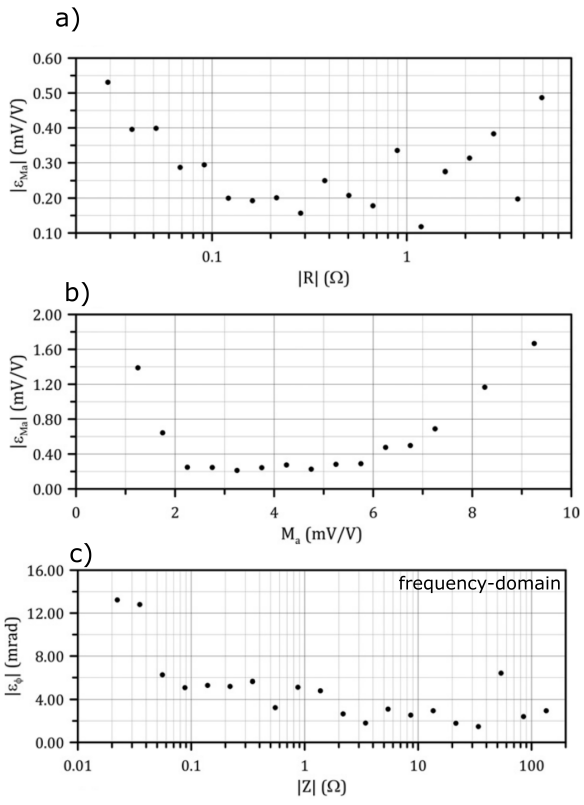

FIGURE 2.8: Reciprocal errors in terms of different measurements. a) Chargeability error as function of the resistance and b) chargeability error as function of the chargeability (time-domain), and c) phase angle error as function of the resistance or impedance (frequency-domain measurements). Image from Binley and Slater (2020).

Frequency domain measurements - lab scale

During this thesis SIP was only applied at lab scale, where the frequency dependent phase spectrum is measured over a broad range of frequencies. In general, an harmonic sinusoidal function is used to measure the complex impedance as a function of frequency, usually reported as a the magnitude $|Z|$ and the phase angle φ. This phase angle is a negative quantity for a polarizable medium, which is consistent with the impedance of a capacitor in an electric circuit. Then the measured $|Z|$ and φ are combined with the geometric factor to derive the complex resistivity or complex conductivity (Binley and Slater, 2020).

As will be explained in Chapter 4, in this thesis we used the impedance analyzer ZEL-2-SIP04-V05. This systems uses the four-point measurement mode to determine the impedance across a sample which is assumed to be homogeneous. It is composed of a function generator, an amplifier unit, an analog-to-digital converter card, a PC and a sample holder with a pair of electrodes for current injection and a pair of electrodes for voltage measurement. The function generator creates a sinusoidal excitation voltage within a range between 1 mHz to 45 kHz (Zimmermann et al., 2008).

2.3 The inverse problem

Inverse theory, oppositely to the forward theory which predicts data or the results of measurements from some general principle or model, addresses the reverse problem: starting with the data and a quantitative model, it estimates model parameters (Menke, 2018). If the data $\mathbf{d}$ and model parameters $\mathbf{m}$ are related in general by implicit equations $\mathbf{f}$ as $\mathbf{f}(\mathbf{d}, \mathbf{m}) = 0$ and the data can be separated from the model parameters, the explicit linear form of the inverse problem can be expressed as

$$\mathbf{f}(\mathbf{d}, \mathbf{m}) = 0 = \mathbf{d} - \mathbf{G}\mathbf{m} \tag{2.17}$$

where the matrix $\mathbf{G}$ is the data kernel. The explicit linear equation $\mathbf{G}\mathbf{m} = \mathbf{d}$ explains the simplest inverse problems (e.g., straight line fitting), and can also be written in the explicit form as $\mathbf{G}(\mathbf{m}) = \mathbf{d}$. Note that this equation is linear in the data but it can be nonlinear in the model parameters through $\mathbf{G}$ (Menke, 2018).

In this section we first show the least squares solution for the linear inverse problem, where we discuss the regularization for ill-conditioned problems and the weighted

measures of the length solution and data errors as a priori information. Then we discuss the Gauss-Newton method used to solve the nonlinear inverse problem, using weighted least squares and weighted damped least squares. The resulting latter equations are the inversion algorithm used for the software RES2DINV (Loke, 2004) and pyGIMLi (Rücker et al., 2017), both used in this thesis for the inversion of geoelectric data.

2.3.1 Least squares for the linear Gaussian inverse problem

The simplest solution to the linear inverse problem is based on a measure of the length of the estimated model parameters and a measure of the predicted data, i.e., least squares method. In this method the model parameters are selected in such a way that the predicted data $\mathbf{d}^{pre}$ are as close as possible to the observed data $\mathbf{d}^{obs}$. In this sense the prediction error or misfit is defined as $e_i = d_i^{obs} - d_i^{pre}$ and the best model is obtained when the model parameters lead to the smallest overall error

$$E = \sum_{i=1}^{N} e_i^2 = \mathbf{e}^T\mathbf{e} = (\mathbf{d} - \mathbf{Gm})^T(\mathbf{d} - \mathbf{Gm}) \tag{2.18}$$

which is the square of the norm L_2 or Euclidean length (and implied that the data obey Gaussian statistics). Although the method of least squares uses norm L_2, if data are very accurate a higher norm may be used and oppositely if the data are widely scattered, a lower order norm may be more suitable.

The least square solution to the linear inverse problem then looks to minimize the total error E. This can be done through the derivative of E with respect to the model parameters and setting the result to zero, which yields to $\mathbf{G}^T\mathbf{Gm} - \mathbf{G}^T\mathbf{d} = 0$. Assuming that $[\mathbf{G}^T\mathbf{G}]^{-1}$ exist, then the estimates for the model parameters can be defined as

$$\mathbf{m}^{est} = [\mathbf{G}^T\mathbf{G}]^{-1}\mathbf{G}^T\mathbf{d} \tag{2.19}$$

Although least squares fails for problems with nonunique solutions, there are alternatives proposed for underdetermined (more unknowns than data) problems and overdetermined problems (more data than unknowns) that are based on the prediction error E and the measure of the length of the solution $L = \mathbf{m}^T\mathbf{m}$ - for norm L_2 (Menke, 2018).

Regularization for ill-conditioned problems

In practice most of the inverse problems are not fully overdetermined nor completely underdetermined. One solution is to conduct a partitioning process of the unknown model parameters based on singular value decomposition of the data kernel. Yet there is another alternative that can be applied on relative underdetermined inversion problems. The idea is to find a solution of estimated parameters that minimizes a combination function Φ of the prediction error E and the solution length L as

$$\Phi(\mathbf{m}) = E + \lambda L = \mathbf{e}^T\mathbf{e} + \lambda \mathbf{m}^T\mathbf{m} \tag{2.20}$$

where λ defines the importance given to the parameter estimation solution with respect to the prediction error. This is also known as damped least squares problem. If λ is large enough, the minimization of Φ will not minimize the prediction error E and the resulting solution may not be an accurate estimation of the true model. If λ is zero, no a priori information can be provided to solve the underdetermined model parameters (Menke, 2018).

Weighted measures of length

The measure of the solution simplicity can be generalized by using a weighted measure of the solution length including a priori values of the model parameters $\mathbf{m}_0$ as

$$L = [\mathbf{m} - \mathbf{m}_0]^T\mathbf{W}_m[\mathbf{m} - \mathbf{m}_0] \tag{2.21}$$

where $\mathbf{W}_m$ is the weighting matrix that quantifies several measures of model's simplicity. Furthermore, the prediction error can also be expressed as a weighted measure, thus accounting for the fact that some observed data are noisier than others. The generalized prediction error can be expressed as: $E = \mathbf{e}^T\mathbf{W}_e\mathbf{e}$, where the matrix $\mathbf{W}_e$ defines the relative contributions of the individual errors to the total prediction error (Menke, 2018). $\mathbf{W}_e$ is a diagonal matrix whose elements contain the inverse of the standard deviation $\mathbf{W}_e = diag(1/\sigma_1^2, ..., 1/\sigma_N^2)$. Then the weighted least squares problem consists in minimizing the generalized total error or:

$$E = \mathbf{e}^T\mathbf{W}_e\mathbf{e} = \sum_{i=1}^{N}\left(\frac{d_i - (\mathbf{Gm})_i}{\sigma_i}\right)^2 \tag{2.22}$$

2.3.2 Gauss-Newton for nonlinear least squares problem

Gauss-Newton is an specialized version of the Newton method and both were developed to solve the nonlinear inverse problem. The Newton method uses the form of the total prediction error $E(\mathbf{m})$ in the vicinity of a solution $\mathbf{m}^{(p)}$, to look for a better solution $\mathbf{m}^{(p+1)}$ (Menke, 2018). However, the method may not present an exact solution in problems with a different number of data and model parameters. This subsection is mostly based on Aster et al. (2018).

The Gauss-Newton method aims to solve a nonlinear least square problem, by finding the model parameters **m** constrained by a data vector **d** with associated standard deviations.

Weighted least squares

Assuming that the observed errors are normally distributed, then the sum of the squared errors normalized by their standard deviations σ_i is minimized (maximum likelihood principle). Furthermore, if the misfits or residuals e_i are represented as scalar-valued functions $f_i(\mathbf{m}) = \frac{\mathbf{G}(\mathbf{m})_i - d_i}{\sigma_i}$ for $i = 1, ..., N$ and defining the vector-valued function $\mathbf{F}(\mathbf{m}) = [f_1(\mathbf{m}), ..., f_N(\mathbf{m})]^T$, the objective is to minimize the weighted residual (squared) norm L_2 as

$$\chi^2(\mathbf{m}) = \sum_{i=1}^{N} f_i(\mathbf{m})^2 = \| \mathbf{F}(\mathbf{m}) \|_2^2 \tag{2.23}$$

which is the weighted least squares problem (Eq. 2.22). Then, the gradient of $\chi^2(\mathbf{m})$ can be computed as the sum of the individual gradients of each f_i, which can be expressed as

$$\nabla\chi^2(\mathbf{m}) = 2\mathbf{J}(\mathbf{m})^T\mathbf{F}(\mathbf{m}) \tag{2.24}$$

where the Jacobian $\mathbf{J}(\mathbf{m})$ is represented as a matrix whose elements are the partial derivatives of the functions f_i with respect to the parameters m_i.

In a similar way, the Hessian of $\chi^2(\mathbf{m})$ can also be expressed as $\mathbf{H}(\chi^2(\mathbf{m})) = \sum_{i=1}^{N} \mathbf{H}(f_i(\mathbf{m})^2)$. Furthermore, in the Gaussian-Newton method the Hessian is approximated as

$$\mathbf{H}(\chi^2(\mathbf{m})) \approx 2\mathbf{J}(\mathbf{m})^T\mathbf{J}(\mathbf{m}) \tag{2.25}$$

In the Newton method, the minimization of $\chi^2(\mathbf{m})$ is done by solving the linear system of equations $\mathbf{H}(\chi^2(\mathbf{m}^{(0)}))\Delta\mathbf{m} = -\nabla\chi^2(\mathbf{m}^{(0)})$, given the initial solution $\mathbf{m}^{(0)}$. The implementation of Gauss-Newton introduces Eqs. 2.24 and 2.25 in the former system of equations, obtaining

$$\mathbf{J}(\mathbf{m}^{(k)})^T\mathbf{J}(\mathbf{m}^{(k)})\Delta\mathbf{m}^{(k)} = -\mathbf{J}(\mathbf{m}^{(k)})^T\mathbf{F}(\mathbf{m}^{(k)}) \tag{2.26}$$

This system of equations is then solved for the successive updates $\Delta\mathbf{m}$. After computing this parameter change vector, a new model is obtained by $\mathbf{m}^{(k+1)} = \mathbf{m}^{(k)} + \Delta\mathbf{m}^{(k)}$. Note however that for both Newton and Gauss-Newton methods, the solution may converge to a local minimum instead of the global minimum (Menke, 2018).

Furthermore, Eq. 2.26 is in practice rarely used in the geophysical inversion as the product $\mathbf{J}^T\mathbf{J}$ might be singular or nearly singular. This problem was mitigated by the Marquardt-Levenberg modification, which integrates a damping factor λ to ensure convergence and as a constrain to the range of values that $\Delta\mathbf{m}$ can take. However, it has only been successfully used for a small number of model parameters in resistivity inversions, e.g., sounding data. To further solve this problem, the Gauss-Newton least-squares equation is again modified to minimize the spatial variations in the model parameters, i.e., a smoothness-constrained, and it can be expressed as

$$[\mathbf{J}(\mathbf{m}^{(k)})^T\mathbf{J}(\mathbf{m}^{(k)}) + \lambda\mathbf{D}]\Delta\mathbf{m}^{(k)} = \mathbf{J}(\mathbf{m}^{(k)})^T\mathbf{F}(\mathbf{m}^{(k)}) - \lambda\mathbf{D}\mathbf{m}^{(k)} \tag{2.27}$$

where $\mathbf{D} = \alpha_x\mathbf{C}_x^T\mathbf{C}_x + \alpha_y\mathbf{C}_y^T\mathbf{C}_y + \alpha_z\mathbf{C}_z^T\mathbf{C}_z$ and $\mathbf{C}_x$, $\mathbf{C}_y$ and $\mathbf{C}_z$ are the smoothing matrices in the three directions (x, y, z). α_x, α_y and α_z are the relative weights giving to the smoothing matrices. Note that the operator $\mathbf{D}$ is the weighting matrix $\mathbf{W}_m$ in the measure of the solution simplicity or the parameter objective function (Eq. 2.21), that in general integrates a prior information and/or smooths the model to be able to fit the data. Additionally, note that Eq. 2.27 minimizes the square of the constrained values of $\Delta\mathbf{m}$ and the spatial changes or roughness of the model parameters. It is a L_2 norm smoothness-constrained optimization method that tends to produce smooth inverted models (Loke, 2004).

When the geology is composed of sharp boundaries between the regions, it may be more suited to adapt the method using the norm L_1. This is the L_1 norm smoothness-constrain optimization method also known as blocky inversion (Loke, 2004) and it can be defined as

$$[\mathbf{J}(\mathbf{m}^{(k)})^T\mathbf{J}(\mathbf{m}^{(k)}) + \lambda\mathbf{D}_R]\Delta\mathbf{m}^{(k)} = \mathbf{J}(\mathbf{m}^{(k)})^T\mathbf{R}_d\mathbf{F}(\mathbf{m}^{(k)}) - \lambda\mathbf{D}_R\mathbf{m}^{(k)} \tag{2.28}$$

where $\mathbf{D}_R = \alpha_x\mathbf{C}_x^T\mathbf{R}_m\mathbf{C}_x + \alpha_y\mathbf{C}_y^T\mathbf{R}_m\mathbf{C}_y + \alpha_z\mathbf{C}_z^T\mathbf{R}_m\mathbf{C}_z$. The matrices $\mathbf{R}_d$ and $\mathbf{R}_m$ represent the introduced weighting of the data misfit and model roughness.

Weighted damped least squares

The Gauss-Newton method can also be used directly to minimize an objective function that accounts for the weighted measures of both the solution length 2.3.1 and the generalized prediction error (or data misfit, 2.3.1). This objective function can be expressed as:

$$\Phi = \|\mathbf{W}_e(\mathbf{G}(\mathbf{m}) - \mathbf{d})\|_2^2 + \lambda\|\mathbf{W}_m(\mathbf{m} - \mathbf{m}_0)\|_2^2 \tag{2.29}$$

where again $\mathbf{W}_e$ is the data weighting matrix containing the inverse of the standard deviations, $\mathbf{W}_m$ is the model constrain matrix, $\mathbf{m}_0$ is the reference model and λ is the regularization parameter, which can be kept at a constant value, or be optimized at each iteration to locally minimize the data misfit. Re-applying Gauss-Newton method in the minimization of the former objective function (Eq. 2.29) leads to

$$\begin{aligned}[\mathbf{J}(\mathbf{m}^{(k)})^T\mathbf{W}_e^T\mathbf{W}_e\mathbf{J}(\mathbf{m}^{(k)}) + \lambda\mathbf{W}_m^T\mathbf{W}_m]\Delta\mathbf{m}^{(k)} \\ = \mathbf{J}(\mathbf{m}^{(k)})^T\mathbf{W}_e^T\mathbf{W}_e(\mathbf{d} - \mathbf{G}(\mathbf{m}^k)) - \lambda\mathbf{W}_m^T\mathbf{W}_m(\mathbf{m}^{(k)} - \mathbf{m}^{(0)})\end{aligned} \tag{2.30}$$

Where $\mathbf{m}^{(k+1)} = \mathbf{m}^{(k)} + \Delta\mathbf{m}^{(k)}$ (Rücker et al., 2017).

2.3.3 Stopping criteria

In the software that we used in this contribution a similar criterion is used to stop the inversion process. In RES2DINV the root mean square (rms) misfit is used as convergence limit and it is defined by the user. The inversion may stop when the rms error is usually between 2- 5 % or when the relative change in the rms error between two iterations is smaller than 5 % (Loke, 2003). In pyGIMLi the iterations are stopped when the mean of the squared error-weighted data misfit χ^2 (see Eq. 2.23) is below the noise level, i.e., $\chi^2 \leq 1$ or when the maximal iteration number is reached, i.e., 20 (Rücker et al., 2017). Other criteria may include a relative change

in the whole objective function below 1 % (Fiandaca et al., 2012) or when the rms of the error weighted data misfit reaches the value of one for a maximum value of λ (Kemna, 2000; Nguyen et al., 2016).

Chapter 3

Quantifying solid waste deposits and mapping associtated dynamic processes using non-invasive geophysical methods: a critical review

Non-invasive geophysical methods have demonstrated their usefulness for landfill characterization and monitoring. They provide complementary information on the waste extension and give indirect indications of waste composition and conditions related to leachate content and gas. However, most of the reported studies are focused on environmental risk assessment, and rarely on the potential for landfill mining nor on the optimization of short-term use of landfill spaces in line with the circular economy. For these broader objectives, captured in the concept of Dynamic Landfill Management (DLM), geophysical studies require to be adjusted to more specific quantitative targets and to be more comprehensive in terms of the spatial and temporal resolution required. Furthermore, heterogeneous waste materials and dynamic processes developed within them contribute to complex bulk geophysical responses, which can lead to ambiguities in the interpretations. It is, therefore, highly important to calibrate and interpret geophysical results using ground truth data to develop robust decision support tools to evaluate different management scenarios. In this contribution, we identify and review recent and reference works that address three relevant geophysical targets not only for a sustainable landfill management but for the selection of feasible economic, effective and sustainable scenarios for landfill remediation/redevelopment and potential resource recovery. First, we focus on the quantification of the landfill boundaries and landfilled waste materials (zonation), giving specific attention to the assessment of uncertainties related to geophysical data acquisition and processing. Then, we focus on the geophysical investigations

on the static characterization and monitoring of leachate mainly in municipal solid waste and on the identification-delineation of landfill gas accumulation zones and other processes related to biodegradation. In addition, we present an overview of the geophysical methods used in the specific investigation of metallurgical residues and deposits, both at lab and field scale. Finally, we discuss the main associated challenges and novel methodologies that could potentially improve the insights derived from geophysics.

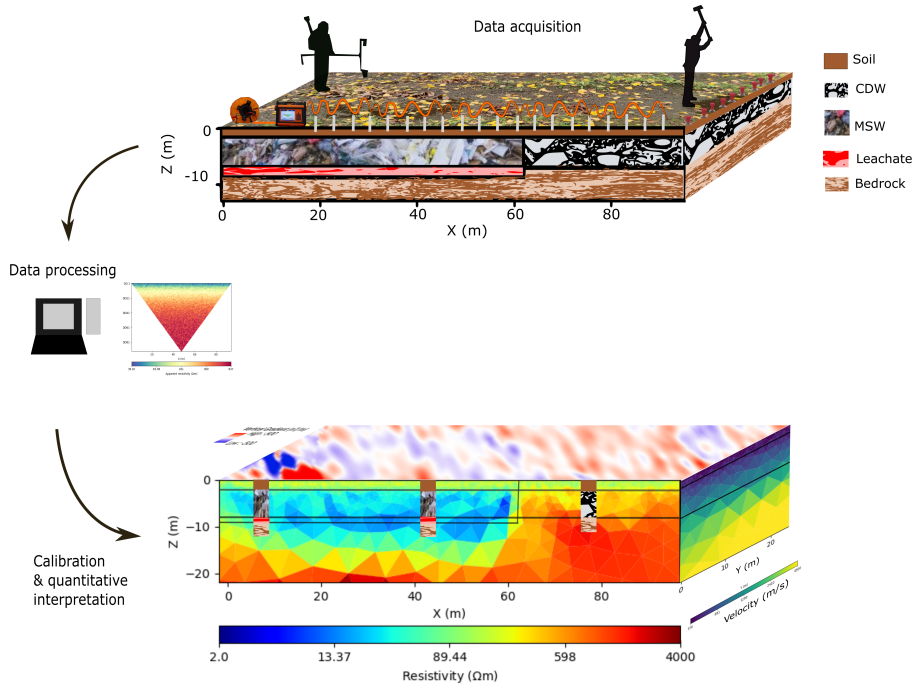

FIGURE 3.1: Graphical abstract.

3.1 Introduction

The existing historic landfills and the continuously increasing waste generation have highlighted the need to develop a sustainable vision on waste management involving the temporary and (supposedly) permanent storage of waste in landfills. In this perspective, strategies have been developed that aim to support the transition to a low-carbon, resource-efficient, circular economy such as Enhanced Landfill Mining (ELFM) (Jones et al., 2013). Furthermore, research is being conducted to explore the feasibility of resource recovery from landfills and to improve the processing and valorization of excavated waste fractions (Neculau et al., 2019; Vollprecht et al., 2021). Nevertheless, the current uncertainty on the long-term liabilities established by the EU Landfill Directive together with variable local policies and the non-dynamic environmental risk-based view on landfills, downgrade the opportunities associated with

landfill mining thereby making them less attractive (Jones et al., 2018). Alternatively, there is a vast number of more short-term sustainable activities that can be developed on landfill sites, for instance, focusing on optimized interim use, e.g., development of solar parks, production of green energy, or use as green space. These activities could be part of a more comprehensive, gradually implemented and adapting landfill management that could generate intermediate revenues and other benefits, as well as mitigate environmental risks for remediation and aftercare, and potential actual landfill mining on the longer term. In this view, the concept of Dynamic Landfill Management (DLM) emerged, capturing a broader range of objectives ranging from pollution prevention and remediation, land restoration, creation of new landfill void space, interim use of landfill surface and recovery of resources (Jones et al., 2018). Thus, DLM requires a reliable characterization and monitoring of landfills in order to allow an informed and sustainable management. In these applications, misjudgment on the current state of a landfill, on specific material characterization (Hernández Parrodi et al., 2019a), and its expected future evolution can have serious -economic and environmental- consequences when implementing suboptimal scenarios, e.g. greenhouse gas emissions in MSW landfills (Sauve and Van Acker, 2020). Conventional approaches to the characterization and monitoring of landfills rely on drillings or trial pits excavations, and subsequent sampling and analysis of the deposited waste. Yet, such methodology is generally expensive and invasive, requiring proper safety measures to limit risks for the environment (e.g., creating new contamination pathways) and for human health (e.g., exposure to dangerous materials). Furthermore, it may deliver results that are non-representative of the entire landfill as, due to the typically high heterogeneity of the waste depositions, the outcome may be strongly variable depending on the number, volume and spatial distribution of the samples (Dumont et al., 2017).

In this context, advances in non-invasive geophysical science and technologies for exploration have demonstrated their usefulness and remaining potential for further development and implementation in the future. To the best of our knowledge, the earliest geophysical survey conducted on a landfill dealt with contaminant detection (Cartwright and McComas, 1968). Since then, the investigations reported in the literature have significantly increased (Nguyen et al., 2018), although these mainly have been focusing on environmental risk assessment, and rarely on the potential opportunity of landfill mining, e.g., Vollprecht et al. (2019), nor on the optimization of short-term use of landfill sites, both of which would integrate them into the circular economy. The integrated use of multiple geophysical methods allows filling information gaps in the landfill characterization remaining after the analysis of historical archives and conventional investigation. They mostly provide complementary

information on the lateral and vertical extensions, and (indirect) indications of waste composition and conditions related to water or leachate content in MSW landfills, e.g., Clement et al. (2018), Moreira et al. (2018), Yannah et al. (2017). Yet, most of the existing geophysical investigations present a rather general and qualitative interpretation, although, there also have been efforts to quantify the landfill structure and dynamic landfill processes for further modelling (Dumont et al., 2016; Martin et al., 2020).

Waste materials of anthropogenic origin have widely varying physical properties, which may be very different from those of natural geological deposits. Furthermore, heterogeneous mixtures of waste materials present an extremely complex matrix in which highly variable and dynamic processes take place. In their turn, the latter also produce variations in physical conditions (e.g., water saturation and temperature) that contribute to the geophysical response of the whole. This may further add to the ambiguity of the interpretations of geophysical data and makes it more challenging to obtain high-resolution geophysical results. Therefore, it is important to also assess the uncertainty associated with geophysical results, which does not only originate from data processing. It can also be related to survey design, data acquisition (technical applicability of the methods), and interpretation of the data (e.g., derived final models can be influenced by subjective decisions). Examples of relevant issues that contribute to the uncertainty present and propagating through the entire data acquisition-processing-analysis-interpretation flow are given in Figure 3.2 (Van De Vijver et al., 2020).

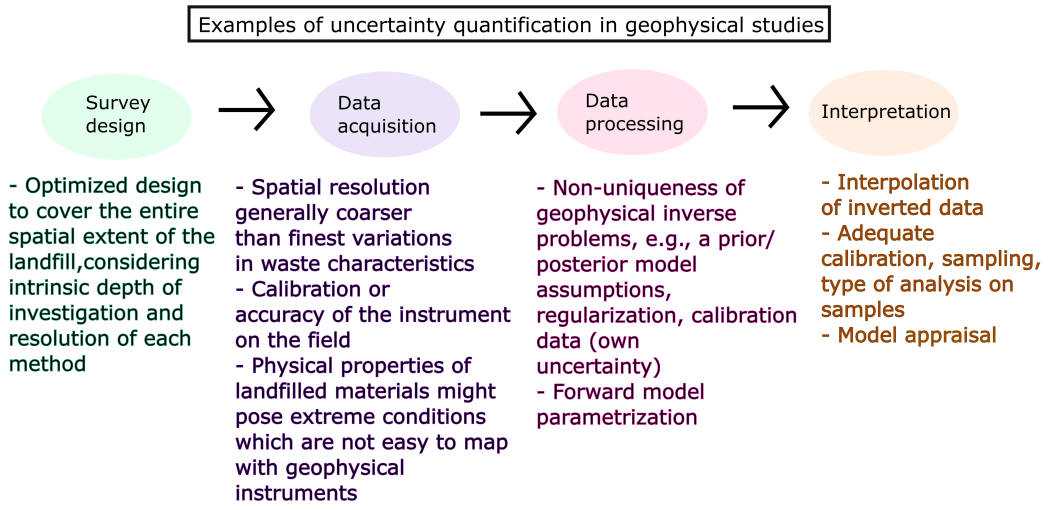

FIGURE 3.2: Examples on relevant uncertainties arising at different steps of a geophysical investigation.

The broader objectives of applied geophysics in the context of DLM requires the

methods, first, to be adjusted to the more specific quantitative targets and, secondly, to be more comprehensive in terms the spatial and temporal resolution required to use the derived data as decision support tools. We identified and reviewed three relevant targets for the selection of feasible (economic, effective and sustainable) scenarios for remediation/redevelopment and potential material/energy recovery. We focus on the quantification of 1) the landfill's geometry and waste materials, and the mapping of 2) leachate and 3) biogas distribution, the last two being the result of biodegradation processes in municipal solid waste (MSW) landfills.

The three specific targets which are relevant to DLM will be addressed in separate sections. In the first section, we show examples of how several geophysical methods are used for the quantification of landfill geometry and internal structure (zonation). We show the intrinsic limitations of the used methods in the particular environments of landfill sites and highlight the importance of considering the uncertainty in the geophysical results (see diagram in Fig. 3.2) and the corresponding computation of waste volumes, representing crucial information in view of material recovery and site redevelopment.

Secondly, we present geophysical investigations applied in leaching studies which particularly aim to quantify the water/leachate distribution by means of static characterization and/or monitoring. The third section is dedicated to the identification and delineation of gas accumulation in landfills and biogeochemically active areas. The multiple parameters that affect leachate generation and biodegradation in general, as well as the large heterogeneity in landfills, lead to preferential flow paths for leachate and landfill gas migration. This fact does not only make calibration and validation more challenging but also the uncertainty assessment in both data processing and interpretation of these complex processes. The fourth section shows an overview of the geophysical investigations carried out in metallurgical residues in specific, and describes how the integrated methodologies are adapted according to the characterization's objectives, e.g., mineralogical, chemical composition, etc. Finally, we describe the applicability of machine learning in the data processing and interpretation to target relevant objectives of DLM.

Note that the first section covers different types of landfills while the lasts are focused on MSW landfills. For a review of the basic principles of the different geophysical methods presented here, as well as an overview of their application to landfill investigations we refer to Soupios and Ntarlagiannis (2017). The novelty of this review is to address geophysical studies focused on filling quantitative information gaps in the three specific targets described above, which are particularly relevant in view of DLM.

3.2 Quantifying landfill's geometry

3.2.1 Estimation of boundaries and zonation

The quantification of a landfill's geometry includes the estimation of the boundaries of its outer extent as well as any internal zonation present. Several examples in the literature demonstrate the effectiveness of the use of multiple geophysical methods to perform this task. For example, Magiera et al. (2019) carried out a multi-methodological geophysical survey to delineate the horizontal and vertical distribution of waste from an ancient glass factory (composed of historical slags and ashes) mixed with modern bottom ashes and inert waste. First, magnetic susceptibility measurements on surface and on near surface samples collected in the dump and its surrounding environment (covering 7.2-ha) were used to discriminate the anthropogenic deposits from the natural soil. Subsequently, they combined magnetic gradiometry with electrical resistivity tomography (ERT), time-domain induced polarization (IP), electromagnetic induction (EMI) and laboratory analysis in material sampled from boreholes (up to 1.5 m deep).

In general, the horizontal distribution of wastes close to the surface has a rather straightforward interpretation, while the vertical extent of wastes often is a more challenging target, correspondingly associated with larger uncertainties. This was illustrated by Dumont et al. (2017) for a 26-ha engineered landfill with known boundaries, including the depth of the landfill bottom. The authors used the passive-source seismic method of horizontal to vertical noise spectral ratio (H/V) jointly with the active-source seismic method of multiple analysis of surface waves (MASW) and gravimetry to estimate the thickness of the waste deposit along a transect (see Fig. 3.3). This enabled to estimate the boundaries with a deviation of 5 m to 15 m from the known depth of maximum 60 m.

The computation of volumes based on those boundaries are therefore also strongly affected by the associated uncertainties and important to quantify for landfill mining initiatives. For example, Martínez-Segura et al. (2020) combined ERT with high-resolution topographic measurements to estimate the volume of waste deposits generated from a phosphoric rock derived fertilizer production unit. The volume was computed based on the comparison of the landfill top layer as represented in LiDAR measurements and the bottom layer of the waste deposits as derived from inverted ERT profiles. First, there is inherent uncertainty involved in the ERT inversion process, where the distribution of electrical resistivity is produced from the ERT measurements. It typically requires a prior geometric constraint (e.g., smoothness of the model, see section 2.3.2) on the resistivity model that may strongly impact the final

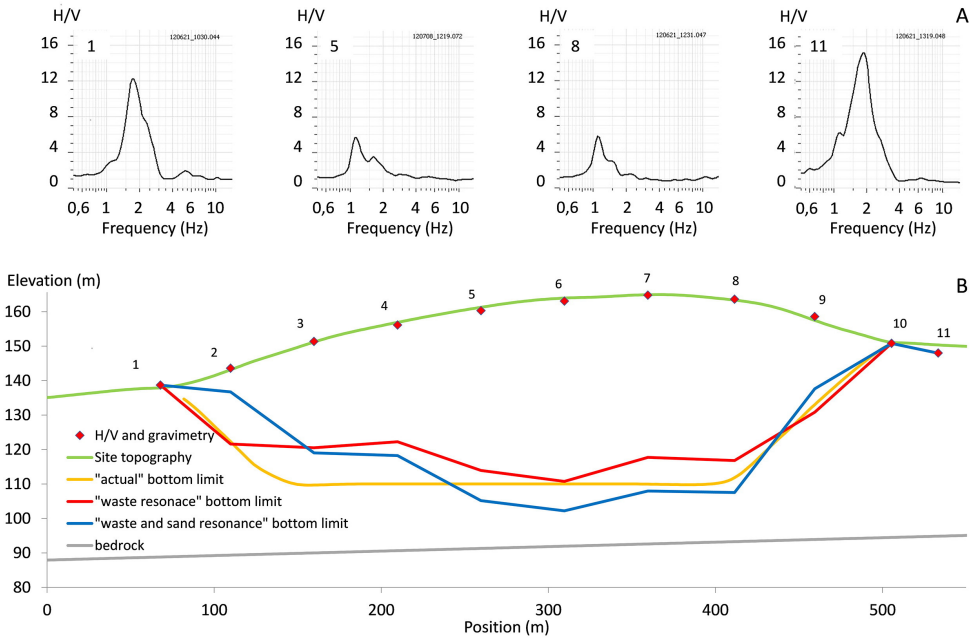

FIGURE 3.3: Estimated thickness along a transversal profile using the method of H/V (red and blue lines, considering one and two resonance peaks respectively). The topography is indicated with the green line and the real bottom limit of the waste is shown in yellow. Image from Dumont et al. (2017).

results (Caterina et al., 2013). Secondly, there is uncertainty in the interpretation of the inverted ERT profiles for the landfill boundaries using boreholes for validation. Although boreholes provide hard data with little uncertainty in the bottom layer at specific point locations along the ERT profiles, considerable uncertainties remained in between boreholes where ERT did not show a clear contrast between the waste and the host material.

Another example is given by Martin et al. (2020), who estimated the volume of ore processing residues in a mine waste dump by integrating ERT, ground penetrating radar (GPR) and spectral induced polarization (SIP) methods. The results were validated via drillings, mineralogical studies and laboratory SIP measurements on collected cores. GPR measurements allowed to distinguish between layers within the first upper meters of the fill while ERT mapped the (vertical and lateral) boundary with the host rock. To estimate the volume of the residues body, the authors relied on interpolated inverted 2D models and a threshold resistivity value derived from lab measurements. The uncertainties that the authors considered for the volume estimation were related to inaccessible survey areas, inversion coverage and small-scale anomalies of high resistivity (i.e. areas of low/no data coverage and anomalies were not considered in the volume computation). Based on this, a correction was applied resulting in the final volume estimation to be increased with 5%, obtaining a final

result of 81,900 m^3. Following the same procedure, two volumes were calculated using a lower and upper threshold limits of resistivity, obtaining a volume range of 63,000-108,000 m^3.

Cavalcante Fraga et al. (2019) used ERT and EMI to delineate laterally and vertically an unauthorized urban fill of 5-ha, composed of anthropogenic brown-to-green silt soils containing construction debris. The dump site is located in a suburban region, which is intended to host a commercial complex, hence the importance of an accurate geometrical characterization. To determine the depth of the interface between the urban fill and the geological substratum, 40 trenches were excavated placed in a non-aligned sampling grid of 33 m by 33 m. Here, the authors used the ERT inverted model as a reference to calibrate EMI data, helping to counter the poor sensitivity of EMI to resistive grounds and eliminating inverted deterministic 1D models with unrealistic parameters according to the site context. The EMI 1D inversion after calibration, indicated that the predicted urban fill thicknesses were consistent with 70 % of the ground truth values.

Besides, mapping the lower limit of a landfill might not always be physically possible. Apart from the uncertainty related to data processing from each geophysical method, the contrast between any physical property of the host material and the waste deposits must be large enough. Dumont et al. (2016) give an example of a study where the lower limit of the waste could not be resolved using electric and electromagnetic methods: first, because the ERT profile extension was limited by a road surrounding the landfill and the lateral walls of a bottom high density polyethylene (HDPE) geomembrane, and, second, because the high conductivity of the leachate concentrated most of the current density, causing the model sensitivity to rapidly reduce with depth. The use of mechanical seismic waves might fill in this information gap. However, low velocity contrast between the material of the landfill and the underlying media, may again significantly hamper the ability to delineate the bottom of the landfill using either active- and passive-source seismic methods. In general, MSW landfills present very low seismic velocities with S-wave velocities up to around 300 m/s and P-wave velocities up to approximately 500 m/s, e.g., Abreu et al. (2016), Balia et al. (2018), Yin et al. (2017).Thus, the thickness estimation of MSW deposits might be challenging in landfills located in “soft” soils such as sand, muds and alluvial deposits, e.g., Isunza Manrique et al. (2019b), but always possible on hard rock.

There have been fewer investigations aiming at identifying and estimating the volumes of different waste types (e.g., MSW, industrial waste), let alone different

individual waste materials proportion (e.g., plastics, metals and glass in MSW) deposited in the same dump. This represents an additional challenging task compared to estimating a single waste volume due to the high heterogeneity of landfills, the widely varying and unusual physical contrasts that might exist within waste materials and the effect that physical conditions (e.g., water saturation, temperature and compaction) have on the geophysical response.

Caterina et al. (2019) managed to estimate the respective volumes of three types of industrial waste, namely 1) industrial scrap and construction and demolition waste (CDW), 2) slacked lime, and 3) fly ash, using EMI, gradient and total field magnetometry, 3D ERT-IP and H/V (see Fig. 3.4). The high electrical conductivity of slacked lime and fly ash made it possible to determine the lateral (with EMI and magnetometry) and vertical extent (with 3D ERT/IP) of both materials overall. The H/V method was used to differentiate vertically between slacked lime and fly ash deposits. Two resonance frequency peaks were observed in several H/V locations at the top of these deposits and the peaks could be associated to the ash and slacked lime, respectively. This in turn allowed to estimate the bulk S-wave velocities of each material at the locations of two boreholes, enabling the use of a general formula (parametric analysis) to estimate the thicknesses of the deposits at locations where only H/V data were available. Thus, the volumes of the three waste deposits were estimated using EMI and magnetometry for the lateral distribution, together with a combination of the ERT inverted model (with a resistivity threshold <25 Ωm) and the thicknesses estimated via H/V for the vertical distribution of the slacked lime and ash. The results were validated via trial pits and laboratory analysis of collected samples.

In the view of ELFM, Vollprecht et al. (2019) associated magnetic properties of MSW to its iron content by conducting field and laboratory studies. The authors deployed a magnetometry survey and estimated the bulk magnetic susceptibility of the subsurface by modelling the total field response. For validation, drill core samples were sorted into different waste fractions (e.g., ferrous and non-ferrous metals, plastics, paper, inert, glass, wood, textiles) and its bulk magnetic susceptibility was measured in laboratory, using additionally reference samples of known composition from a different site. Whereas it was possible to distinguish the zonation of magnetic and non-magnetic materials, similar to the observations made by Yannah et al. (2017), the authors pointed out two outcomes underlining why quantifying the iron content based on magnetic measurements remains difficult: 1) even for wastes derived from known materials, landfilled materials show a highly variable bulk magnetic susceptibility, which can be likely be (partly) explained by degradation processes, and 2)

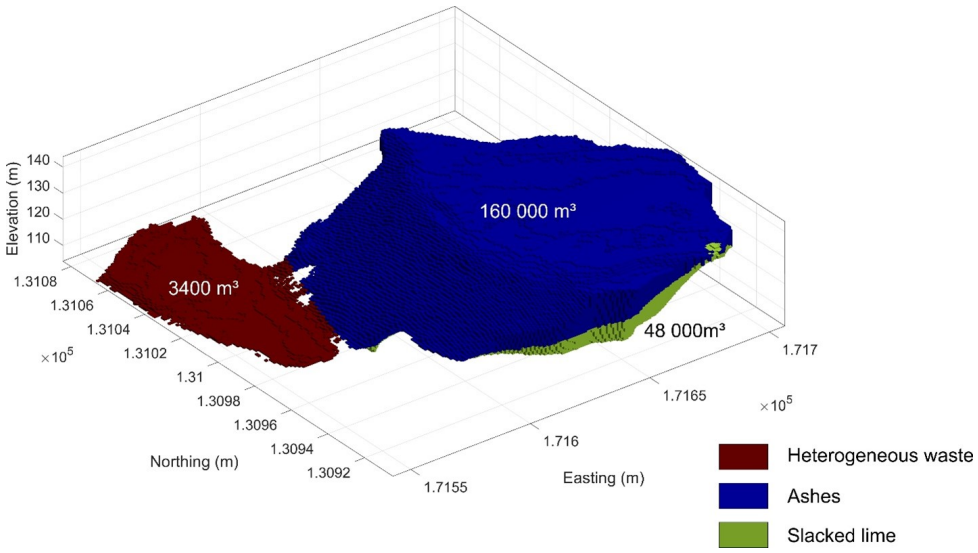

FIGURE 3.4: Estimated volumes of three industrial types of waste using multiple-geophysical methods, trial pits and lab measurements. Methodology described in Caterina et al. (2019).

the difference between the modeled data and experimental data (in this case derived from waste samples and reference samples), can be partially explained by scaling effects.

Mutafela et al. (2020) demonstrated that one single method, ERT in this case, may be able to distinguish a zonation within the landfill if the electrical contrast is unique within the waste body. The authors investigated a glass waste dump that covers approximately 38,500 m^2, and which contains MSW, crushed glass and some demolition waste from the glass factory. They identified buried glass hotspots in the dump as regions of high resistivity (>8000 Ωm), which afterwards were corroborated (via test pits excavations and laboratory analysis) to correspond with a composition with a mean glass fraction of 87.2%. Given that glass hotspots deposits were often located close to the surface, the ERT resolution remained sufficiently high.

3.2.2 Challenges and future directions

The above mentioned landfill geometry and zonation studies show that successful characterization is achieved when a target waste zone has a unique signature with respect to both the rest of the waste and/or the surrounding host material. These conditions allow to derive the required information by applying a relative simply procedure: defining a threshold value for (inverted) geophysical data that corresponds to the boundary of the zone of interest. In more complex cases, a solution can often only be achieved when multiple geophysical methods and/or modelling approaches are integrated. Inspiration may be found in methodologies used in natural geological

environments, for example, by applying a petrophysical joint inversion integrating electrical and seismic data in order to quantify the volumetric water, air, ice and rock contents in permafrost systems (Mollaret et al., 2020).

Additionally, the presented works illustrate the need to quantify the uncertainty of landfill boundaries and corresponding derived waste volumes. Whereas in general fairly accurate results can be achieved for rather shallow landfills (a few meters below the surface), the uncertainty of boundary estimates significantly increases when larger depths are targeted. While error propagation can relatively easily be incorporated into the data analysis, such as the impact of the threshold set on a volume estimation, e.g., Martínez-Segura et al. (2020), the conceptual choices that are underlying the error/uncertainty quantification, e.g., Dumont et al. (2017), should also be accounted for.

In this context, there is a need to provide a robust and commonly accepted methodology to provide "standards" for how uncertainties are to be quantified, accounting for the most important factors described in Figure 3.2. There are methodologies available, applied in natural geological environments, that include the quantification of uncertainty using probabilistic formulations to solve the geophysical inverse problem, for example, to "better" resolve the geometry of different subsurface units (De Pasquale et al., 2019). In hydrogeology and hydrogeophysics, Linde et al. (2017) reviewed the uncertainty quantification in both the forward problem and the solution of the Bayesian inverse problem and discuss, for instance, the use of proxy-modeling strategies and multi-resolution (multi-level Monte Carlo) methods to mitigate computational costs of forward uncertainty quantification. The integration of such approaches would lead to an improved interpretation of geophysical data, using a decision analysis based on probability theory, that in turn would improve decision making in DLM.

3.3 Mapping dynamic processes: leachate and landfill gas in MSW

3.3.1 Leachate

The disposal of waste in landfills leads to the generation of leachate, which is a polluting effluent with a high concentration of organic material composed of humic and nitrogenous compounds, heavy metals and inorganic salts (Costa et al., 2019). In a landfill bioreactor and/or engineered landfills, however, waste stabilization can be

enhanced and accelerated, primarily, through leachate recirculation systems. Characterization of landfill leachate is complex due to the presence of multiple contaminants and because leachate is also affected by the landfill age and its interactions with the surroundings, i.e., rainfall, surface runoff, climate and groundwater infiltration (Miao et al., 2019).

The presence of leachates generally leads to lower electrical resistivity values due to their elevated concentrations of total dissolved solids (Mirecki and Parks, 1994). This permits the use of static and time-lapse ERT to characterize the leachate distribution and migration patterns in the waste deposits (Chambers et al., 2006; Maurya et al., 2017), and potential pollutant leakages in the vicinity of a landfill (Moreira et al., 2018). Nevertheless, the heterogeneity of landfills can cause significant extra complexity, for instance, due to the creation of preferential flow paths for leachate transport which in their turn might form subsurface canals and perched water bodies in the wetland system (Wijesekara et al., 2014).

For problems involving optimization of a landfill infrastructure (i.e., design of control and collection systems of leachate and gas emissions), it is important to have a better understanding of unsaturated flow theory to improve the study of the migration of leachate and landfill gas (Feng et al., 2017c). Thus, it is critical to understand the unsaturated properties of MSW landfills such as volumetric and gravimetric water/leachate content, intrinsic/relative permeability, water retention capacity, as well as the spatio-temporal variation in these properties. In addition, there are multiple interacting parameters that strongly affect the leachate generation and, hence, should be considered in the modeling of this process (e.g., infiltration of rainwater and seasonal variations, temperature, moisture content, geographical features like topography). Here, we review the recent literature available on the quantification of water/leachate content in both static characterization and monitoring studies.

Static characterization

Dumont et al. (2016) estimated the gravimetric water distribution in a MSW landfill along an ERT profile, intersecting a 32-m deep borehole in which complementary EMI tests were performed. From the same borehole, waste samples of a few dm^3 were collected every 2 m and analyzed for gravimetric water content, temperature and volumetric water content, as well as the electrical resistivity. Using the Archie's and Campbell's petrophysical laws (Archie, 1942; Campbell et al., 1949), the entire profile of electrical resistivity values was translated into a profile for gravimetric water content. Additionally, the authors provided a hypothesis on the vertical evolution of salinity with depth in the unsaturated zone. They concluded that established

petrophysical laws can be accurately used in MSW landfills, provided that the temperature, compaction and salinity evolution with depth can be assumed stationary and sufficiently accurately approximated by in situ measurements, in this case made in one borehole. Neyamadpour (2019) extended this approach to a 3D ERT set-up combined with sample analysis from several boreholes and reported a good fit of Archie's law at the different boreholes (R^2 = 0.79). This indicates that the vertical evolution of the influencing factors of the temperature, compaction, and salinity is a major factor in explaining the leachate distribution in landfills.

Ignoring these specific conditions may lead to important uncertainties. For example, Feng et al. (2017a) used an empirical Archie law in a similar approach as Dumont et al. (2016), but without including a temperature correction, nor accounting for any other influencing parameter. The underlying assumption was that the effects of these parameters on the electrical resistivity are negligible, mainly because the studied waste areas were either in a stage of anaerobic biodegradation or already stabilized. A temperature gradient was observed, from an ambient temperature of 25°C to a temperature of 35°C at the bottom of the waste, but was considered to be small. However, this already produces a 20% error in the estimation of the bulk electrical conductivity used to estimate the water content. In general, the electrical resistivity tomography is a method that has been used as an indicator of temperature variations, for example, in shallow geothermal systems (Hermans et al., 2014). Considering that the correction factor for compaction is five times as high as the temperature one (Dumont et al., 2016), ignoring compaction is likely to lead to an even greater additional error in terms of water content estimation.

The hydraulic conductivity is a determining factor in water and leachate migration, which can even occur outside of the landfill, and has been estimated using geophysical methods. For example, Fiandaca et al. (2018) predicted the permeability at field scale in heterogeneous lithologies and water chemistry. The data were collected in an aquifer contaminated by a leachate plume from a landfill nearby. They used spectral induced polarization (SIP) data measured in 3 boreholes in an undisturbed formation, using the logging-while-drilling technique with a 0.2 m vertical resolution and extending the measured data to time domain SIP (Gazoty et al., 2012). A very good correlation was found between time domain SIP-derived permeability estimates and those derived in an experimental approach based on sample grain size analysis and slug tests. The total uncertainty on the SIP-derived permeability estimation depended on the uncertainties of the petrophysical relations and the inversion parameters.

Already for decades, IP investigations have been applied to target leachate plumes

in landfills, often jointly interpreted with ERT, e.g., Abdulrahman et al. (2016). Balbarini et al. (2018) propose a geophysics-based interpolation method to estimate a contaminant mass discharge from a landfill to complement the results from a conventional investigation campaign with a low spatial sampling density. The method is based on finding a conceptual link between the bulk conductivity from inverted geophysical models and the concentration of contaminants. To this aim, ERT and time-domain IP were applied to a wide leachate plume (with high concentration of inorganic and pharmaceutical compounds) downgradient from the landfill. The limited number of spatially discrete contaminant concentrations data were interpolated through regression kriging, using the geophysical models as dependent variable. The use of the bulk conductivity from geophysics to describe the distribution of the contaminant concentration was assessed at co-located observations, were the relative contaminant mass discharge estimation error and relative uncertainty were also computed. Here, it was possible to estimate the contaminant mass discharge of chloride and pharmaceutical compounds in the landfill.

A methodology for leachate detection in a MSW landfill based on statistical analysis of ERT and IP data were presented by Frid et al. (2017). To mitigate the variations in the different inverted models, the authors computed the statistical distributions of 1) the inverted electrical resistivity, 2) the chargeability, and 3) the ratio of chargeability to electrical resistivity models. Then, the three models were standardized to have a mean of zero and a standard deviation of 1. These values were used to define the likelihood of an anomaly through the computation of probabilities (for each model) which were jointly interpreted for the distribution of leachate in the landfill. The study was combined with synthetic modeling and analysis of the relationship between bulk and fluid electrical resistivity, which was validated by test borehole drillings. Leachate detection could be successfully performed using the chargeability-to-resistivity ratio with the anomaly's likelihood being higher than 90%.

Baawain et al. (2018) provide an example where greater investigation depths (75 m) are reached in an unregulated landfill by using TDEM to identify leachate contamination and image the plume migration by investigating preferential flow paths. Here, the installation of monitoring wells and piezometers, combined with sampling for chemical analysis, was used to verify the geophysical results. This approach confirmed the migration of contaminant plumes derived from previous domestic waste disposal and possibly waste oil from auto-garages. Anomalies encountered below 80 mbgl (meters below ground level) were related with the groundwater table.

Similarly, Høyer et al. (2019) built a 3D geological model for the surroundings of

a former landfill, to assess the risks for landfill leachate migration. TDEM and FDEM measurements were combined with geoelectrical profiling, analysis of the geomorphology, and spear-auger mapping. The immediate risk for leachate migration was found downgradient through a lacustrine sandy aquifer and wetlands. Finally, also using TDEM, Feng et al. (2020) assessed the leachate leakage of a MSW landfill to evaluate the safety of the construction and operation of a tunnel underneath the landfill. The investigation included an ERT and TDEM data acquisition together with drilling and water sample analysis from boreholes.

Seismic methods are scarcely used to characterize parameters and processes related to leachate plumes. Nevertheless, Konstantaki et al. (2015) performed active-source seismic reflection and ERT surveys to understand the flow inside a landfill (household, CDW) in order to optimize processes such as irrigation and leachate recirculation. They calculated the density distribution in the landfill using an empirical relationship between S-wave velocity and unit weight (proportional to bulk density), concluding that high-resolution seismic reflection methods seem to be more reliable for imaging and monitoring a heterogeneous landfill, as compared to multiple analysis of surface waves (MASW). The empirical relationship they used was derived by Choudhury and Savoikar (2009) from a database of laboratory and field tests, including data on different physical properties (e.g., unit weight, S-wave velocity, strain dependent material damping ratio, consolidation modulus), collected from more than 30 landfill surveys.

Monitoring

Rather than mapping the water content at a particular time, it is often of interest to monitor its evolution over a certain time period. This can be done without quantifying the water content variations as intermediate step, such as in Dumont et al. (2018) where the authors' aim was to assess the efficiency of horizontal drains in a landfill bioreactor by using 2D time-lapse ERT, 3D ERT, and distributed temperature sensing (DTS) vertically in a borehole and along the horizontal drain, in order to determine an optimized water injection protocol. They highlighted that the horizontal anisotropy in the water flow is due to the compaction of the waste layers.

In general, customized data acquisition and processing schemes have been developed to accurately map the spatial distribution of leachate and better understand its hydrodynamic behavior. Audebert et al. (2014) noted that the inversion of time-lapse ERT data could be problematic for an accurate delimitation of the infiltration area due to the ambiguity in the parameters set and smoothness of the inversion. To improve

the ERT imaging during a leachate recirculation experiment on a landfill bioreactor, the authors proposed a methodology based on multiple inversions and clustering. First, they performed several inversions by varying inversion parameters, then clustering on each resistivity model (considering two groups: leachate infiltration area and surrounding waste medium) and finally a grouping approach for the integration of all clustering results into one final cross section.

Seismic methods have been scarcely applied in leachate monitoring. For example, Carpenter et al. (2013) explored the use of seismic surveys to characterize changes in the dynamic properties (e.g., shear wave velocity, Poisson's ratio) of a MSW landfill to infer the spatial extent of degradation. The authors collected data in a bioreactor cell by using fan shot direct P- and S-wave surveys, together with repeated EMI measurements. Although the study provided useful information on the effects of leachate recirculation on shear modulus and Poisson's ratio of MSW landfills, additional information such as the independent direct measurements of material density and velocity are needed for calibration, as well as a characterization of the MSW of different ages.

Despite the general small depth of investigation of GPR in conductive media, Carpenter and Reddy (2016) applied this method to investigate a leachate recirculation system in a MSW cell, reaching a depth of around 8 m (with an antenna with a center frequency of 50 MHz). The radargrams imaged reflections that could relate to intermediate cover layers, layers of different types of waste, leachate recirculation lines or leachate accumulation. In addition, geophysical well logging with natural gamma and electromagnetic conductivity probes was conducted to characterize waste in-situ and identify leachate accumulations.

The integration of multi-geophysical investigations mitigates the ambiguities and shortcomings inherent to each method. For example, integrating geochemical and geophysical ERT, spontaneous potential and FDEM results, Alam et al. (2018) located a highly conductive zone caused by the accumulation of contaminants from a leachate plume, which was validated by chloride concentrations from total dissolved salts (TDS). Also, Giang et al. (2018) used ERT, self-potential and VLF methods in combination with hydrochemical analysis to assess the impact of a landfill in the subsurface geologic formations and the hydrogeological environment. They could detect a low resistivity area associated with a fully leachate-saturated zone in the landfill.

Challenges and future directions

From the above mentioned contributions, it can be concluded that resolving the spatial distribution of water/leachate content and its evolution in time (e.g., related to

leachate injection or dewatering) can be considered as the state-of-the-art solution in monitoring landfills. Nevertheless, the quantification of underlying parameters (e.g., hydraulic conductivity) in highly heterogeneous environments and subsequent modeling (e.g., flow and transport) using hydrogeophysical approaches still faces unaddressed challenges. A first difficulty is linked with the non-stationarity of petrophysical relationships, particularly in multiphase systems with highly variable temperature (bioreactor). A second difficulty is the typically large anisotropy due to different waste compaction levels which can lead to preferential flow paths.

In their review, Slater and Binley (2021) promote the use of hydrogeological observatories to provide insight into hydrogeological processes through long-term ERT monitoring. The authors also emphasize the importance of taking into account the additional uncertainty that time-lapse inversion and interpretation problems pose (e.g., petrophysical model uncertainty and lab-to-field calibration uncertainty). If we translate this to the study of leachate dynamics in a MSW, the potential integration of a permanent ERT system within an engineered landfill cell or a bioreactor together with the use of other sensors could help developing more representative leachate-waste interaction models from geophysics. Furthermore, efforts are being made to consider more realistic three-dimensional modelling of coupled leachate and gas flow in landfill bioreactors (Feng et al., 2017b). In addition, combining ERT monitoring with other methods such as IP and self-potential data could better resolve the leachate spatial distribution and its evolution over time (Flores-Orozco et al., 2020; Helene and Moreira, 2021).

3.3.2 Landfill gas

MSW landfills are by nature reactors in which degradation of organic materials in anaerobic conditions lead to the production of landfill gas, mainly composed of the greenhouse gases methane and carbon dioxide (Shen et al., 2018; Williams, 2005). The accumulation of gas might pose a risk of explosions, fires–both at the surface and underground (due to anthropogenic activities at deposits with flammable waste), or spontaneous combustion of the waste. Additionally, there is an environmental risk of pollutants and greenhouse gas emissions migrating into the air, water or geological host (Frid et al., 2010). In this context, landfill bioreactors are a sustainable option wit a landfill gas energy recovery, designed to achieve a stabilization of the waste within 30- 50 year time span (Williams, 2005).

In general, the rate of gas production in a landfill is a function of waste composition (organic content), age or time since deposition, climate variables, moisture content, particle size and compaction (Georgaki et al., 2008). Despite the frequent

monitoring of gas emissions and site investigations that might be possible in a landfill, waste heterogeneities can create lateral migration paths for the gas, and, therefore, gas emission measurements can often only be considered rough estimations.

In the last decades, geophysical methods – in particular ERT and IP – have been used to investigate the gas distribution in landfills and the related processes of degradation and contaminant transport. In this section, we present geophysical investigations that aim, first, to detect and image gas accumulations within the landfill body and, second, to investigate variations in biogeochemical parameters that are related to biodegradation.

Gas accumulation

The detection of subsurface gases is inherently difficult in geophysics as their diffusive nature makes them less likely to produce detectable contrasts in geophysical measurements. Gas accumulations, trapped because of the presence of less permeable layers, however can show a relatively large contrast in many physical parameters, including mechanical, electrical, e.g., Frid et al. (2010), and electromagnetic ones. Yet, in both scenarios the validation of the geophysical interpretation using ground truth data is particularly challenging. The literature provides studies performed in the laboratory and in situ. In the former, the limited volume allows for the gas to be detected by geophysics, e.g., Zhan et al. (2019), but the latter yield more uncertain outcomes as will be shown in the discussion of the studies of Jacome et al. (2021) and Konstantaki et al. (2016) below.

In his work, Jouen (2018) presents an overview of how biodegradation processes can influence multiple geophysical methods both at laboratory and field scale. Overall, the ERT monitoring studies performed over several months (or years) indicate that the resistivity decreases with time, which is often attributed to an increasing water content. Additionally, the response of IP in time- (chargeability) and frequency-domain (phase shift) increases at laboratory scale with decreasing density, and, at field scale, the response decreases during biodegradation and a density increment. Moreau et al. (2012) also studied the impact of waste biodegradation on resistivity at laboratory scale. Here, the authors pointed out that biodegradation of organic fractions could induce modifications of mechanical and chemical characteristics of porous media and leachate composition.

Zhan et al. (2019) carried out several ERT tests in a large-scale ($5 \times 4 \times 7.5$ m) landfill bioreactor to investigate the possibility of detecting liquid and gas accumulation zones in wet MSW landfills (under presence of leachate). This large-scale experiment was instrumented to monitor temperature, earth pressure (vertical and

horizontal stress), settlement, moisture content and leachate level with simultaneous time-lapse ERT measurements, the authors identified irregular spatial variations of high-resistivity zones observed below the leachate level, which were associated with the accumulation and dissipation of gas pressure. Monitoring and quantifying these parameters allowed to better understand the gas accumulation and migration dynamics, which is essential for safety assessment and management of a wet MSW landfill. In an in-situ study, Júnior et al. (2016) detected small continuous voids and large voids within the waste mass using GPR (with maximum penetration depth around 5 m). The small voids were considered to be possible indicators of slip surfaces, due to the clear dielectric contrast between the air and the MSW, and the larger voids possible indicators of greenhouse gases pools.

More recently, Jacome et al. (2021) developed an approach to predict methane generation rates in a non-engineered closed landfill. The algorithm, based on ERT, IP and point-source methane concentration measurements, incorporated fuzzy logic to neural networks for causal variable forecasting of surface methane concentrations, using geoelectrical proxies of leachate accumulation (taken from the ERT and IP inverted models). This hybrid algorithm provided a statistically significance inference of the effects of the processes linked to methane production on which little (experimental) control is possible (i.e. biological mechanisms affecting organic matter degradation, moisture content, temperature and pressure of the system, anaerobic decomposition rate in leachate, and flow rate of water in the waste, among others). Some uncertainties that might hamper achieving a better inference are moisture, temperature and features such as discontinuities, fissures and cracks in the cover soils, which could qualitatively explain the distortions in the relationship between methane emissions and geoelectric parameters.

Active source seismic methods have also been used to investigate landfill gas. Konstantaki et al. (2016) analyzed shallow S and P reflection data and surface-wave data acquired at a landfill where biogas was extracted. Jointly interpreting the P- and S-wave velocity fields, together with the location of distinct scatterers, the authors interpreted wet and gassy (dry) zones in the landfill (Fig. 3.5). Gassy or air-filled pockets were interpreted considering abnormally low P-wave velocities estimated from body and surface wave seismic data. A validation was done by performing independent field measurements of biogas flow and mechanical tip resistance on the waste in shallow wells, which were in agreement with the spatial delineation of stiff and soft zones and wet and gassy areas interpreted based on seismic data.

Finally, the use of passive source seismic methods can potentially provide useful

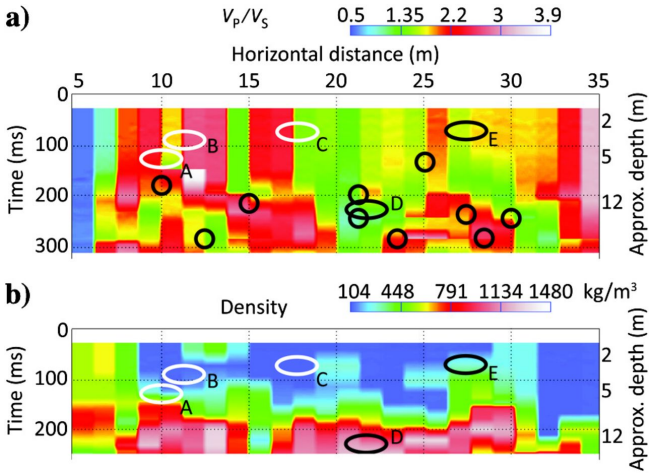

FIGURE 3.5: a) The VP/VS field and b) density field. White and black ellipses indicate the interpreted water-bearing and gas/air-bearing zones respectively (interpreted from S and P-wave reflection data). Black circles mark locations where velocity estimates are relatively uncertain. Image from Konstantaki et al. (2016).

information for monitoring landfills. For example, the evolution of the seismic velocities and induced pressure variations have been studied in a natural gas field, using passive seismic ambient noise during the gas production (Brenguier et al., 2019).

Biogeochemically active areas

Flores-Orozco et al. (2020) applied frequency-domain IP, together with excavations at several locations, waste samples collection and chemical analysis, to discriminate between biogeochemically active and inactive zones – in terms of production of CO2 – in a MSW landfill. The total organic carbon (TOC) content in the leachate of solid waste samples was used as a proxy for microbial activity. A positive correlation between the leachable TOC concentration and the polarization effect was observed, both for the imaginary component (r=0.9) and the phase of the complex conductivity (r= 0.79). Correspondingly, low polarization values were observed in microbiologically inactive areas while the highest values were observed in microbiological hot spots associated with high leachate and landfill gas production (see Fig. 3.6).

To improve the estimation of surface gas emissions from a landfill, Georgaki et al. (2008) acquired several 2D ERT profiles together with boreholes and CH4 and CO2 emission measurements using the static chamber technique (SCT) (Czepiel et al., 1996; Hellmann et al., 1997). Then, a classification of the landfill content was done based on the ERT results, data on the properties of the waste/bedrock obtained from the boreholes and chemical analysis: organic waste, organic waste saturated in leachates, low organic and non-organic waste. The classification was done measuring

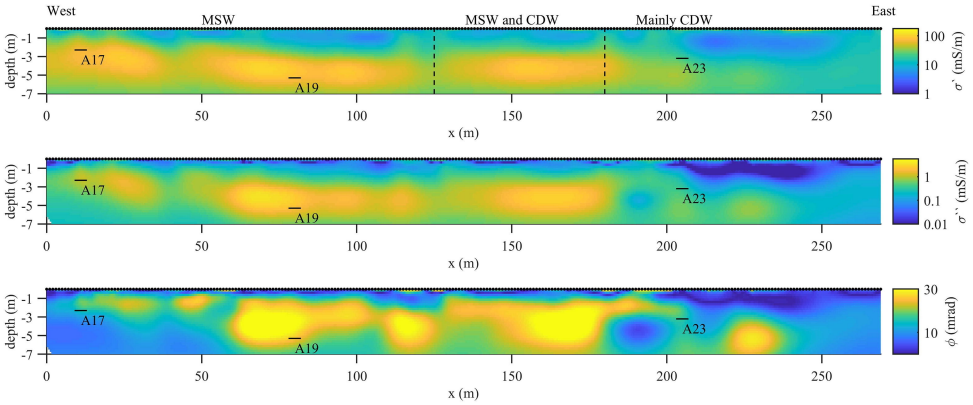

FIGURE 3.6: SIP results for the real and imaginary component of the complex conductivity (first and second row) as well as their ratio expressed in terms of the phase of complex conductivity. Solid black lines indicate the bottom of the landfill observed in excavations. Image from Flores-Orozco et al. (2020).

the electrical conductivity in liquid samples and applying explicit limits of resistivity ranges. In general, areas of high gas emission rates were strongly affected by the thickness of organic waste and organic waste saturated in leachates underneath. The combined use of ERT and SCT represents a cost-effective, reliable, and easily conducted approach to estimate the gas emission rate in a landfill, that allows to reduce the number of gas sampling points. However, SCT cannot estimate emissions in places where surface leachate or precipitation might block the emission of gases.

Naudet et al. (2003) applied the self-potential (SP) method to investigate a contaminated groundwater plume originated from a MSW landfill. The measurements were performed downstream of the landfill and complemented with sampling from piezometers and wells for geochemical measurements to delineate redox fronts in the contaminant plume. The results showed a large negative SP anomaly ($\approx$ -400 mV) with respect to a reference SP station positioned outside the plume. The origin of SP has two main components: the electrokinetic contribution associated with groundwater flow in permeable soil and redox phenomena. In this work, the first component was removed, and the residual SP signals were linearly related (R^2 = 0.85) with in-situ measurements of redox potential. Then, a quantitative relationship between SP and redox potential was proposed, in order to invert SP measurements in terms of in situ redox potential values in contaminant plumes. Afterwards, this method was also applied on a MSW landfill composed of 15 m thick cells, filled with half MSW and half of industrial waste. The SP signal was mainly influenced by the biodegradation of the waste with negative values being observed on the more mature cells (Naudet et al., 2012).

More recently, Moreau et al. (2019) monitored the biodegradation phases of non-hazardous waste mass, by studying the spatial distribution and temporal evolution of the temperature in a MSW cell. To this aim, they used distributed temperature sensing (DTS) with optical fibers installed in the bottom part of the waste mass for a monitoring period of six years. After landfilling, the temperature of the waste increased (up to 65 °C) due to the exothermic reactions in the aerobic biodegradation phase (< 1 year), followed by a more gradual decrease in temperature during the anaerobic biodegradation phase, which was spanned over a period of 6 years. The rate of temperature decrease during this period of time, is strongly affected by external conditions on the points closest to the edges of the cell, while the center of the waste mass remains warmer. Nevertheless, the heterogeneity of the waste mass was not identified in the temperature variations and the waste is considered as one bulk unit. In addition, a numerical simulation was performed to reproduce the temperature evolution and spatial distribution, enabling to predict if the waste reached the temperature conditions to promote methanogenesis biodegradation. Over the simulation period, the differences between the measured and simulated temperature values decreased in time.

Challenges and future directions

Gas accumulation and biodegradation zones may be detected using geophysical methods provided that their volume is sufficient to be spatially resolved by the method and the associated contrast in the investigated physical property is sufficiently large, i.e. dominant over the variations of other influencing properties. Whereas this is almost always the case for laboratory studies where the volume is controlled, it is more challenging in field applications.

The quantification of landfill gas concentrations in a landfill remains difficult as several parameters must be monitored simultaneously to enable inferring reliable conclusions. Yet, in more general applications, ERT has been largely used to monitor gas dynamics in the subsurface (Slater and Binley, 2021). As resistivity increases when gasses replace water in the pore space, then greater electric contrast will be observed if gas pockets are present.

To improve the monitoring, there is a need to improve the temporal and spatial resolution of geophysical imaging, and to advance our understanding of processes related to biodegradation coupled with non-invasive geophysical monitoring, e.g., coupling of IP with direct biogeochemical measurements and mechanisms models, see Kessouri et al. (2019). Similar to the directions mentioned for the study of leachate,

the integration of permanently installed geophysical sensors in boreholes could improve the understanding of the production and transport of biogas and other reactions in engineered landfills. Downhole geophysical tools in boreholes have proven efficient in offering high temporal and spatial resolution measurements together with monitoring and pumping wells, see Tal et al. (2019), who monitored seawater intrusion through electrical resistivity measurements.

3.4 Quantitative studies in metallurgical residues

Geophysical methods have proven useful to characterize specifically metallurgical wastes and associated contamination. To this aim, magnetic and electromagnetic methods have been successfully used, often qualitatively, to identify these deposits (Ivančan and Karavidović, 2021; Mendecki et al., 2020) and in most cases, geoelectric methods (Florsch et al., 2012, 2011). However, as indicated in Placencia-Gómez et al. (2015), using DC-resistivity or electromagnetic methods alone, may be challenging to identify critical zones of oxidative-weathering of metal sulphides present in tailings or the zones associated with the precipitation-adsorption of secondary minerals. Nonetheless, time-domain IP and SIP, represent a promising method that has been applied both in the laboratory and in the field to investigate the chemical form and physical properties of these residues, as well as dynamic processes within them (Revil et al., 2022).

3.4.1 Metallurgical zonation

Beyond the use of geophysical methods for the estimation of volumes in metallurgical wastes (dusts, slags, tailing waste, etc.), comprehensive characterizations such as mineral or metallurgical zonation, may require integrated approaches to link geophysical measurements in the field and/or in the laboratory with optimized field sampling and metallurgical or geochemical analysis. For example, Martin et al. (2021) studied slags derived from historical processing of metal ores using SIP in the laboratory and in the field. Samples were collected at maximum depths of 0.5 m in which SIP measurements and geochemical-mineralogical analyses were carried out. Then, two 2D SIP profiles were measured in the field and interpreted through a classification in terms of different types of slags grades, based on the varying spectral polarization behavior identified in the laboratory (and based on the fact that few SIP data has been collected on the last three decades, leading to limited spectra types). Qi et al. (2018) measured SIP in the laboratory and stablished a relationship between the chargeability and the volumetric metal content at lab scale. This relation

was translated to a 3D time-domain IP acquisition to quantify the metallic volume of a slag heap imaging the metallic volume fraction zonation. Other integrated approaches may include several methods as in Pierwoła et al. (2020), where they used ERT, time-domain IP, electromagnetic mapping and magnetometry combined with geochemical analyses, to identify the spread of pollution zones around a tailing pile.

More recently, Lévy et al. (2019) have linked field and laboratory measurements by qualitatively comparing inverted spectral parameters from time domain 2D IP-ERT field data with in situ borehole measurements, SIP laboratory measurements and mineral distribution analysis. The methodology allowed discriminate between zones rich in pyrite from those zones with iron oxides (magnetite-rich) in a geothermal area. Similarly, Bortnikova et al. (2017) used field and laboratory measurements mainly to study the trace element transfer from waste heaps of metallurgical slags. The measurements included, among others, thermometric mapping and chemical analysis, that allowed to qualitatively interpret the ERT data in terms of zones of frozen and wet slags, slags saturated with highly mineralized solutions, and a zone potentially associated with a combustion center.

3.4.2 Mapping dynamic processes

The complex dynamic behavior of metallurgical residues and associated contamination has also been investigated using mostly SIP at laboratory scale. For example, Placencia-Gómez et al. (2015) conducted SIP laboratory measurements together with mineralogical and geochemical analysis to study tailings from an Au-Cu mine, showing the ability of the method to resolve oxidation-based textural features of the tailings (e.g., acid mine drainage discharges). Similarly, Fernandez et al. (2019) investigated SIP as indicator the development of reducing conditions during degradation of organic contaminants at the water table interface, proposing that the method is sensitive to the anaerobic dissolution of iron and manganese oxides. Furthermore, there have been investigations that aim to develop potential applications tailored to remediation of mine wastes. For example, Slater et al. (2007) studied the SIP signatures of iron sulfide biomineralization induced by sulfate reducing bacteria in the laboratory, for potential contaminants degradation using wetlands and biostimulation strategies.

For methodologies applied in the field, we can refer to Kessouri et al. (2022) who conducted a post-remediation assessment in a chlorinated-contaminated aquifer several years after amendment delivery, using surface resistivity imaging, and cross-borehole resistivity and time-domain IP. Aqueous chemistry analysis, natural gamma and magnetic susceptibility logs supported the interpretation of geophysical data,

which indicated that the formation of (polarizable) iron sulfide minerals are associated with the long-term impact of the aquifer's remediation.

IP method has also proven useful for monitoring as shown in Saneiyan et al. (2019), who used IP to delineate spatially and temporally the propagation of microbial induced carbonate precipitation in a vanadium-uranium processing facility field during 15 days. It has been suggested that IP is a promising method for the long-term monitoring of soil stabilization.

Geoelectric methods have been ultimately used as complement in secondary recovery applications. For instance, Rucker et al. (2009) used ERT to monitor a secondary recovery process involving high-pressure injections of leachate into an engineered (leach) heap of a mine with sediment-hosted gold. The leachate injections were monitored trough two injection wells and surface ERT for seven days. During this period ERT was able to identify the leachate distribution and zones of low permeability as well as to infer in the moisture content variations in time. As a subsequent work, Rucker et al. (2014) proposed to rather monitor the raw current output and voltage on a network of borehole electrodes installed around the injection well. In this way, the authors suggested to use the method as a real-time tracking of leachate distribution in the subsurface.

3.5 Applications of machine learning

Recently, there is an increasing use of machine learning in geosciences using both supervised and unsupervised learning algorithms for a broad range of applications (Yu and Ma, 2021) including few investigations on deposits of different types of residues.

In terms of environmental risk assessment, Sun et al. (2023) designed a deep network for multi-view fusion to invert the resistivity distribution and infer the leachate distribution in a hazardous waste landfill. The model was developed and validated using inverted ERT data from synthetic models and a salt tracer experiment using different electrode arrays. Jacome et al. (2021) investigated a non-engineered closed landfill combining ERT and time domain IP with measurements of methane concentrations collected over the landfill. The authors applied a hybrid algorithm that combines fuzzy logic to neural networks to predict surface methane concentrations using the ERT/IP data as proxy indicator of leachate accumulation. Unsupervised learning has also been applied to improve the geophysical imaging of leachate distributions. For example, Piegari et al. (2023) used k-means cluster analysis on ERT

and IP inverted data to better interpret leachate accumulation zones in urban landfills (one MSW and an unknown type of landfill).

Regarding the investigations on metallurgical residues, Zhang et al. (2023) studied a mine tailing pond using an unmanned aerial vehicle with an hyperspectral sensor and collected 74 soil samples in which available copper content and soil organic matter were measured. Then, the hyperspectral data were processed, and the simulated annealing deep neural network was used to predict the available copper and organic matter.

Machine learning algorithms are useful in the investigation of anthropogenic residues provided that there are enough data for training (supervised learning). Appropriate training in machine learning can lead to results that outperform standard (less informed) inversions (Moghadas and Badorreck, 2019; Sun et al., 2023). However, this may not always be the case in these environments where often ground truth data is limited. A common practice is to create synthetic data to complement the training data available (Yu and Ma, 2021). Nonetheless, synthetic models may not accurately represent highly heterogeneous landfills, integrating varying parameters such as temperature and salinity, and processes developing within the waste. Hence the need for more robust methods that allow a quantitative interpretations of geophysical data presenting results that can be used as decision support tools in a sustainable landfill management.

3.6 Discussion and general conclusions

Multiple surface geophysical methods have proven useful to investigate the geometry and the zonation of a landfill – depending on the contrast of physical properties within the waste and between the waste and the host geology. Yet, there is a need to take into account the uncertainty at the different steps of a geophysical investigation, when targeting the quantitative characterization of waste volumes, and temporal and spatial variations of waste processes. Table 5.1 presents an overview of some works that show the applicability of different surface geophysical methods for several objectives as well as the type of interpretation developed. The aim of this table is to illustrate whether the interpretation offers quantitative information in different types of landfills or deposits.

Regarding the uncertainty quantification, Bayesian frameworks are an option to explicitly express the uncertainty on inversion results, e.g., Bobe et al. (2020), on the data interpretation in combination with sampling data (Hermans and Irving, 2017;

Isunza Manrique et al., 2019a), and to quantify the uncertainty in a statistical interpretation of inverted models, see Scheidt et al. (2018).

In general, the most used geophysical method for monitoring in MSW is time-lapse ERT. Yet, also useful information can be derived from noise-based passive seismic methods, which can be deployed relatively easily on a variety of landfill types and infrastructures. It is also possible to use a GPS network to assess the deformation rates in the surface, which in turn could be correlated with biodegradation processes, e.g., Jiang et al. (2020), applied to the study of an underground gas storage facility). In this view, there is potential on the combined use of geochemical/geotechnical and geophysical techniques for mapping and monitoring fluids migration processes (Sciarra et al., 2021; Wagner and Wiese, 2018).

In summary, we reviewed how geophysical methods can be used to deliver insights about the state of a landfill or metallurgical residues, despite the complex bulk geophysical response originated by anthropogenic materials and variations in physical conditions within them. We also illustrated how mainly geoelectrical methods are being used to image in static and dynamic ways the processes related to biodegradation in MSW landfills, for instance, mapping (and monitoring) the accumulation of gas and biogeochemically active zones. Regarding the investigations carried out in metallurgical wastes, geoelectrical methods have also been largely used at field scale. IP in particular has proven suitable to investigate slags while ERT may not always image these deposits. This fact is due to the linear relation that has been observed between the chargeability and the slag (metallic) concentration. The study of the dynamic behavior of these residues, e.g., oxidation-reduction reactions, is complex and has mostly been applied at lab scale where SIP represents a promising method.

In this regard, there is a need to improve both the spatial and temporal resolution of geophysical imaging specially to improve monitoring, which could be achieved through the use of new sensors, combining multiple geophysical methods, deployed from the surface and in boreholes, and when possible, through the (permanent) installation of sensors as part of an engineered landfill infrastructure for long-term monitoring. These advances in technologies and methods can potentially lead to more accurate static and dynamic characterization of landfills, which in turn can improve decision support to evaluate material recovery and other DLM site redevelopment projects.

From the literature presented above, we can conclude that there is a need to develop more quantitative interpretation methodologies that take into account the associated uncertainty for more reliable characterizations of landfills and deposits in particular in the case of volume estimations. Furthermore, more comprehensive characterization of metallurgical residues, in terms of metallic content or mineral variations require integrated methodologies that integrate first, geophysical and geochemical lab measurements and additionally link this lab-calibration with geophysical data at field scale. These were the drivers of the methodologies presented in Chapters 4 and 5.

TABLE 3.1: Applicability of different surface geophysical methods targeting different objectives as well as type of interpretation.

Authors	Type of landfill	Main method	Objective	Type of interpretation	Validation
Audebert et al. (2014)	MSW-industrial waste, engineered landfill	time-lapse ERT	Monitoring- delineate infiltration zones in leachate injection	visual (based on inverted time-lapse models)	EMI mapping
Dumont et al. (2016)	MSW, industrial & inert waste, engineered landfill	ERT	gravimetric water content distribution	Based on petrophysical laws	borehole EM, sampling, lab measurements (T, liquid phase σ, compaction, bulk ρ, etc.)
Konstantaki et al. (2016)	MSW, sludge, industrial waste, semi-engineered bioreactor landfill	P and S-wave reflection imaging	delineate wet and gassy zones	visual (from inverted models), detection of air-filled pockets	MASW, biogas flow and mechanical tip resistance measurements in wells
Cavalcante Fraga et al. (2019)	Urban fill (CDW)	EMI calibrated with ERT	Lateral & vertical delineation of deposit	Depths from 1D EMI inversions	Comparison with 40 trenches (depths: 0.4- 3.6 m)
Martin et al. (2020)	Mine waste dump (silver, lead) & CDW	2D ERT profiles interpolated to 3D	Volume estimation	Volume computed using a ρ threshold estimated from SIP lab measurements	depths comparison with 16 drill cores (depths: 4-8 m)
Flores-Orozco et al. (2020)	MSW, soil, CDM, semi-engineered, with aeration system	ERT & IP	delineation of biogeochemical active zones	visual from inverted models	comparison between leachate TOC measurments from waste samples and inverted models

(*Continuation) Applicability of different surface geophysical methods targeting different objectives as well as type of interpretation.

Authors	Type of landfill	Main method	Objective	Type of interpretation	Validation
Frid et al. (2017)	MSW, semi-engineered landfill (bottom water-proof geotextile)	ERT and IP	leachate detection	based on probability models derived from statistical distribution of inverted data (ratio chargeability/resistivity)	drilling, sample collection and leachate lab measurements(ρ)
Dumont et al. (2017)	MSW, industrial & inert waste, engineered landfill	H/V & MASW	estimate thickness of the waste deposit	Parametric analysis of H/V using inverted model of S-wave velocity, direct thickness estimation	borehole nearby and gravimetry
Magiera et al. (2019)	dump with slags & ashes from glass factory, modern bottom ashes, CDW	Magnetometry, EMI, ERT, 90 punctual surface measurements of κ	delineation of dump geometry	visual (from mapping EMI and Magnetic measurements and profiling ERT inverted models)	Collection of topsoil cores at 27 points, lab measurements (κ)
Sun et al. (2023)	hazardous waste landfill	ERT	leachate delineation	visual, based on deep network for multi-view fusion (3 electrode arrays) to invert ERT data	inverted ERT data from synthetic models & salt trace experiment

Chapter 4

Quantitative interpretation of geoelectric inverted data with a robust probabilistic approach

The non-uniqueness of the solution of the geophysical inverse problem can lead to misinterpretation while characterizing the subsurface. To tackle this situation, ground-truth information from excavations and wells can be used to improve, calibrate and to interpret inverted models. We refer to quantitative interpretation as the decision analysis based on probability theory, which is focused on solving a classification problem. First, we present a probabilistic approach to classify different types of materials or categories observed in borehole logs using multiple data sources: inverted 2D electrical resistivity tomography (ERT) and induced polarization (IP) data, and the positions (x, z) of these boreholes. Then, using Bayes' rule and permanence of ratios, we compute joint conditional probabilities of each category, given all data sources in the whole inverted model domain. We validate this approach with synthetic data modeled for a complex anthropogenic-geologic scenario and using real data from an old landfill. Afterwards, we assess the performance of the probabilistic approach for classification and compare it with the machine learning algorithm of multi-layer perceptron (MLP). Additionally, we analyze the effect that the different data sources and the number of boreholes (and its distribution) have on both approaches with the synthetic case. Our results show that the MLP performance is better for delineating the different categories where the lateral contrasts in the synthetic resistivity model are small. Nevertheless, the classification obtained with the probabilistic approach using the real data seems to provide a more geologically realistic distribution. We conclude that the probabilistic approach is robust for classifying categories when high spatial heterogeneity is expected and when ground-truth data is limited or not sparsely distributed. Finally, this approach can be easily extended

to integrate multiple geophysical methods and does not require the optimization of hyperparameters as for MLP[1].

4.1 Introduction

Geophysical imaging has been widely used to derive insights on the subsurface structures and processes by mapping physical parameters through non-invasive techniques. After processing and interpretation of geophysical measurements this information can be translated into geologic structures, quantification of volumes and geometries, or can be used to provide insight of groundwater processes (Romero-Ruiz et al., 2018; Slater and Binley, 2021; Whiteley et al., 2019). To obtain these images or physical models an inverse problem, which is usually ill-posed and presents a non-unique solution, is solved (Aster et al., 2018). Inverse problems may be solved using prior information in the form of structural or geostatistical constraints in the higher dimensional space of the model parameters (Caterina et al., 2014; Chasseriau and Chouteau, 2003; Kaipio et al., 1999) and more recently in lower dimensional spaces using machine learning methods provided that generative models may be trained to enforce consistent spatial patterns (Lopez-Alvis et al., 2021, 2022). Interpretation of geophysical images can be achieved with several approaches ranging from a qualitative analysis that might be validated by correlation with ground truth data (Magiera et al., 2019; Yannah et al., 2017) to automated quantitative processes to directly assist interpretation when a large amount of data is available, for example using deep learning approaches (Wang et al., 2018) or when the translation from bulk geophysical properties to properties of interest is sufficiently linear, e.g., Hermans et al. (2012). In the following, we focus on the quantitative approaches to improve data interpretation.

In geosciences, there is a recent increase in the use of machine learning, deeply rooted in applied statistics, where computational models are built using inference and pattern recognition (Dramsch, 2020). In this context, supervised and unsupervised learning algorithms of linear and nonlinear methods have also been developed and adapted (Scheidt et al., 2018).

For example, Moghadas and Badorreck (2019) used neural networks to successfully link time-lapse ERT data to soil moisture, collecting reference data via an excavated pit and using the reference electrical conductivity and temperature values as

[1]This chapter is based on: Isunza Manrique, I., Caterina, D., Nguyen, F., and Hermans, T., 2023, Quantitative interpretation of geoelectric inverted data with a robust probabilistic approach: Geophysics, **88**, no. 3, KS73-KS88.

data sources or inputs to train the supervised learning algorithm. To solve a classification problem also using supervised learning, Lysdahl et al. (2022) applied the algorithm of multi-layer perceptron (MLP) to extract the depth to bedrock from airborne electromagnetics and sparse drillings. Training data were pairs of known depth points and resistivity data. The former approach was used in a field case with a post-glacial geomorphology, yet the authors concluded that the geological complexity was the main limitation on the MLP performance.

Combining two or more geophysical methods based on different physical properties can greatly reduce the ambiguities inherent to each method (Hellman et al., 2017), improving the interpretation and geophysics-based characterization. Paasche et al. (2006) adopted a statistical approach to integrate the physical models from individually inverted georadar and seismic data into one multiparameter model, and to estimate the spatial distribution of petrophysical parameters (from limited geophysical and petrophysical databases) using fuzzy c-means clustering. Another example of unsupervised learning to solve a classification problem is given by Whiteley et al. (2021), who used a Gaussian Mixture Model algorithm to classify geophysical data into cluster groups to build a ground model and characterize landslide materials. These authors used three geophysical variables as data sources: resistivity, P-wave and S-wave velocities, and a spatial variable: depth from the ground surface. In the context of landfill investigations, Inauen et al. (2020) applied several algorithms of supervised learning to classify geoelectric and seismic data according to the materials observed in several trial pits and boreholes. The main goal was to derive a model of a solid waste landfill, for which the algorithm of MLP presented a good classification performance.

In the literature, we find fewer applications for the interpretation of geophysical data based on statistics or probability theory exclusively. For example, Dewar and Knight (2020) developed a methodology for estimating the top of the saturation zone from airborne electromagnetic data (1D resistivity models) and measurements from nearby wells. The methodology included the optimization of two parameters: 1) a search radius, to integrate resistivity data within this area, and 2) statistical properties of the resistivity distribution that best captures the transition from unsaturated to saturated zone, i.e., minimum, maximum, difference between minimum and maximum, mean, difference between the 75th and the 25th percentiles and standard deviation.

In most of the cases discussed above, the interpretation of geophysical data provides a single model representing the physical reality in which the uncertainty is often not considered. In this regard, the Bayesian framework has become one of the leading paradigms to quantify uncertainty in geophysical modelling, inversion and

data interpretation, which can be translated into more rigorous decision making in subsurface systems, especially under noisy data (Bobe et al., 2020; Parsekian et al., 2021; Ray et al., 2018; Scheidt et al., 2018). Bayesian analysis or inference refers to all procedures that use Bayes' theorem, where a quantitative relation is introduced to link pre-defined knowledge to new observations, thus comprising the computation of posterior distributions of a set of priors given a likelihood function (Piana Agostinetti and Bodin, 2018). For instance, Wellmann et al. (2018) combined the pre-existing geological modelling with additional geological considerations and gravity data simulations, applying Markov chain Monte-Carlo (McMC) to evaluate and sample from the posterior distributions to obtain suitable geophysical models. This approach successfully addressed uncertainty and optimized the geological model of a sandstone greenstone belt. More recently, Fossum et al. (2022) used Ensemble Randomized Maximum Likelihood (EnRML) to update the subsurface uncertainty in earth models and simulated electromagnetic logs generated with Generative Adversarial Networks (GANs) and a forward deep neural network respectively.

In line with the Bayesian framework, another approach for the interpretation of already inverted geophysical data was used by Hermans and Irving (2017), where the inverted parameters were expressed in terms of categories defined by probability distributions of hydrofacies. The authors assessed the use of ERT to identify and classify hydrofacies in alluvial aquifers, using co-located inverted data and boreholes records, integrating the effect of the sensitivity spatial variation.

In this contribution we use a probabilistic approach as an alternative to perform a rapid quantitative interpretation by classifying geophysical data according to the materials observed in a limited number of co-located borehole logs (hereafter referred as categories or classes). The method is based on the above-mentioned approach used by Hermans and Irving (2017). We extend it to account for more than one geophysical model (i.e., ERT and time-domain IP), and to include spatial trends in the co-located data. For comparison, we also apply the supervised machine learning algorithm of multi-layer perceptron (MLP) and include the same data sources or input for training. We apply both approaches in a synthetic case of study and analyze the effect that the data sources and the number of boreholes (and its distribution) have on the probabilistic approach and MLP. Finally, we compare and validate the approaches using the geophysical data acquired in an old landfill with available co-located trial pits. Such systems are notably difficult to characterize both with geophysics due to the strong heterogeneity and physical contrasts encountered, and with boreholes due to the increased contamination risks. We observed that the probabilistic approach is suitable to classify inverted models that are highly variable along the

whole domain, with predictions consistent with the prior sampling information and the integration of the prediction uncertainty. Note that a robust characterization is crucial in decision-making for a sustainable management, e.g., estimate the internal structure of a landfill to assess potential for resource recovery, to prevent or evaluate associated environmental pollution and prioritize (re)development scenarios (Jones et al., 2018; Van De Vijver et al., 2020, 2021). Below, we first present the methods used for the classification after inversion, the results are then presented for the synthetic case and the field data, followed by discussions and conclusions.

4.2 Methods of classification: probabilistic approach and MLP

4.2.1 Input data

To compare the probabilistic approach and MLP we used the same input or training data. These are the co-located inverted resistivity ρ, chargeability C, the position (x, z) of the boreholes and target categories. In these data a relative cumulative sensitivity threshold is used to keep only parts of the tomograms (ρ and C) that are sufficiently well covered, e.g, Beaujean et al. (2014). Consequently, this also contributes keeping reliable training data and reduce misclassification in the final model (Hermans and Irving, 2017).

4.2.2 Probabilistic approach

In the classification of the probabilistic approach, we first use the training data to define individual probability distributions and then we compute the joint conditional probabilities of each category, given ρ, C, x and z in the whole domain of the inverted models. The results are given in terms of probability maps to belong to each predefined category which can be translated into classes. In the following sections we first introduce the permanence of ratios, which is an alternative to compute joint conditional probabilities of different sources in presence of data interdependence (Journel, 2002). Then, we describe the procedure of the probabilistic approach where the permanence of ratios is used.

Principle of permanence of ratios

Let A be an unknown event that can be assessed with two data events from different sources, B and D, through its conditional probability $P(A|B, D)$. For instance, A may represent a category, such as inert waste, and the events B and D, the resistivity

and chargeability. The easiest way to recombine these probabilities is to assume independence of the data events in which case the joint probability is the product of the marginal probabilities. However, this is a strong hypothesis as B and D are related to the common event A. To take this into account, Journel (2002) proposes an alternative to combine probabilities of different sources based on the permanence of updating ratios while guaranteeing all limit conditions (e.g., $P(A|B,D) \in [0,1]$) even in presence of complex data interdependence. The principle of permanence of ratios indicates that the rates or ratios of increments are typically more stable than increment themselves. For simplicity, let us consider only two data events from different sources B and D, then the logistic-type ratio of marginal probability of the unknown event A is:

$$a = \frac{1 - P(A)}{P(A)} = \frac{P(\tilde{A})}{P(A)} \in [0, \infty] \tag{4.1}$$

where $\tilde{A}$ is the complement of A. And similarly,

$$b = \frac{1 - P(A|B)}{P(A|B)} = \frac{P(\tilde{A}|B)}{P(A|B)} \qquad d = \frac{1 - P(A|D)}{P(A|D)}$$
$$X = \frac{1 - P(A|B,D)}{P(A|B,D)} = \frac{P(\tilde{A}|B,D)}{P(A|B,D)} \geq 0 \tag{4.2}$$

Then the ratio a can be seen as a measure of prior uncertainty about A, $a = 0$ if A is certain to occur and $a = \infty$ if A is an impossible event. Similarly, d can be seen as the distance to A occurring after observing the data event D. The ratio d/a is then the contribution of D to that distance starting from the prior distance a. Finally, X would be the distance to A occurring after observing both events B and D, and the ratio X/b is the incremental contribution of D starting from the distance b. The permanence of ratio assumes

$$\frac{X}{b} \simeq \frac{d}{a} \tag{4.3}$$

which means that the incremental contribution of data event D to knowledge of A is the same after or before knowing B. Then, the joint conditional probability of the two events B and D can be expressed as $P(A|B,D) = \frac{1}{1+X} = \frac{a}{a+bd}$.

We can generalize the previous expression to n data events G_i, $i = 1, ..., n$. Denoting by $|G_i, i = 1, ..., n$ the joint conditioning to all n data events, the conditional

probability provided by a succession of $(n-1)$ permanence of ratios is:

$$P(A|G_i, i = 1, ..., n) = \frac{1}{1+X} \in [0, 1] \tag{4.4}$$

with

$$X = \frac{\prod_{i=1}^{n} g_i}{a^{n-1}} \geq 0 \iff Ln(X) - Ln(a) = \sum_{i=1}^{n} [Ln(g_i) - Ln(a)]$$
$$a = \frac{1 - P(A)}{P(A)}, \qquad g_i = \frac{1 - P(A|G_i)}{P(A|G_i)}, \qquad i = 1, ...n$$

Which is an expression that verifies all limit properties, and it only requires the knowledge of the prior probability $P(A)$ and the n elementary single data event-conditioned probabilities, $P(A|G_i)$ which can be evaluated independently one from another using co-located data.

Procedure of the probabilistic approach

Let A_i be the different categories (materials) found in the boreholes along the inverted sections. First, we estimate a prior probability or material proportion $P(A_i)$ based on the area they occupy in the boreholes co-located in the 2D inverted sections. Then, we determine unimodal distributions of the training data given each category A_i, i.e., $f(\rho|A_i)$, $f(C|A_i)$, $f(x|A_i)$, $f(z|A_i)$. These distributions define parameters, i.e., shape, locations and scales, which we use afterwards to estimate the distributions in an extended dataset: ρ, C, x and z in the whole inverted model domain. In the next step, we compute the conditional probability of each material using Bayes' rule. For instance, to compute the conditional probability of a category A_i, given the resistivity, we use:

$$P(A_i|\rho) = \frac{f(\rho|A_i)P(A_i)}{\sum f(\rho|A_i)P(A_i)} \tag{4.5}$$

and similarly, for the conditional probability of A_i given C, x or z.

At this stage we need to combine the prior probabilities $P(A_i)$ with the conditional probabilities of A_i given the datasets, into the joint conditional probabilities $P(A_i|\rho, C, x, z)$. To this aim we use Equation 4.4 where the event A becomes the categories A_i, $n = 4$ and the data events G_i are ρ, C, x and z. Therefore the ratios $g_i = \frac{1-P(A|G_i)}{P(A|G_i)}$ will be given in terms of the marginal probabilities $P(A_i|\rho)$,

$P(A_i|C)$, $P(A_i|x)$, $P(A_i|z)$ for each category. The joint conditional probabilities are then normalized (divided by $\sum_i P(A_i|\rho, C, x, z)$) to ensure the closure condition, i.e., $P(A|(\cdot)) + P(\tilde{A}|(\cdot)) = 1$. Then, the results are given in terms of probability maps for each category in the whole inverted model domain, and therefore may be used to assess the interpretation uncertainty. Finally, we may also derive a map in terms of the categories by comparing the normalized joint conditional probabilities of A_i and selecting the category corresponding to the largest probability value, i.e., classification model.

4.2.3 Supervised machine learning: MLP

Classification and regression methods are part of statistical learning and machine learning for which numerous methods have been developed, from simple linear regression to nonlinear methods such as neural network or deep learning (Scheidt et al., 2018). Here, we focus on the multi-class classification problem, where we want to predict discrete class labels or categories for unlabeled patterns based on observations. We used the algorithm of multi-layer perceptron (MLP) or feedforward neural network, which proved to have a good performance for classification in the context of landfill investigations (Inauen et al., 2020).

Description of MLP

As explained by Goodfellow et al. (2016), the goal of MLP is to approximate some function f^*. For a classifier, the function $A_i = f^*(\{\cdot\})$ maps an input data $\{\cdot\}$ to a category A_i. This algorithm defines a mapping $A_i = f(\{\cdot\}, \theta)$ and learns the value of the parameters θ (weight and bias coefficients of the transformation function), that result in the best approximation. MLP or feedforward neural networks are models where the information flows through the function from the input data, through the intermediate computations (linear and non-linear data transformations followed by an activation function) used to define f and finally to the output A_i. They are networks because they can be composed of many different functions connected in a chain, i.e., $f(\{\cdot\}) = f^{(3)}(f^{(2)}(f^{(1)}(\{\cdot\})))$, where the superscript 1 refers to the first layer of the network, 2 for the second layer and the final layer is called the output layer. The overall length of the chain gives the depth of the model, the more layers the 'deeper' the model. In this contribution we are dealing with a small amount of geophysical data, thus as shown in the next sections, a simple neural network (few layers in the chain) proves to be enough.

The neural network makes use of training data to drive $f(\{\cdot\})$ to match f^*. These data provide approximations of f^* evaluated at different training points, which are

accompanied by a category (A_i). Then the learning algorithm decides how to use the other layers to produce the desired output, and as we cannot see the intermediate output of each of these layers, they are referred as hidden layers. Finally, each hidden layer of the network is composed of several units or neurons that can act in parallel, representing a vector-to-scalar function.

In the multi-class classification, the output layer receives the values from the last hidden layer and transform them into the different classes, commonly with the Softmax function. This activation function of the last layer normalizes the data and transform them into an output probability vector, based on which the output classes are selected, e.g., Williams and Barber (1998). Therefore, the output is quite similar to the probabilistic approach.

MLP architecture

To design and optimize the architecture of MLP in terms of the hyperparameters (such as number of hidden layers, neurons, or regularization), the total training data are divided in a validation dataset (10-20 %) and a remaining training dataset (70-80 %). The partition is done randomly but preserving the relative frequency of the categories.

To tune the hyperparameters we trained the MLP algorithm using combinations of different numbers of hidden layers (from 1 to 10), number of neurons (1-100), solver for weight optimization and activation function for the hidden layers, computing the accuracy score or the fraction of correct predictions in the validation dataset. Then we select three MLP architectures from which the highest scores were obtained, and compare them with the accuracy scores of the prediction in the training dataset for several regularization values. We select the regularization parameter where the gap between the accuracies (from validation and training) is reduced while still preserving a relatively large accuracy score, i.e., generalization. In addition, as we have a multiple-classes problem, we first applied one-hot encoding to define each class (Fu et al., 2019; Liu et al., 2021; Potdar et al., 2017). This simply means we encoded the categories as a binary (one-hot) numeric array. Once the hyperparameters are selected and the architecture of the algorithm is defined, the training data set is the same as the one used for the probabilistic approach (or validation plus training data as indicated here).

4.2.4 Classification performance assessment

For both methods, we evaluate the performance of the classification or prediction of classes using a test dataset. In the synthetic case, these are the categories known at the whole model space (excluding the data at the boreholes) and in the field case, a percentage of the training data where the categories are known. Then, we compute two classification scores to compare the results of this classification or "prediction" with the original categories of the test dataset. First we use the accuracy score, which computes the fraction of correct predictions. Given a predicted class $\hat{A}_i$ for a sample i, the accuracy score can be expressed as

$$accuracy(A, \hat{A}) = \frac{1}{n} \sum_{i=0}^{n-1} 1(\hat{A}_i = A_i) \tag{4.6}$$

where A_i is the true category, n is the number of samples and $1(x)$ is the indicator function, which maps the elements of a subset to one and the rest of elements to zero (Pedregosa et al., 2011). We selected this accuracy score as we want to assess the classification performance of both methods when considering a model with a predominant material or class. Additionally, we used the confusion matrix to assess the performance of the classification. In this matrix, the elements on the diagonal are the percentage of categories that are correctly predicted, and the off-diagonal elements are the misclassified percentage. In the synthetic and field case examples, the categories for the classification are: non-organic waste deposits, soil, lime, backfill and limestone bedrock.

4.3 Results

4.3.1 Synthetic case study

Model generation and inversion

The synthetic model is inspired by a real near-surface scenario composed of anthropogenic materials deposited on a limestone quarry. The data were simulated for a resistivity and chargeability distributions composed of five regions derived from non-organic waste deposits, soil, lime and backfill on a limestone quarry (Figure 4.1). In this geometry we defined a surficial and continuous layer of waste, as this material was observed in the ground surface in the real landfill. We included two types of backfills: neutral soil and crushed limestone (here referred as backfill) to investigate if these materials were discriminated using ERT and IP data. Then we defined two

bodies of lime at different positions (x, z) and with different thicknesses, to test the effect that including spatial trends has on the classification approaches. Lastly, the upper limit of the bedrock has a step-like shape, which might be close to a limestone quarry structure. The resistivity and chargeability values we used for the different regions are shown in Table 4.1. Then, similar to the field measurements, we created a dipole-dipole acquisition scheme with 64 electrodes spaced 1.5 m. For the numerical modelling of ERT and time-domain IP datasets we used the open-source library pyBERT, which is based on the framework of pyGIMLI (Rücker et al., 2017).

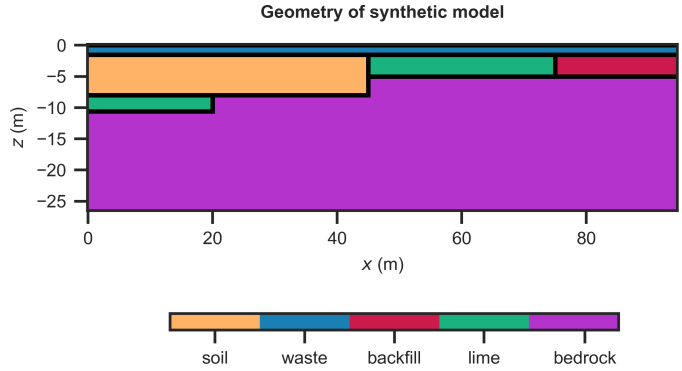

FIGURE 4.1: Geometry for the ERT and time-domain IP modeling.

TABLE 4.1: Resistivity and chargeability values for the different regions used for modeling.

Region marker	Material	ρ (Ω m)	C (mV/V)
1	Soil	300 (Wang et al., 2017)	15 (Kiberu, 2002)
2	Limestone	9000 (Sun et al., 2017)	10 (Johansson et al., 2017)
3	Backfill	800 (crushed limestone backfill, e.g., Qiao et al. (2019))	15 (RAWFILL, 2020)
4	Heterogeneous waste (nonorganic)	500 (Dumont et al., 2017)	100 (Elis et al., 2016)
5	Lime	3 (sample measured in the lab, this study)	1.3 (see Moreira et al. (2019) for chargeability values in dolomitic deposits, as raw material for lime production)

The ERT data were modeled adding a 3% voltage dependent noise plus 1μV absolute error, e.g., Costall et al. (2020). Then, the apparent chargeability was modeled following Seigel's formulation, carrying out two DC resistivity forward models: the

inverted resistivity of the medium and a decreased resistivity modified by the intrinsic chargeability (chargeability model, Table 4.1) (Oldenburg and Li, 1994; Seigel, 1959).

Finally, the synthetic data were inverted using the commercial software RES2DINV (Loke, 1997, 2004) to avoid the pitfall of using the same forward solver in the reconstruction algorithm (Lionheart, 2004). Here, we incorporated the data noise estimate for the apparent resistivity by subtracting the synthetic data modelled with and without added noise. We used a robust least-square inversion with the Gauss-Newton method and an initial damping factor of 0.25. The inverted ERT and TDIP models are displayed in Figure 4.2 together with the normalized sensitivity represented in logarithmic scale and the real interfaces from Figure 4.1.

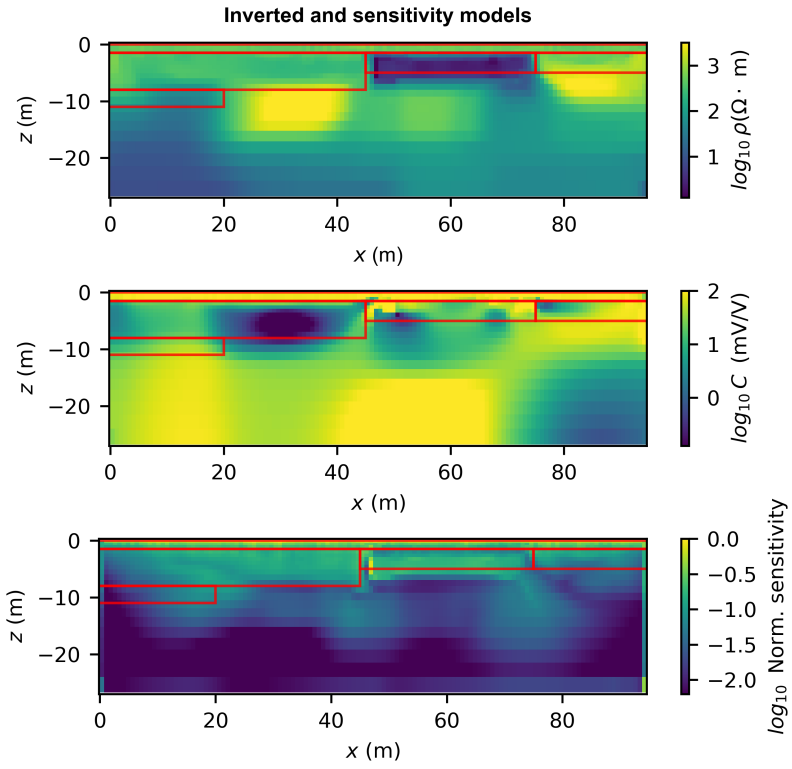

FIGURE 4.2: (a) Inverted resistivity and (b) chargeability models with the (c) associated normalized sensitivity. The rms errors of the inversion were 4.57% and 6.72%, respectively. Red boundaries represent the real model from Figure 4.1.

In the resistivity model, low values delineate the shallower lime deposit, but the deeper lime cannot be imaged. There is no clear contrast of resistivity between the heterogeneous waste and the soil and backfill underneath. The upper limit of the bedrock is better imaged from x $\approx$ 20 m to the end of the profile. Nevertheless, the resistivity values of the bedrock have a strong lateral variation as an effect of the

regularization (there was a tradeoff between the damping factor and the rms error) and low sensitivity.

In the chargeability model, the surficial layer of waste is well delineated with large values. Nevertheless, the horizontal interface of the backfill/soil and the lime cannot be clearly distinguished. Artifacts of large chargeability are present at the locations of the lime and larger artifacts in the bedrock area centered at x $\approx$ 10 and 30 m.

For the assessment of the inverted models' reliability, we used the normalized sensitivity in logarithmic scale (hereafter referred as sensitivity), which shows how the data are influenced by the respective resistivity of the model cells. In Figure 4.2 we can observe a general sensitivity decrease with depth, particularly below the shallowest lime deposit.

In addition, we also present the cross-plots of the inverted resistivity (ρ) and chargeability (C) values (Figure 4.3). For comparison we also plot the mean of the inverted data $\mu_i = (\rho_\mu, C_\mu)$ together with the initial values for modelling (Table 4.1) for each category. First, we can notice that the mean of the inverted data for the bedrock, presents a largely underestimated value of resistivity compared to the initial value. The second category where we can see a large variation is the lime, where the mean of the inverted resistivity was larger than the initial modeling values. Additionally, notice that all the clusters' categories are largely overlapping, especially the bedrock and lime, whose ρ and C values are widely distributed. This gives an insight on the ability of ERT and IP for resolving the features of this complex anthropogenic scenario and on the uncertainty associated within the inversion process.

Synthetic borehole sampling

In this synthetic case we assume a sampling scenario composed of several equidistant boreholes along the inverted 2D section. Notice that in real study cases, we want to reduce the number of excavations to mitigate costs, and environmental and health risks. Then to select and justify an optimum number of boreholes we follow a statistic analysis. We used the mean of the inverted data for each class i, (see Figure 4.3, represented with triangles), and computed the mean of the inverted data within a variable number of boreholes b. For each class i, this was represented as $\mu_i(b)$. Then, we compute a summation of the difference between μ_i and $\mu_i(b)$ over all the classes i, i.e., $\sum_i(\mu_i - \mu_i(b))$. Figure 4.4 shows the plot of the summation vs the number of boreholes b. As b increases (and tends to cover the entire domain) the summation is closer to 0 as $\mu_i(b) \rightarrow \mu_i$. The first points of this plot vary depending on the location of the selected boreholes and for $b < 6$, the summation's rate decreases more significantly. Therefore, in the following sections we start by using

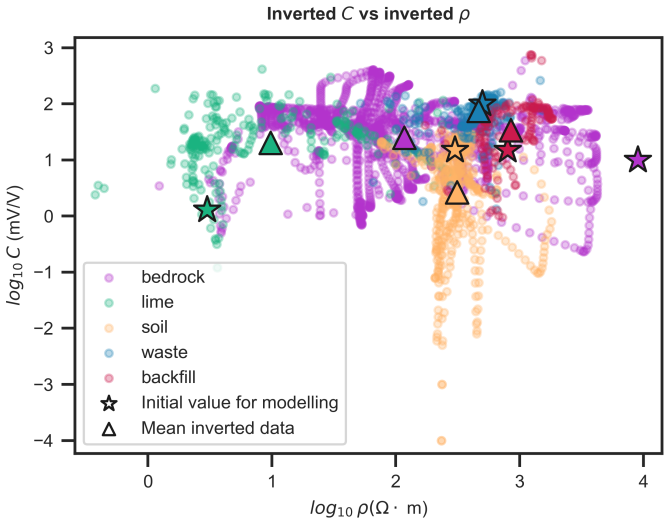

FIGURE 4.3: Crossplot of the inverted chargeability versus the inverted resistivity in logarithmic scale. The stars represent the original values for modeling, and the triangles represent the mean of the inverted data for each category, i.e., $\mu_i = (\rho_\mu, C_\mu)$. The inverted data corresponding to the different categories are represented with different colors.

5 boreholes equidistantly distributed (Figure 4.5) and test the effect of changing b in the probabilistic approach and the MLP model.

Interpretation – Classes prediction using probabilistic approach

The training data were composed of $\{\rho, C, x, z\}$ at the borehole locations, which resulted in a matrix of 158×4, and their respective known categories (vector of 158×1). In this case we used a sensitivity threshold of $10^{-1.7}$ to keep only parts of the tomograms that are sufficiently reliable. The threshold was chosen based on the maxima of the sensitivity gradient, taking the average sensitivity values located beneath the area of the shallowest local maxima (below the conductive zone corresponding to the lime deposit). This threshold leads to use 38 % of the grid cells, which supports the assumption of testing this approach on heterogeneous models (few reliable data).

For each category observed in the boreholes logs, A_i =soil, waste, backfill, lime and bedrock, we estimate a prior probability $P(A_i)$ based on the area that they occupy on the boreholes (see Figure 4.5). The proportions are respectively 9.57%, 5.5%, 2.5%, 7.3% and 74.9 %. Note that if the boreholes are limited in depth, one would naturally assume the vertical continuity of the bedrock once encountered. Then, we computed unimodal Gaussian distributions of the training data given each category A_i, and computed the corresponding conditional probabilities according to Equation **??**. We selected this type of distribution as they can integrate the overall uncertainty

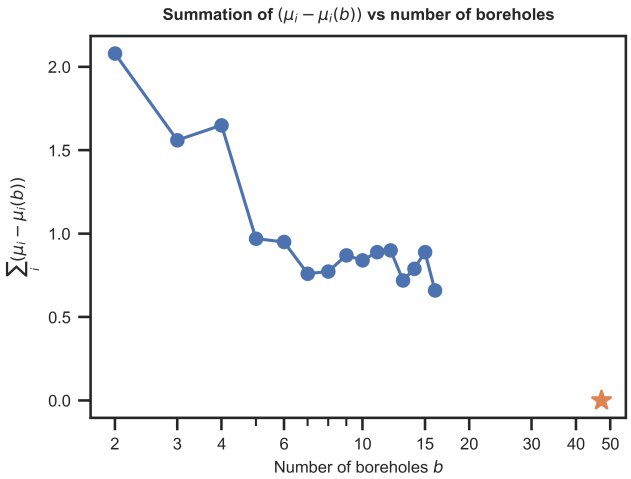

FIGURE 4.4: Summation of the difference between μ_i and $\mu_i(b)$ over all the classes versus the number of boreholes. Notice that initially $b = 2$ as we need to have all the category types.

from data noise, inversion artifacts and scarcity of the co-located data. If a lot of co-located data are available, empirical distribution can be built without requiring any assumption about their shape. Figure 4.6 shows the conditional probabilities with and without considering the sensitivity threshold.

The distributions of Figure 4.6 show the impact of the large prior probability considered for the bedrock. This category presents the largest probability values for $log_{10}\rho > 0.5$, for $log_{10}C > 0$, at the largest depths $z < -6$ and nearly along the whole model domain in x. Yet, it can be observed that the resistivity model was able to discriminate between the bedrock and the lime. With the chargeability model, we can only discriminate the soil from the bedrock, due to the heterogeneities of large values distributed in the bedrock. This is the reason why it was not possible to clearly distinguish the waste (material with the largest chargeability modelling values) from the other categories.

The conditional probabilities given the spatial coordinates show a trend on the vertical (z) and lateral (x) distribution of the materials according to the location of the boreholes, i.e., the probabilities are impacted by the spatial distribution and number of boreholes. Given the depths, several categories are clearly resolved: bedrock at the largest depths, soil at intermediate depths and waste at the shallowest zone. However, these distributions cannot discriminate between different categories at similar depths. In the distributions given the distance x, we can roughly differentiate between the soil (maximum probability at shorter x) and the backfill with larger probabilities at the end of the profile. Note the impact that the small sampled region of backfill has on its conditional probability (large probabilities in a in a reduced range of x).

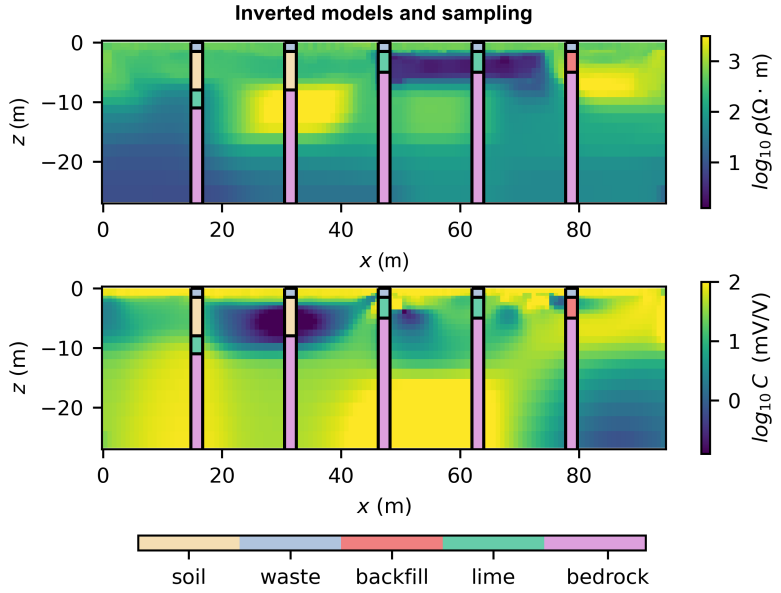

FIGURE 4.5: Resistivity and chargeability inverted models plotted with the boreholes. Where bedrock is present, we assume it reached the bottom of the models.

Afterwards, we computed the joint conditional probabilities for each category $P(A_i|\rho, C, x, z)$ using Eq. 4.4 and normalized them so that they sum to one. Hereafter we refer to the normalized joint conditional probability simply as joint probability. We work with the ratios of each data event, $g_i = \frac{1-P(A|G_i)}{P(A|G_i)}$ whose corresponding conditional probability can be independently estimated, i.e., $P(A_i|\rho)$, $P(A_i|C)$, $P(A_i|x)$ and $P(A_i|z)$. The results are presented as probability maps, see for instance Figure 4.7, where the joint probabilities of the waste and the bedrock are represented in the whole model domain. The surficial layer of waste was accurately delineated whereas the upper limit of the bedrock was overestimated in the beginning of the profile $x < 20$ m.

We derived a map in terms of the categories by comparing the joint probabilities of the materials and selecting the category corresponding to the largest probability value (Fig. 4.8). In this map we added transparency which indicates the decrease of probability values: total opacity represents a probability of 1 and the strongest transparency represents a minimum probability of 0.25 for four categories. Finally, we computed the classification scores comparing the results with the test data, i.e., categories of the synthetic model (excluding the data at the boreholes). We obtained an accuracy score of 0.87 and the confusion matrix is shown in Fig. 4.8.

First, we can notice that the bedrock could be predicted along the entire model and especially in the deeper areas, although its occurrence was slightly overestimated.

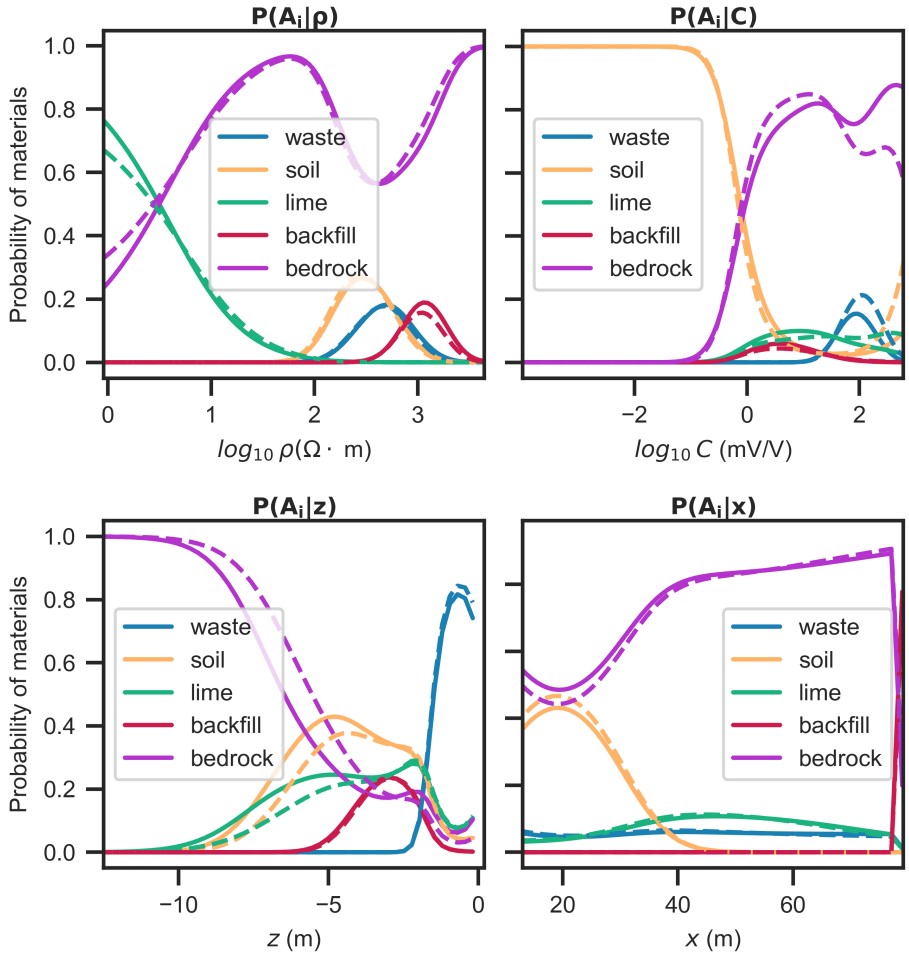

FIGURE 4.6: The conditional probability of A_i given (a and b) ρ and C, respectively, and (c and d) z and x from the boreholes. The solid lines represent the probabilities derived using the whole data within the boreholes and the dashed lines represent the distributions using a sensitivity threshold.

The waste deposit could be accurately delineated, whereas the soil and the lime deposit in the central part of the profile were roughly delimitated laterally and vertically. This is represented in the confusion matrix, as we found that the bedrock obtained the largest number of correct predictions followed by the categories of waste, soil and lime. The backfill could only be predicted in the area immediately around the borehole. This is mostly an effect of integrating the horizontal tendency x of the boreholes in the joint probabilities and this is the reason why in the confusion matrix, the lowest percentage of correct classifications correspond to backfill. The largest percentage of incorrect predicted categories corresponded to the backfill which were misclassified as bedrock.

The second lime body, close to the origin of the profile could not be detected, first because the inverted geophysical models could not resolve this feature and secondly,

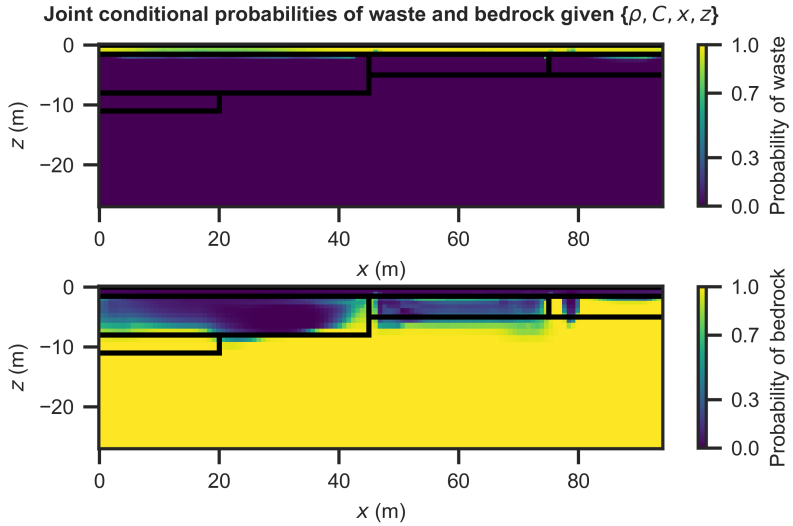

FIGURE 4.7: Joint probabilities of (a) the waste $P(A_{waste}|\rho, C, x, z)$ and (b) the bedrock, using a sensitivity threshold of -1.7.

because this category has considerably lower prior probability values compared to the bedrock. This is the reason why this zone was predicted as bedrock.

The transparency added in Figure 4.8 allows to identify the zones where there is a larger uncertainty in defining the categories, e.g., the lateral interface between the soil and the lime.

Interpretation – Classes prediction using MLP

We apply the MLP algorithm using the python library of scikit-learn (Pedregosa et al., 2011). The training data were composed of $\{\rho, C, x, z\}$ at the borehole locations, resulting in a matrix of 158×4, and their respective known categories (vector of 158×1). Similar to the probabilistic approach, we consider a sensitivity threshold of 10-1.7 on the selected training data. To optimize the architecture of MLP we use a validation dataset which is composed of 15 % of the total training data and the remaining 85 % of data are used to train the algorithm. Several combinations of hyperparameters showed equally large accuracy scores. From the hyperparameters that showed the highest scores, we selected the simplest, two hidden layers of 100 neurons each, a regularization parameter of 0.15, a stochastic gradient-based optimizer and the rectified linear unit as activation function of the hidden layers.

At this step, we used the training data and the validation data to train the algorithm, i.e., the same input data as for the probabilistic approach. The category predictions in the whole model domain are shown in Figure 4.8, where we also added transparency which represents the probability values from the activation function of the output layer (Softmax). Total opacity represents a probability of 1 while total

transparency represents a probability of 0. In Figure 4.8 we can see that the waste, the soil, one lime deposit and the backfill were well delineated. The lime body located at the origin of the profile was partially imaged. To assess the performance of this algorithm, we also used the real model defined in Fig. 4.1 as the test dataset (excluding the data on the boreholes) and obtained an accuracy score of 0.95. Figure 4.8 shows the confusion matrix, where the largest number of correct predictions are the ones from the waste, bedrock and soil. The category that was incorrectly classified the most, was the lime (predicted as bedrock). Yet, we can observe that the classification of the lime and backfill improved using MLP.

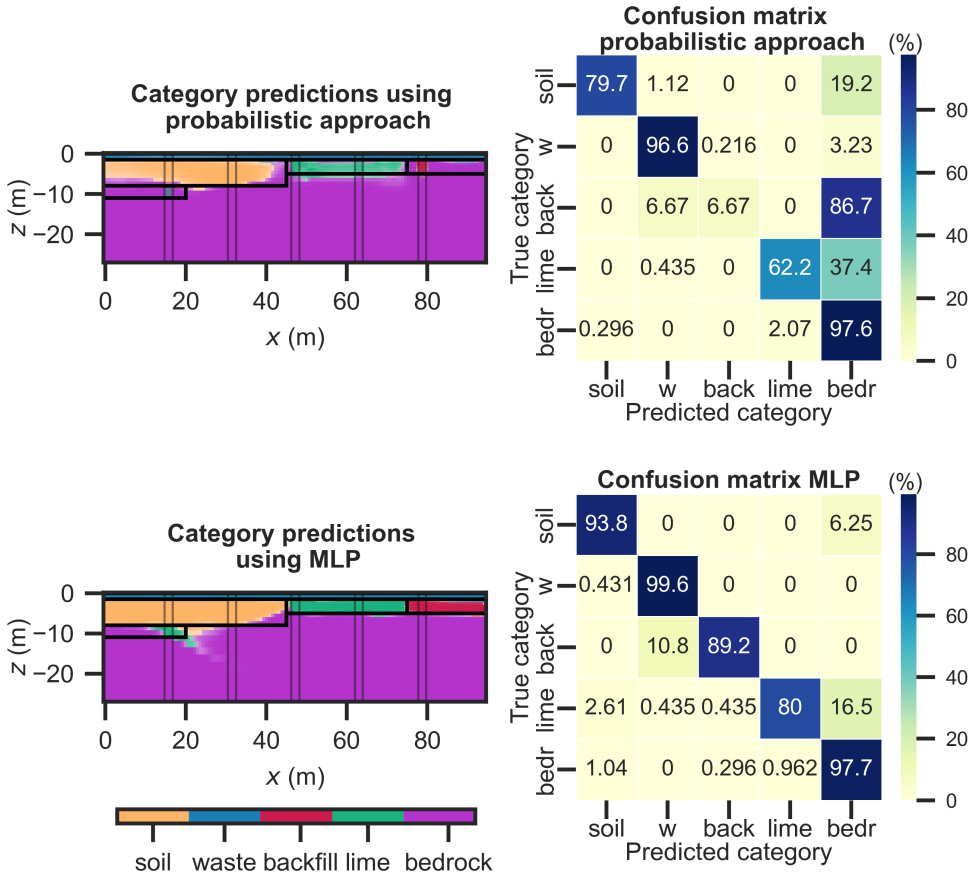

FIGURE 4.8: Category predictions from the (a) probabilistic approach and (b) MLP with borehole locations and corresponding confusion matrices. Minimum probability values (higher transparencies) are 38% for the probabilistic approach and 43% for MLP. In the confusion matrices, "w" refers to waste, "bedr" refers to bedrock, and "back" refers to backfill.

Effect of data sources as input

In this section we show the effect the data sources or elements of the training data have on the probabilistic approach and MLP. Figures 4.9 to 4.11 show the category

predictions of both methods and the respective confusion matrix when we use only the resistivity inverted data, ρ co-located with the boreholes, the resistivity together with the chargeability inverted data, ρ and C, and these two inverted datasets together with the depth z.

First, we can notice that when we only use ρ or ρ and C (with a sensitivity threshold of $10^{-1.7}$) as training data in MLP, the predictions are strongly influenced by the artefacts from the model inversion leading to several misclassified zones (see Figs. 4.9 and 4.10). Some categories remain correctly identified such as the waste deposit and part of the soil. On the other hand, the probabilistic approach overestimates the distribution of the bedrock (largest prior probability). It partially distinguishes one lime deposit when using only ρ, and delineates most of the waste layer and partially the soil when using ρ and C (Figs. 4.9 and 4.10). Although the probabilistic approach is not able to predict all the categories in the whole domain, the results are still in line with the material proportions estimated from sampling and thus more realistic. This is not the case for MLP, where the waste, soil, backfill and lime are predicted at larger depths.

When we use additionally the depth from the co-located boreholes (i.e., ρ, C, z) the results of both methods largely improve (see Fig. 4.11), and the categories are well delineated overall. Yet, the probabilistic approach indicates a larger uncertainty (more transparency) in the deposits of backfill and partially the soil. In addition, the classifications of both methods present few locations where the soil and backfill are misclassified. This is the improvement that we can observe when we use all the data sets: ρ, C, z and x, especially for MLP where the soil is only predicted at $x < 50$ m and the backfill only for $x > 75$ m (see Fig. 4.8).

The probabilistic approach presents some changes when using $\{\rho, C, z\}$ and $\{\rho, C, z, x\}$. The method proves better to classify the backfill deposit when using only $\{\rho, C, z\}$ (accuracy score of 0.89). However, when x is included, the probabilistic approach is strongly impacted and even though it reduces misclassification between soil and backfill at few locations, the backfill is only resolved roughly in the area of a borehole and the accuracy score is reduced to 0.87.

In general, including spatial information on the training data should be done carefully. In the probabilistic approach, the conditional probabilities are clearly impacted by the spatial distribution of the boreholes. Therefore, highly localized sampling of certain materials may lead to small classification zones in the immediate vicinity of a borehole. Although MLP presents large accuracy scores using the spatial training data, which indicates that the distribution of the boreholes reflected the real material distribution of the synthetic case, this is rarely the case in the field (Baasch et al.,

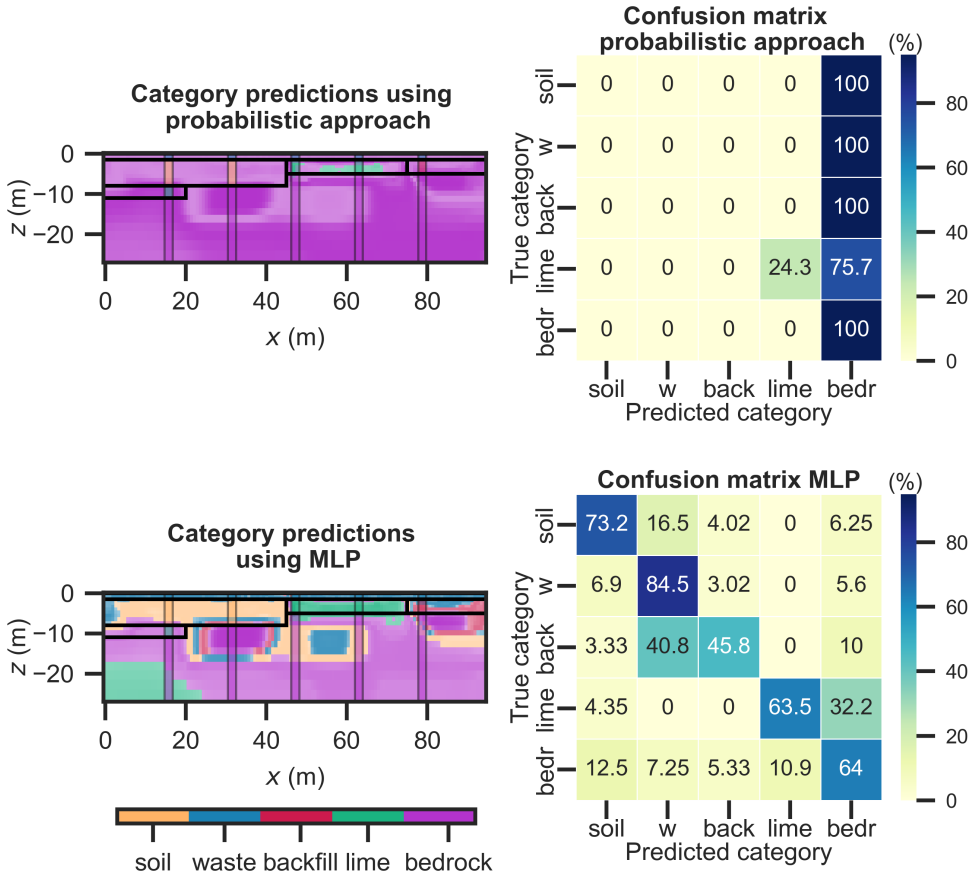

FIGURE 4.9: Category predictions of (a) probabilistic approach and (b) MLP algorithm using only ρ. The minimum probability values are 50% for the probabilistic approach and 40% for MLP, and the accuracy scores were 0.53 and 0.68, respectively. The confusion matrices also are displayed next to each model. The MLP model was built using two hidden layers with 100 neurons each, a regularization parameter of one, the rectified linear unit as an activation function of the hidden layers, and an optimizer based on the quasi-Newton method. In the confusion matrices, "w" refers to waste, "bedr" refers to bedrock, and back refers to backfill.

2018; Cracknell and Reading, 2014; Gahegan, 2000). In particular, in heterogeneous landfills where abrupt vertical and lateral variations of materials may be present.

Effect of borehole sampling

In this section we assess the effect that the number of available boreholes and their distribution have on both methods. We use the training dataset $\{\rho, C, z\}$, which led to a larger accuracy score in the probabilistic approach as compared to $\{\rho, C, z,x\}$. First, we assume a sampling survey with boreholes uniformly distributed along the whole domain (e.g., Fig. 4.5). Secondly, we assume a survey composed of boreholes whose distribution does not map all the model domain, both in x and z directions,

i.e., boreholes might be concentrated in an area of the model and/or boreholes might not go deep enough to map the bedrock upper interface (see Fig. 4.12).

Figure 4.13 shows the plot of the accuracy score against the number of boreholes for both sampling scenarios. Despite that the minimum number of boreholes to capture all categories is 2, this number leads to a highly variable accuracy depending on the distribution of the boreholes. Yet, this variability is largely reduced when $b > 3$. In Figure 4.13 we can note that the accuracy scores of the probabilistic approach using the uniform or non-uniform sampling scenarios are very similar. On the other hand, MLP predicts correctly the classes at most locations of the model under the uniform borehole distribution. Nevertheless, if the boreholes do not cover the whole domain in x and z and therefore, the training samples do not reflect the real distribution of the materials (preferential sampling), the classification performance decreases. In addition, we observed that MLP can lead to unrealistic classifications that underestimate the bedrock distribution even if the accuracy scores are similar to the ones of the probabilistic approach. See for example Figure 4.14, where we show the comparison between both approaches using 3 boreholes of a non-uniform sampling scenario (shown in Fig. 4.12). Note that the lime deposit was predicted at the deepest regions of the model.

4.3.2 Field case study: Onoz landfill

Site description

The study site is in a former limestone quarry in Onoz (Walloon Region, Belgium) that produced lime until 1967. At the end of the quarry activities, the eastern part of the site was filled with slaked lime and fly ash. The area of interest here is the central part of the site, which was used as a landfill where different types of waste were deposited: inert waste, household, industrial waste, backfill, etc. (see Figure 4.15).

Since the landfill closure, several sampling surveys mostly composed of trial pits and different geophysical measurements have been carried out. Here, we focus on one high-resolution 2D profile which has both ERT and IP data (profile P2) and presents the largest number of co-located excavations where bedrock was reported. Profile P3 has only ERT data and both profiles P1 and P3 present a very similar distribution of resistivity and chargeability (Caterina et al., 2019).

Data acquisition and inversion

ERT and IP measurements were collected with an ABEM Terrameter LS. The profile presented here, was acquired using 64 electrodes at 1.5 m electrode spacing. We used a dipole-dipole array configuration and a stack of $n = 2$ and a protocol sorted to limit electrode polarization. For the IP measurements, the electrical current was injected for 2 s, using an integration window of 1.7 s for the electrical resistance measurements, and the decay of electrical potential after current shut off was measured for 3 s.

Data were first filtered by removing the resistance measurements that presented variations larger than 5 % from the measurements repeated two times. This is commonly referred as repetition error, e.g., Robert et al. (2011). On the IP data, the curves of inconsistent decay were also removed, they represented 18 % of the original datapoints. Inversion of data was performed with RES2DINV (Loke, 1997, 2004). We also used a robust least-square inversion with the Gauss-Newton method and an initial damping factor of 0.25. The inverted ERT and IP models are displayed in Figure 16 together with the normalized relative sensitivity. We obtained a RMS of 4.74 % and 3.36 % for the resistivity and chargeability models respectively after 7 iterations.

The inverted resistivity section shows a conductive body on the top of a resistive horizon and a strong lateral contrast at around $x = 30$ m (Fig. 4.16). The IP model presents scattered bodies of large chargeability in the surface and a smoother lateral contrast beneath. Similar to the synthetic model, the sensitivity of these inverted data presents a vertical decrease in the central part, below the conductive body.

Sampling

Several trial pits have been excavated in the landfill's area (Figure 4.15). To test both the probabilistic approach and the MLP algorithm, we consider the 6 trial pits that are co-located with the ERT/IP profile, and which do not cover the entire model domain. Only two shallow pits, not reaching the bedrock, are in the first half of the profile. We assume that once the bedrock is reached, it extends further at depth (in z), see Figure 4.17.

Interpretation – Classes prediction using probabilistic approach

As observed in the synthetic case, the training dataset $\{\rho, C, z\}$ led to a larger accuracy score in the probabilistic approach and MLP. Therefore, here we interpreted the inverted models using as input data the values of $\{\rho, C, z\}$ co-located with the boreholes and ignore the variable x. This defines to a matrix of 149×3 and corresponding

vector of categories of 149×1. We divided the input data in a training dataset (87 %) and a test dataset (13 %) to assess the classification performance. First, we define material proportions based on the area of the trial pits. These were 11.33 %, 1.78%, 4.67% and 82.20% for the waste, soil, lime and bedrock respectively. Then we computed the joint probabilities $P(A_i|\rho, C, z)$, and derived the classification maps. Note that the MLP algorithm intrinsically uses the prior distribution in its training step (if one class has a higher probability, the algorithm will more often classify an unknown point in that category).

Interpretation – Classes prediction using MLP

Similar to the probabilistic approach, the training data were the values of $\{\rho, C, z\}$ co-located with the boreholes, which defined a matrix of 149×3 and corresponding vector of categories of 149×1. The training dataset was then divided to be 72 % of the total data, the validation dataset to optimize the hyperparameters 15 % and the test data set was the remaining 13 %. From the three MLP architectures that showed the largest classification performance, we selected the simplest one. It was composed of one hidden layer with 50 neurons, regularization value of 0.01, the rectified linear unit as activation function of the hidden layers and a quasi-Newton based optimizer as solver.

Comparison between the probabilistic approach and MLP

We use the same training data for both the probabilistic approach and MLP (training and validation after tuning hyperparameters) and we use the same test dataset to assess their performance. Figure 4.18 shows the category predictions for the probabilistic approach and MLP, the accuracy scores (which were 0.63 and 0.68 respectively) and the confusion matrices. In both approaches, the confusion matrix indicates that only the categories of waste and bedrock could be partially predicted.

First, we can observe that the MLP predicted model is strongly influenced by the inversion. The bedrock is predicted in the largest resistivity values and the lime is roughly predicted in the area of very low resistivities. The soil is predicted at some small areas of high chargeability (which might be artifacts in the inverted model), and as it was the class found at the largest depth of a pit at $x \approx 0$ m, then the soil was predicted in the area nearby at larger depths. This is a consequence of including spatial training data that is not distributed over the entire survey area (Baasch et al., 2018) and which may not reflect the real distribution of the materials deposited in the landfill. The waste is also predicted at larger depths in the model and might be influenced by the intermediate resistivity values. In addition, this model present

large areas of transparency representing probability values of around 30 %. This means that there are large uncertainties in the prediction of classes in nearly the whole model except in the area of the predicted bedrock.

The classification derived from the probabilistic approach is composed of a much simpler model. It mainly presents three nearly continuous deposits: a surficial layer of waste (with interspersed soil), an underlying layer of lime and the bedrock at the bottom, which is continuous along the whole model. Here, the zones of transparency are distributed in the shallowest layers along the profile, at a depth corresponding to the intersection between the lime and the waste. Nevertheless, this classification might present a more realistic geology, with continuous bedrock and a nearly continuous surficial layer of heterogeneous waste on the top of a lime deposit. In general, the anthropogenic-geologic scenario from the probabilistic approach might be more realistic as it agrees with the additional trial pit logs excavated near the profile's origin, where bedrock was found at similar depths than the ones presented here.

4.4 Discussion

We analyzed the performance of both approaches using a realistic synthetic benchmark and a field case where only few ground truth data are available. First, the MLP algorithm requires a previous optimization of the hyperparameters using a validation dataset (typically around 15 % of the available data set). Thus, when few data are available, optimizing the hyperparameters with a validation set can be difficult and yield highly variable results. For instance, several MLP architectures for the synthetic case led to large accuracy scores using the validation set (which may be a consequence of having few data). Nonetheless, the use of the algorithm on new data requires again an optimization of hyperparameters using a validation dataset, e.g., Aszemi and Dominic (2019) and Yu et al. (2020). Oppositely, in the field case, the accuracy scores were in general smaller during the optimization of hyperparameters and only few architectures presented scores over 0.7. In both cases, we selected relatively simple neural networks with a small number of hidden layers and neurons to remain in agreement with a small number of training data and to be comparable with the probabilistic approach where no data transformations are performed. In addition, during the optimization of hyperparameters we also observed larger accuracy scores in neural networks with smaller hidden layers and neurons.

Secondly, in the synthetic case the entire model domain was available to assess the performance of the algorithm. This was not the case for the field site, where the test data were only the 13 % of the ground truth data. For the latter, the classification

predictions were compared with the observation from excavations nearby. Finally, the transparency applied in this classification is derived from the probabilities of the output layer, derived from the Softmax function. Note however, that this function transforms the data into a probability vector with values between 0 and 1 and whose elements add up to 1. As it is a normalized exponential function, then the largest values are transformed into values close to 1 while the smallest into values close to 0. Therefore, the results may not represent exact probabilities as derived from the probabilistic approach, e.g., Gal and Ghahramani (2016).

The probabilistic approach does not require an initial tuning of parameters. The prior probability of the different categories or the categories proportion can be defined from the volumes obtained in the excavations. This information is essential to ensure that the conditional probabilities of each category are in line with the ground-truth data. If one category dominates the prior probability while the geophysical data are poorly informative, this can lead to a final classification favoring the most probable facies. This is the reason why in the field case, the bedrock lies across most of the model domain (especially in comparison with MLP classification). Finally, the transparency applied in this classification shows joint probabilities of the selected category, indicating specific zones of larger classification uncertainty. The probabilistic approach is also less dependent on the location and number of the co-located data.

The integration of more (inverted) data that increases the training dataset is likely to improve the performance of MLP while not necessarily the performance of the probabilistic approach. When the physical properties of the categories in the inverted model(s) are highly variable along the whole domain mapped, the classification uncertainty is likely to increase. Nevertheless, the predictions would still be in line with the material proportions or prior information from sampling. Note that the better the materials are resolved in the conditional probabilities given the geophysical or spatial variables, the better the performance of the probabilistic approach. Consequently, in highly heterogenous environments the probabilistic approach is likely to improve when it is applied locally, i.e., per profile if multiple profiles are available or in areas of a 3D model, depending on the heterogeneity observed in the conditional probabilities. Regardless, a representative sampling based on geophysical data, e.g., Van De Vijver et al. (2019), could improve data interpretation and therefore the classification performance of both methods.

Another option to increase the training data of the field case may be to use the data of the synthetic case. It is a common practice to create synthetic data to train artificial neural networks (Yu and Ma, 2021). Nevertheless, this contribution aims to present a

probabilistic approach as an alternative to perform a rapid quantitative interpretation of site-specific anthropogenic environments incorporating ground truth data.

We also studied the effect that the use of different data sources as training has on the probabilistic approach and MLP. Here we can notice that the category predictions derived from MLP are highly influenced by the spatial heterogeneity of the inverted models when we only use the geophysical data as input. This leads to several misclassification zones, the majority of which are nonrealistic. On the other hand, since the probabilistic approach relies on a Bayesian framework, it integrates the uncertainty related to data noise and inversion artifacts overall into the results. Therefore, the probabilistic approach is less sensitive to the heterogeneities of the inverted models when using only ρ and C, although it overestimates the distribution of the bedrock due to the large prior probability of this category. When we also include spatial training data (x, z), both approaches largely improve the classification, in particular MLP. However, including the position x in the probabilistic approach leads to a high degree of influence of the sampled location(s).

Additionally, we analyzed the effect that the number of boreholes and its distribution have on both approaches using the synthetic case. The distribution of a low number of boreholes can lead to variable accuracy scores (in particular for MLP). The accuracy scores of the probabilistic approach are very similar under the uniform and non-uniform sampling scenario.

Here we only compared the probabilistic approach with one algorithm of supervised learning, both of which presented classification models (overall) similar. Unsupervised learning has also been used for data interpretation in cases with minimal prior knowledge or where few ground truth data are available (Delforge et al., 2021; Sabor et al., 2021; Whiteley et al., 2021). These approaches have proven useful for the interpretation of geophysical data often in geological environments composed of layered models or when the geophysical method(s) resolve zones or structures, most of which, can be evidenced in intrusive data. The motivation of this probabilistic approach is to quantitatively interpret geophysical data in complex anthropogenic environments with extreme heterogeneity not only in terms of the spatial distribution of deposited wastes but also in terms of the high contrasts in physical properties that may lead to noisy data and artifacts in the inverted models. Since it provides probability values, its integration within other model types or in decision making is relatively straightforward, e.g., Hermans et al. (2015).

Both the probabilistic approach and MLP classify zones with large uncertainty. If the classification improves when adding the x and z information, this can also lead to local improvement while degrading the overall accuracy score. Another option is

then to improve the inverted model by adding the prior information from boreholes in the inversion process (Linde et al., 2015; Ronczka et al., 2015). For example, adding the depth of the bedrock, located in a low sensitivity zone, can improve the interfaces in the other part of the model (Caterina et al., 2014; Thibaut et al., 2021). However, adding such information bears the same limitation as it is highly dependent on the available boreholes and can lead to erroneous inverted models (Caterina et al., 2014). Nevertheless, using more advanced inversion methods does not prevent the use of the probabilistic approach nor the MLP algorithm for post-inversion classification. Hermans and Irving (2017) have shown that an appropriate regularization could lead to an increase in the confidence of the classification (higher probabilities).

4.5 Conclusion

In this study we presented a probabilistic approach that can be used in the classification problem including uncertainty estimation from site-specific multiple geophysical datasets and when only few ground truth data are available. The classification is based on two geophysical models (ERT and IP) and spatial data co-located with boreholes or trial pits. We compare this approach with a machine learning approach, the MLP, in both a synthetic model and in a real field case. In addition, we tested the effects that the types of (training) data sources and the borehole sampling have on both approaches.

The probabilistic approach has proven to provide robust results regarding the position and number of ground truth data and the presence of artefacts of inversion, in contrast to the MLP algorithm whose performance is largely related to the number of training data. Therefore, we recommend the use of the probabilistic approach in complex anthropogenic-geological scenarios or other site-specific environments where: 1) geophysical inverted models present spatial heterogeneities (laterally and vertically) or artifacts, 2) only few ground truth data are available, and 3) ground truth data might be sparsely distributed or not covering most of the area of study. The approach can be easily extended to integrate geophysical data from multiple methods or in three dimensions. It represents a suitable alternative to perform a rapid quantitative interpretation of geophysical data by using a probabilistic classification. Finally, as it integrates uncertainties in the prediction results, these can be used to complement decision support tools in a sustainable landfill management. In contrast, when a large number of training data are available, the MLP algorithm is expected to outperform the probabilistic approach.

4.6 Data and materials availability

Codes necessary to reproduce the classification using the probabilistic approach in the synthetic case and in the field case study are available at: https://doi.org/10.5281/zenodo.7121021.

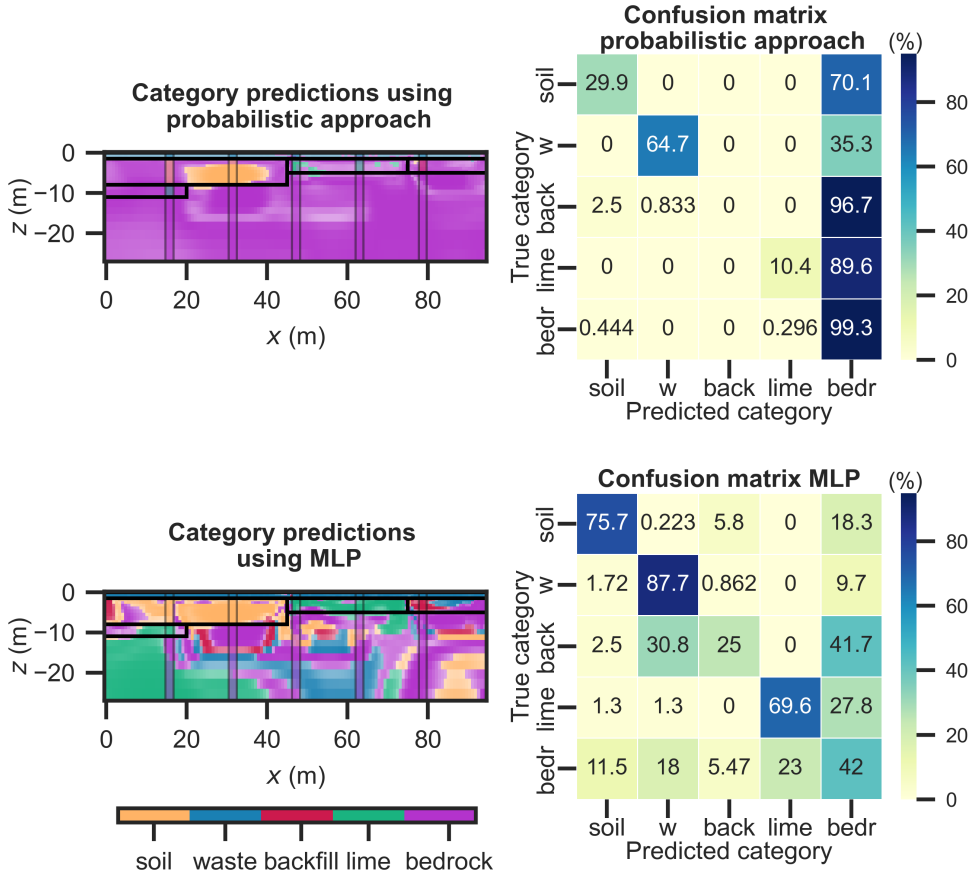

FIGURE 4.10: Category predictions of (a) probabilistic approach and (b) MLP algorithm using resistivity and chargeability data. For the former approach, minimum and maximum probability values are 44% and 100%, respectively, and 30% and 100% for MLP. The accuracy score for the probabilistic approach was 0.68 and 0.57 for MLP. The confusion matrices are displayed next to each model. The MLP model was built using three hidden layers with 50 neurons each, a regularization parameter of one, the rectified linear unit as an activation function of the hidden layers, and an optimizer based on the quasi-Newton method. In the confusion matrices, "w" refers to waste, "bedr" refers to bedrock, and back refers to backfill.

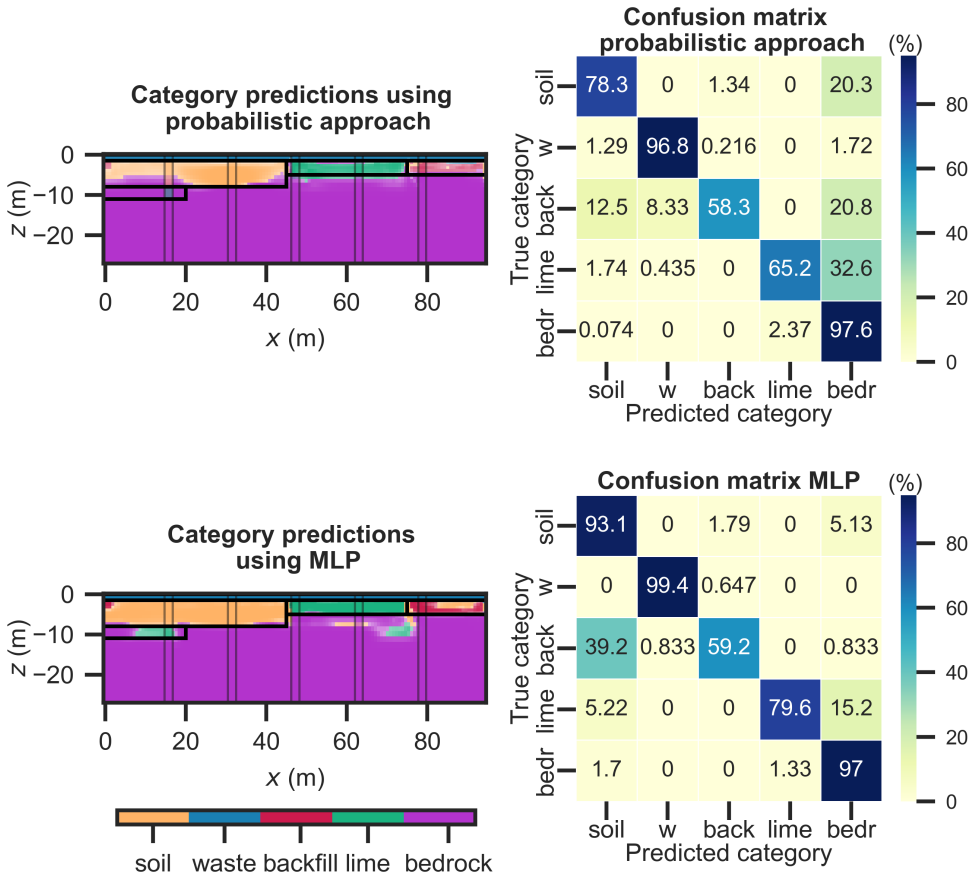

FIGURE 4.11: Category predictions of (a) probabilistic approach and (b) MLP algorithm using ρ, C and z. For the former, minimum and maximum probability values are 30% and 100%, respectively, and 41% and 100% for MLP. The accuracy score for the probabilistic approach was 0.89 and 0.93 for MLP. The confusion matrices are displayed next to each model. The MLP model was built using three hidden layers with 100 neurons each, a regularization parameter of one, the rectified linear unit as an activation function of the hidden layers, and an optimizer based on the quasi-Newton method. In the confusion matrices, "w" refers to waste, "bedr" refers to bedrock, and back refers to backfill.

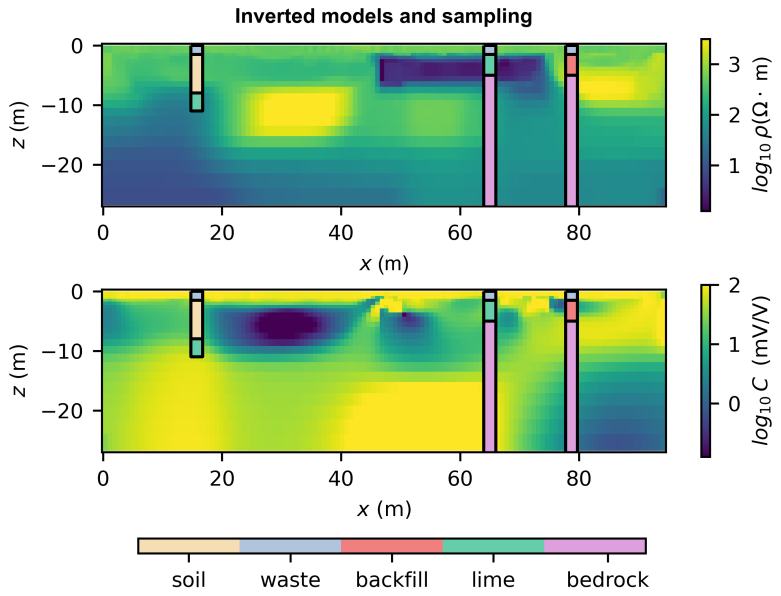

FIGURE 4.12: Nonuniform sampling scenario composed of three boreholes plotted with the inverted models.

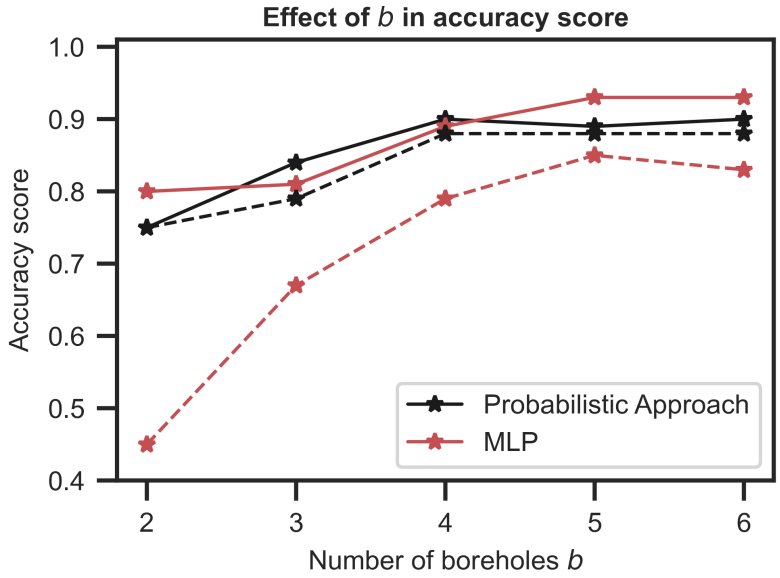

FIGURE 4.13: Plots of the accuracy score against the number of boreholes for the probabilistic approach (in black) and MLP (in red). The solid lines represent the sampling scenario of a uniform distribution of boreholes and the dashed lines represent the scenario of sparsely distributed boreholes.

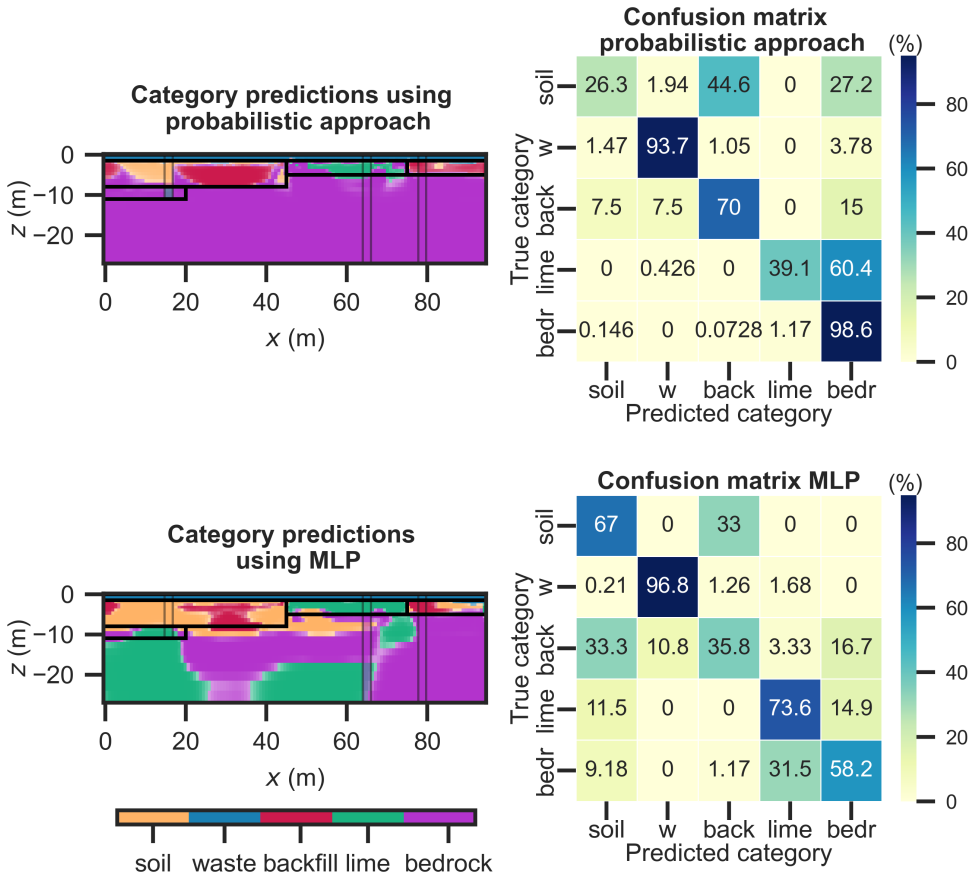

FIGURE 4.14: Category predictions of (a) probabilistic approach and (b) MLP algorithm using ρ, C, and z. The minimum probability values (higher transparencies) are 30% for the probabilistic approach, 45% for MLP, and 100% for the maximum probability values in both. The accuracy score for the probabilistic approach was 0.79 and 0.67 for MLP. The confusion matrices also are displayed next to each model. The MLP model was built using four hidden layers with 20 neurons, a regularization parameter of 0.1, the rectified linear unit as an activation function of the hidden layers, and a stochastic gradient-based optimizer. The distribution of nonuniform borehole sampling is shown in Figure 4.12.In the confusion matrices, "w" refers to waste, "bedr" refers to bedrock, and back refers to backfill.

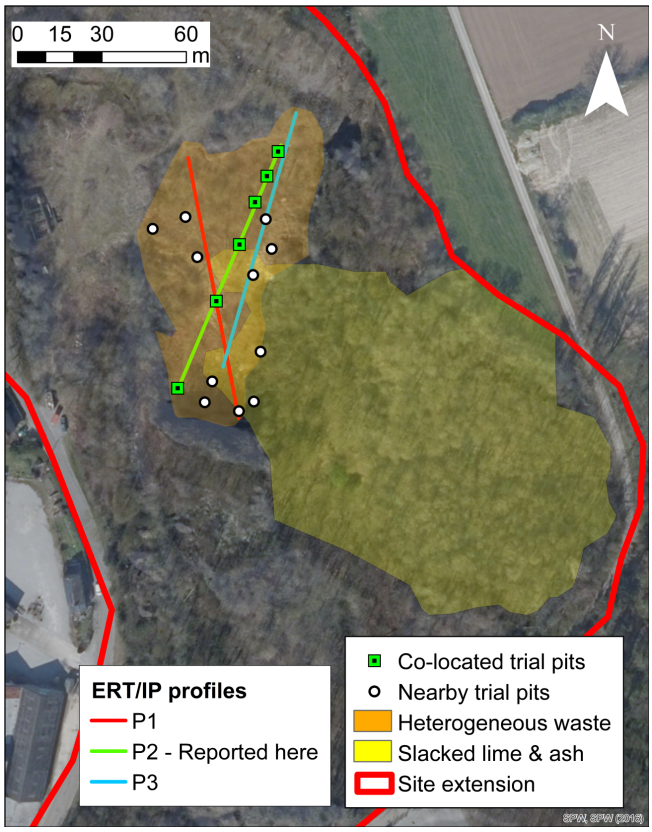

FIGURE 4.15: Map of the Onoz landfill, whose extension is indicated with the solid red line. The zone in orange is the lower part of the quarry, where heterogeneous waste was deposited, and the zone in yellow corresponds to the upper level of the quarry mainly composed of slacked lime and ash. P1, P2, and P3 show the locations of the ERT/IP profiles acquired in the lower part of the quarry. The square green symbols represent the position of trial pits colocated with a profile and used here, and the white circles are the trial pits excavated in the zone of the geophysical acquisition. The methodology that we present here was applied to profile P2 (in green) which is colocated with six trial pits.

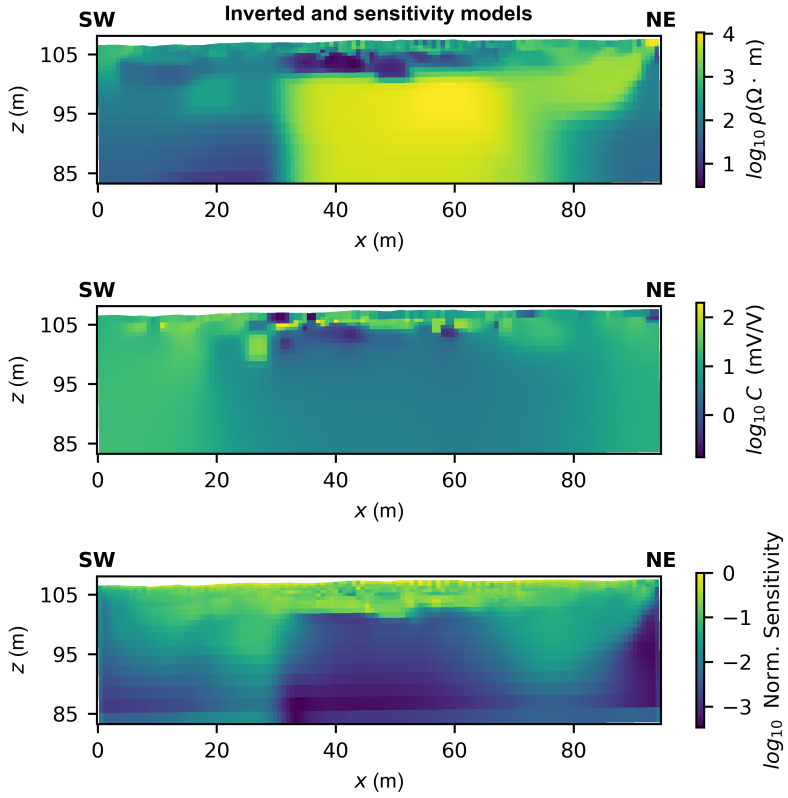

FIGURE 4.16: (a) Inverted resistivity model, (b) chargeability, and (c) associated sensitivity. The rms is 4.74 % and 3.36 % for the resistivity and chargeability models, respectively.

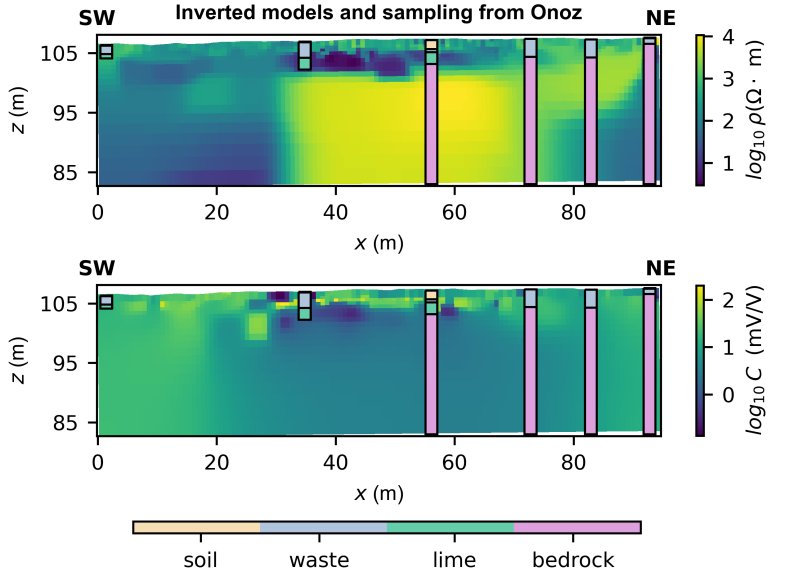

FIGURE 4.17: Colocated trial pits in the ERT and IP inverted sections.

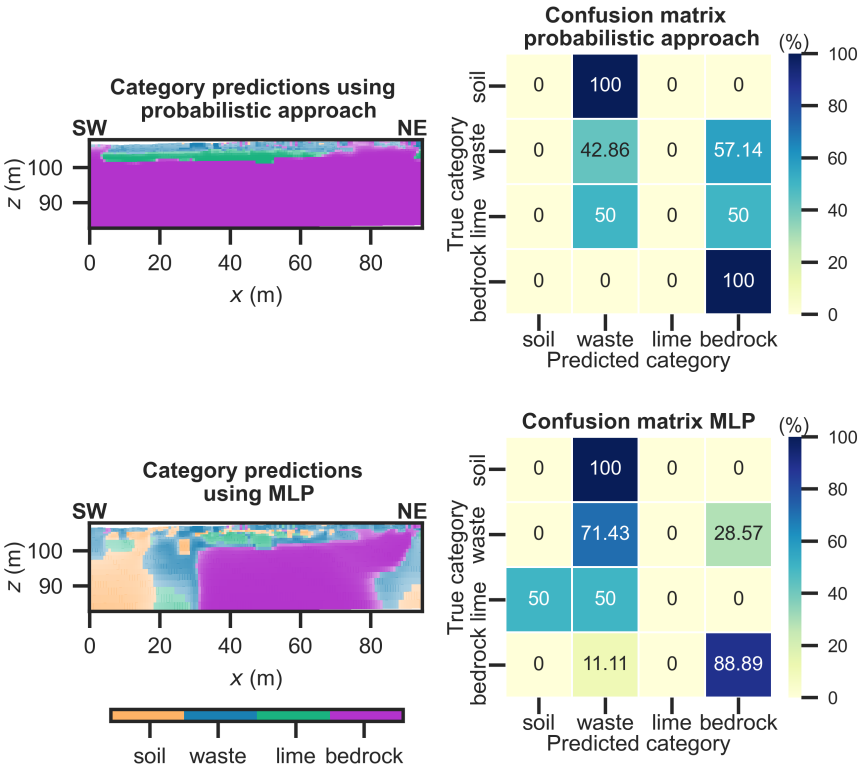

FIGURE 4.18: Category predictions derived for the (a) probabilistic approach and (b) MLP algorithm using ρ, C, and z. The minimum probability values (higher transparencies) are 35 % for the probabilistic approach and 33 % for MLP. The maximum probability value in both methods is 100 %. Corresponding confusion matrices are shown next to category predictions.

Chapter 5

Integrated methodology to link geochemical and geophysical-lab data in a geophysical investigation of a slag heap for resource quantification

The increasing need to find alternative stocks of critical raw materials drives to revisit the residues generated during the former production of mineral and metallic raw materials. Geophysical methods contribute to the sustainable characterization of metallurgical residues inferring on their composition, zonation and volume(s) estimation. Nevertheless, more quantitative approaches are needed to link geochemical or mineralogical analyses with the geophysical data. In this contribution, we describe a methodology that integrates geochemical and geophysical laboratory measurements to interpret geophysical field data in terms of the geochemical composition. The final aim is to estimate volume(s) of different types of materials to assess the potential resource recovery. We illustrate this methodology with a slag heap composed of residues from a former iron and steel factory. First, we carried out a 3D field acquisition using electrical resistivity tomography (ERT) and induced polarization (IP), based on which, a targeted sampling was designed. We conducted laboratory measurements of ERT, IP, spectral induced polarization (SIP), and X-ray fluorescence analysis. Afterwards, we identified groups of different chemical composition based on the geophysical and geochemical laboratory measurements. Its definition was supported through hierarchical clustering and principal component analysis. Then, we used the resistivity and chargeability inverted data collocated with the samples to fit 2D kernel density estimation functions for each group. Using Bayes' rule, we computed joint conditional probabilities in the whole domain of the inverted models and performed a classification. We found that a representative sampling and the

definition of the KDE bandwidths are defining elements in the computation of joint conditional probabilities and ultimately, in the classification. This methodology represents a suitable alternative to quantitatively interpret geophysical data in terms of the geochemical composition of the materials, integrating uncertainties both in the classification and the estimation of volumes[1].

5.1 Introduction

Former mining and metallurgical activities are often associated with the long-term contamination in soils, lakes, and estuarine sediments among others, which may be detectable even centuries after the end of activities on site (Asare and Afriyie, 2021; Cortizas et al., 2016). Simultaneously, the need of raw materials, metals and minerals, for the industry and the transition towards sustainable development for example in terms of energy, emphasize recent challenges faced by the mining industry, e.g., inaccessibility of deposits, decreasing grade of mined ores and land pressure (Žibret et al., 2020). Therefore, the increasing number of materials which are economically important and pose supply risks (Grohol and Veeh, 2023), highlight the need to explore alternative material sources.

Past mining and metallurgical sites offer an opportunity to mitigate this situation if we are able to assess the potential recovery of buried mine or metallurgical materials treated as waste, since mineral processing and metallurgical treatments were not as efficient as they are nowadays. What was considered as metalliferous wastes (dusts, slags, tailings, etc.) can therefore still contain valuable materials. Primarily, these residues may still contain valuable ferrous and non-ferrous metals, rare earth elements and other critical raw materials (Sethurajan et al., 2018) and ultimately, they could be reprocessed and used in the construction industry (Machiels et al., 2022) as aggregates or for cement. In this context, remediation strategies that aim to prevent or reduce the release of pollutants into the environment and reduce waste volumes can also be targeted to enhance secondary resource recovery (Izydorczyk et al., 2021; Vareda et al., 2019). To exploit such resources efficiently, it is crucial to have in-depth knowledge on the available quantities, composition, heterogeneity, and physical and chemical properties (Asare and Afriyie, 2021; Dino et al., 2021; Žibret et al., 2020).

[1]This chapter is based on: Isunza Manrique, I., Hermans, T., Caterina, D., Jougnot, D., Mignon, B., Masse, A., Nguyen, F., 2023, Integrated methodology to link geochemical and geophysical-lab data in a geophysical investigation of a slag heap for resource quantification. *Accepted pending reision, Journal of Environmental Management*

Geophysical methods have proven useful to characterize metallurgical wastes and associated contamination. To this aim, magnetic and electromagnetic methods have been used (often qualitatively) to identify these deposits, although geoelectric methods have been applied to a greater extent. For example, Mendecki et al. (2020) used electromagnetic induction (EMI) and electrical resistivity tomography (ERT) to delineate a slag waste dump from lead production. Additionally, samples were collected on the surface at six locations and analysis of X-ray diffraction (XRD), electron probe micro-analyzer (EPMA) and scanning electron microscope (SEM) were carried out to better interpret (qualitatively) the geophysical results. Martin et al. (2020) used ERT and ground penetrating radar (GPR), and spectral induced polarization (SIP) in the lab and in the field, to image the structure of a mine waste dump derived from silver and lead production. The geophysical results were calibrated using mineralogical analysis from multiple boreholes and a volume of potentially valuable residues was estimated interpolating several 2D ERT inverted profiles and using a resistivity threshold defined from the SIP lab results.

Other types of slags may not be easily detected using only ERT as indicated in Florsch et al. (2012, 2011), who used additionally magnetometry and induced polarization (IP) to estimate the volume of a slag heap from iron and steel production. The magnetic results supported the location of the ERT- IP acquisition profiles and the volume was estimated using a laboratory-derived linear relationship between the chargeability and the slag concentration. A review on this petrophysical model that accounts for the presence of disseminated metallic particles in a porous polarizable material can be found in Revil et al. (2022), showing that the chargeability of the material is linearly dependent on the volume fraction of the metallic ore and the chargeability of the background. The review also shows applications of the IP method and demonstrates its usefulness in the study of mineral and metallurgical deposits. In addition, SIP represents a promising method to investigate the evolution of complex mechanisms within metallurgical residues, such as oxidative-weathering mechanisms and oxidation-reduction processes (Placencia-Gómez et al., 2015; Slater et al., 2007).

Note that comprehensive characterizations such as mineral or metallurgical zonation, may require integrated approaches to link geophysical measurements in the field and/or in the laboratory with optimized sampling and metallurgical or geochemical analysis (Van De Vijver et al., 2021). For example, Lévy et al. (2019) qualitatively compare inverted spectral parameters from time domain 2D IP-ERT field data with in situ borehole measurements and SIP laboratory measurements to study the lithology and mineral composition of a geothermal area. In the lab, the mineral distribution

analysis and SIP measurements were carried out on 38 core samples from two boreholes located in the field acquisition domain and samples from two other boreholes westward from the study area. The methodology allowed to discriminate between zones rich in pyrite from those zones with iron oxides (magnetite-rich). Johansson et al. (2020) compared inverted SIP parameters from time-domain IP field data with SIP from laboratory measurements from a 50 m long rock core drilled along one field profile. The study was carried out on a limestone succession and the solid parts of the core were used for the analysis of physicochemical characteristics of the rocks in the laboratory. The results showed that the inverted parameters of the field data (closer to the borehole) were comparable to the SIP lab measurements despite the differences in measurements techniques and scale. In addition to the laboratory derived petrophysical models to infer on the structural or chemical characteristics of materials using geophysics, statistical analyses may be used. Inzoli et al. (2016) conducted SIP lab measurements to infer the litho-textural properties of alluvial sediments. The authors carried out a cluster analysis and a principal component analysis (PCA) using the parameters of a Debye decomposition on the SIP data measured in 55 samples with varying saturation (from originally 19 samples collected at 3 sites).

Techniques to ultimately interpret field data, considering the link between laboratory and field measurements, have been developed through classification. For example, Vásconez-Maza et al. (2019) predicted the distribution of chromium in an abandoned phosphogypsum pond through a classification of ERT field data. The authors used a non-linear relationship between the concentration of chromium measured in the lab and the inverted field resistivity collocated with the samples' positions. More recently, Martin et al. (2021) investigated slags from different historical dumps derived from processing of metal ores to extract copper, lead, silver and zinc among others. The authors measured SIP in the laboratory and carried out geochemical and mineralogical analyses in some samples collected at the surface or at maximum depths of 0.5 m. In the field, they collected two 2D SIP profiles with a limited bandwidth. Three slags grades could be identified in the laboratory and in the field based on the polarization magnitude. Additionally, the slags could be classified in five categories according to the shape of their spectra which could reflect the diversity of environmental parameters such as saturation or fluid conductivity.

In this contribution, we propose a quantitative approach to integrate laboratory and field measurements to perform a 3D classification within a slag heap in a probabilistic manner. The main objective is to define a zonation based on chemical composition and to estimate the volumes of different materials within the slag heap for potential resource recovery. To this aim, we followed a quantitative approach that

integrates: 1) 3D ERT and IP measurements in the field, 2) a targeted sampling with samples' collection at 22 different positions in the heap, 3) laboratory measurements of ERT, IP and SIP and 4) a chemical characterization of samples through X-ray fluorescence (XRF) analysis. We used laboratory measurements and chemical analysis to identify groups of samples of different composition and properties. The identification of these clusters was supported by studying the relationships between the chemical and geophysical variables, an unsupervised clustering algorithm (hierarchical clustering), and a PCA analysis. Then, we linked the laboratory with the field measurements by fitting the resistivity and chargeability field data collocated with the sampling using 2D kernel density estimation (KDE) functions for each previously defined group. Afterwards we computed the joint conditional probabilities in the whole field domain. Lastly, we classify the 3D inverted models in terms of the groups and compute the corresponding volumes.

5.2 Site description

The site of Duferco – La Louvière, located in the Province of Hainaut (Belgium), is an idled factory of iron and steel production that started its activities around 1850 and officially stopped in 2013. The site evolved and reached its final infrastructure in 1981, integrating elements such as a coking plant, blast furnaces and agglomerations of by-products and raw materials in the northeast zone (see Figure 5.1a). In this contribution, we study the storage of slags located in the northern zone of the site where the backfilling started around 1930's and comes from steel works and blast furnaces. In the last decades of activity, the materials of the slag heap were mostly produced from electric arc furnaces and in particular from the ladle refining furnaces. These materials are typically rich in lime and alumina. It is likely that the most recent layers in the western area of the heap contain a mixture of residues (e.g., scrap metal, wood and refractories).

5.3 Methodology

Figure 5.2 shows the workflow of the quantitative approach which integrates field and laboratory measurements through a targeted or geophysics-based sampling. Then, all the data is studied through a statistical analysis where different groups or clusters representing distinct types of materials are identified. Finally, a probabilistic classification is conducted in the whole field data domain and the volumes of each group are estimated.

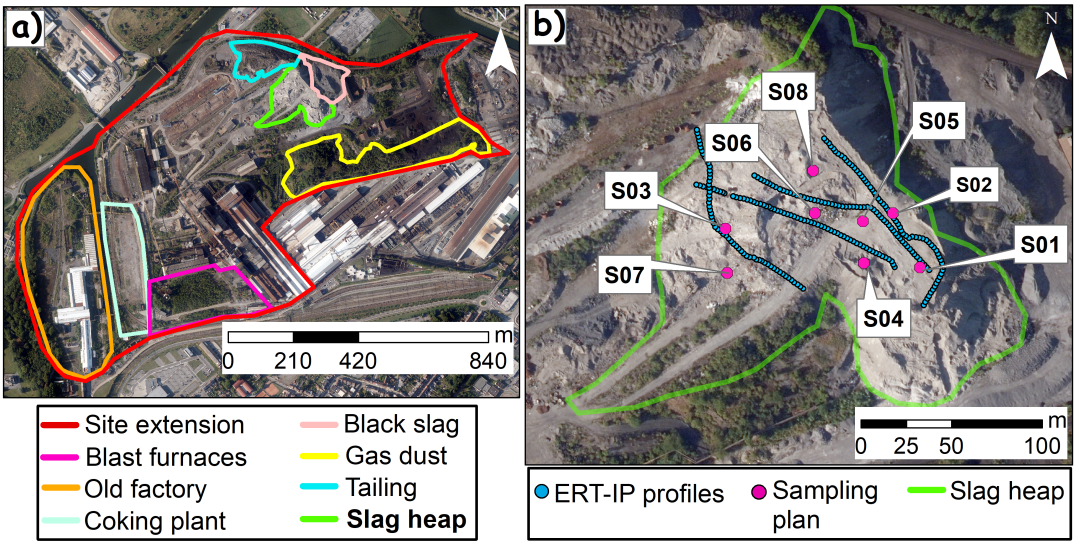

FIGURE 5.1: a) Map of Duferco -La Louvière with the different production and agglomeration zones, b) Location of the ERT-IP acquisition profiles (blue) and sampling plan (pink) in the slag heap.

5.3.1 Field measurements and targeted sampling

First, we measured ERT and time-domain IP along four profiles deployed across the entire slag heap and each profile was composed of 64 stainless electrodes spaced by 2 m (see Figure 1b, blue dots). Data acquisition was carried out simultaneously on combinations of two profiles, with inline and crossline measurements, to obtain truly 3D information for the inversion (Van Hoorde et al., 2017). A gradient array with a "s" factor equals to 7 was used (Dahlin and Zhou, 2006) and it was complemented with a bipole-bipole acquisition. This 3D acquisition was a tradeoff between the maximization of the heap's coverage and the spatial resolution. Electrical current was injected for 2 s and the voltage decay was measured for 1.86 s after the current was switched off. Two stacks (repetition error) and a sample of reciprocal measurements were collected to assess data quality. Then, data were filtered removing measurements with a repetition error greater than 5 % in resistance. The error model from reciprocal measurements was to 0.029 Ω and 2.27 % for the absolute and relative errors (Slater et al., 2000). The data were inverted with BERT (Günther et al., 2006) using a robust constraint on the data and blocky constraint on the model to derive 3D models of electrical resistivity and chargeability while respecting the noise level ($\chi^2 = 1$).

Secondly, we designed a targeted sampling based on the contrasts observed in the ERT and IP models, i.e., targeting zones of low, intermediate and high resistivity/chargeability values and covering most of the (shallow) observed contrasts in the

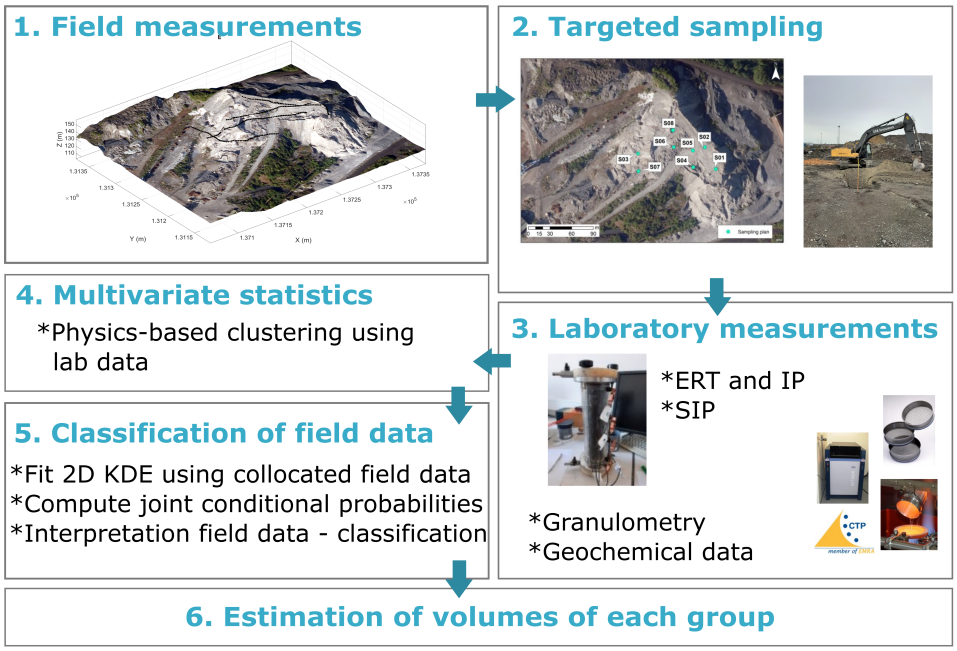

FIGURE 5.2: Workflow of the integrated approach. 1) Field measurements are carried out, then 2) the sampling survey is designed and samples are collected. 3) Geophysical and geochemical measurements are conducted in the laboratory. 4) These results are then studied through multi-variate statistics and several groups of different geochemical/geophysical composition are identified. 5) Based on 2D KDE distributions using the field data collocated with the samples positions and the computation of joint conditional probabilities for each group, the field data are classified. 6) Volumes of each group are computed considering the sensitivity of the inverted models and the joint conditional probabilities.

inverted models. Samples were collected at 8 locations on the heap at depths of 1, 3 and 5 m (see locations in Figure 5.1b, pink dots). During the sampling we took approximately 10 – 15 kg of material in buckets that were sealed and stored in a cold environment. The maximum depth of excavation was limited by the terrain stability, the hardness of the soil and the machine used. Additionally, heterogeneous waste at one location impeded the collection of material at two depths, therefore in this study we use 22 samples in total. As will be explained in the results, based on the inverted models, we assume that the 22 samples taken at different positions (x, y, z) captures the variations of physical and chemical properties in the slag heap.

The identifiers we use to refer to the samples indicate its location followed by an underscore and the depth of collection, i.e., S01_3 is the sample located at S01 collected at 3 m.

5.3.2 Laboratory measurements

Geophysical data

The laboratory measurements were carried out using the samples as they were collected in the field, i.e., no re-saturation, as the aim was to measure their properties in the same conditions as in the field. Geophysical measurements of resistivity (ρ_{lab}) and chargeability (m_{lab}) were carried out using columns of 1.5 dm^3 (0.08 m diameter $\times$ 0.3 m length, see Fig.5.3). The potential electrodes are made of brass and the current transmission porous plates, which are in the bases of the cylinder, are made of bronze.

FIGURE 5.3: Column used for geophysical laboratory measurements of ERT, IP and SIP.

First, the geometric factor KG was estimated based on the resistance measured when the column was filled with water at a known conductivity (KG = 0.045 m^{-1}). We then filled the columns with 1 to 1.5 kg of the material of each sample. First, we measured the electrical resistance and the time-domain chargeability using 4 electrodes with a Wenner array. Electrical current was injected for 2 s and voltage decay was measured for 1.86 s after switching the current off, as for the field data. Two stacks were collected to have a repetition error which was < 1 % in resistance for all the samples. Then we measured SIP in the same columns using the impedance analyzer ZEL-2-SIP04-V05 (Zimmermann et al., 2008). The impedance and phase shift were measured in the range of 10 mHz to 45 kHz for the reciprocal and normal setup, leading to a high phase accuracy of 0.1 mrad (below 1kHz).

Granulometry and geochemical data

Geochemical analyses were conducted in the same volumes of samples as those used for the geophysical laboratory measurements. First, each sample was sieved to determine the particle size distribution. Then, the subsamples at the different particle

sizes were analyzed using X-ray fluorescence (XRF) for major elements (e.g., Fe, Si, Mn, Ca). Finally, the average content over all particle sizes was computed per element for each of the 22 samples. The average content of only six elements was larger than 1 wt. % for all samples: Si, Ca, Fe, Mg, Al and Mn. The elements with the largest concentrations were Si, Ca and Fe with average contents up to around 30 wt. %.

5.3.3 Multivariate statistics

The objective of this step is to identify groups of samples with different chemical composition and simultaneously, to identify the geophysical parameters that can distinguish these groups.

First, we studied the linear correlations between pairs of the chemical elements constituting all the samples (average content). We applied a standardization of the data by removing the mean and scaling to unit variance, and then we computed the Pearson' correlation coefficients. The standardization of the data allows to compare the variations of the different variables using the same scale. At this step we consider strong positive and negative correlations of elements as a first indicator of different types of slags.

Afterwards, we computed the pairwise Pearson' correlation coefficients between the geochemical variables and the geophysical variables measured both in the laboratory and in the field. The field measurements were obtained from the inverted resistivity and chargeability models, computing an average of the cells within a volume of dimensions 3 m $\times$ 3 m $\times$ 1.6 m centered at the positions where the samples were collected, i.e., ρ and m. The correlations were also computed using previously standardized data.

Furthermore, we studied the relation between the resistivity and the chargeability measured in the laboratory, together with the concentration of some chemical elements with which the largest correlations were observed, to identify groups or clusters of different composition. Similarly, we analyzed the scatterplots of the imaginary and real components of the conductivity measured in SIP.

We carried out an unsupervised learning approach (hierarchical clustering) to group the samples from the lab data and compare it with the groups previously identified. Lastly, we applied PCA to support the geophysical-geochemical-based definition of groups in the principal component space, using the standardized geochemical and geophysical data. This technique was executed using the python library of scikit-learn (Pedregosa et al., 2011).

5.3.4 Classification of the field data

In the literature, we can find quantitative interpretations of inverted geophysical data integrating ground truth data and which are based on machine learning (Lysdahl et al., 2022; Moghadas and Badorreck, 2019; Whiteley et al., 2021) and exclusively on statistics or probability theory (Dewar and Knight, 2020; Hermans and Irving, 2017; Isunza Manrique et al., 2023).

Here, we used a probabilistic approach to interpret the field data in terms of the classes or groups previously identified using laboratory measurements. Similar to Isunza Manrique et al. (2023), we derive joint conditional probabilities of each identified group in the whole field range, using the volume-averaged field data ρ and m collocated with the sampling, but here, we use a different probability density function in 2D. Note that variations of resistivity are not expected to be indicators of different types of slags (Florsch et al., 2011) but potential indicators of different types of materials within the heap, while a linear relationship has been observed between the chargeability and slag concentration (Florsch et al., 2011; Qi et al., 2018). The kernel density estimator $f_{KDE}(y)$ at a point y based on a dataset of points x_j for $j = 1 \dots N$ is defined as

$$f_{KDE}(y) = \sum_{j=1}^{N} K(y - x_j; h)$$

where K is the kernel and h is the bandwidth.

First, we used 2D KDE's to model the distributions of the volume-averaged field data $\mathbf{x}_j = (\rho, m)_j$ for each group A_i ($i = 1 \dots 4$), using a Gaussian kernel expressed as $K \propto exp(-x^2/2h^2)$. The bandwidth was estimated using the data-based Scott's Rule which considers the number of data and dimension, and an estimate of the standard deviation of the bivariate data distribution (Scott, 2015; Virtanen et al., 2020). Then, we estimated the KDE's functions at all the inverted resistivity values (**P**) and chargeability values (**M**), i.e., whole field data domain $\mathbf{y} = (\mathbf{P}, \mathbf{M})$, as

$$f_{KDE}(\mathbf{y}|A_i) = \sum_{j=1}^{N} K(\mathbf{y} - \mathbf{x}_j; h) \tag{5.1}$$

Afterwards we used Bayes' rule and computed the joint conditional probabilities $P(A_i|\mathbf{y})$ of each group. The prior probability values $P(A_i)$ were estimated from the number of lab samples belonging to each group.

Each grid cell of the inversion is then classified in the group having the largest joint conditional probability, while the probability itself gives an idea of the uncertainty of the classification.

5.3.5 Estimation of volumes

Once the inverted model is interpreted in terms of groups or classes, we estimate the volumes of each group according to the corresponding cells' mesh. As each cell has been classified on the basis of a joint conditional probability, groups selected as the most likely class that have low probability values can be overestimated while groups with smaller probabilities can be underestimated. To integrate this classification uncertainty into account, we estimate the volume of each group V_i by adding the volume of the corresponding cell v, weighted with the corresponding value of joint conditional probability $P(A_i|\mathbf{y})$, see Canters (1997), as

$$V_i = \sum_{j=1}^{N} P(A_i|\mathbf{y})v \tag{5.2}$$

5.4 Results

5.4.1 Inverted ERT and IP models and sampling

The inverted models are displayed in Figure 5.4 for several cross-sections along the x and y axis. These include a (normalized) cumulative sensitivity threshold (>$10^{-5.5}$) to keep only parts of models that are sufficiently well covered (Caterina et al., 2013). The sensitivity model is shown in Figure 5.5. We selected this threshold to ensure that the areas in the vicinity of the electrodes were considered (laterally) and additionally, it led to include bottom elevations that have been reported as the original topography before the activities in the factory (approximately 110 – 115m). In Figure 5.4a we can note, overall, zones of larger resistivities towards the east and west end of the heap. Smaller resistivity values can be observed downhill of the heap (towards the west) at larger depths. In the chargeability model (Fig. 5.4b) we can observe shallow layers of large chargeability values and in particular a large zone which is distributed southeast- northwest with values up to 250 mV/V.

Based on the inverted models, the targeted sampling was composed of 22 samples collected at 8 different locations of the heap and at different depths of 1, 3 and 5 m (Figs. 5.1b and 5.4). Most of the samples were slags of similar color and structure except samples S04_5 and S05_3 which were mostly crushed bricks (see Figure 5.6).

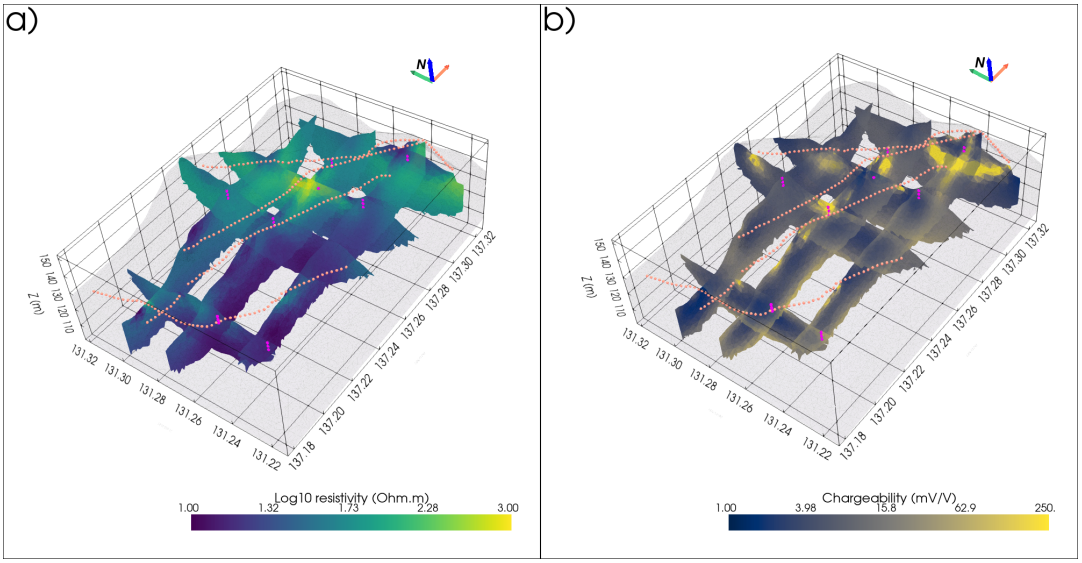

FIGURE 5.4: 3D inverted models of a) resistivity and b) chargeability. Electrodes used in the acquisitions are shown in the heap ground surface as small salmon dots. Sampling location is indicated with the pink spheres.

The sampling survey targeted different zones of the inverted models, e.g., high and low values of resistivity and chargeability, combinations of large/low chargeability values and large/low resistivity values. Therefore, we assume that the collection of 22 samples taken at different positions (x, y, z) captures the variations of physical and chemical properties in the slag heap. In particular, note that the sharpest contrasts in the inverted models of resistivity and chargeability are in the shallowest zones. Then, we assume that the calibration of geophysical data with ground truth data observed at the first 5 meters of the heap, can be extrapolated at larger depths, although the sensitivity and discriminating ability of ERT/IP decreases (Hermans and Irving, 2017; Isunza Manrique et al., 2023).

5.4.2 Laboratory measurements

ERT, IP and SIP data

Figure 5.7a and 5.7b show the laboratory measurements of resistivity and chargeability respectively. Most of the samples present similar ranges of resistivity (ρ_{lab}) with slight variations with depth, except for samples S04 and S08, which present an increase and strong decrease of ρ with depth respectively. In terms of chargeability (m_{lab}), samples S06 and S02 present the largest values while sample S05 has $m_{lab} < 10$ mV/V. Overall no tendency is observed for the variations of chargeability with depth.

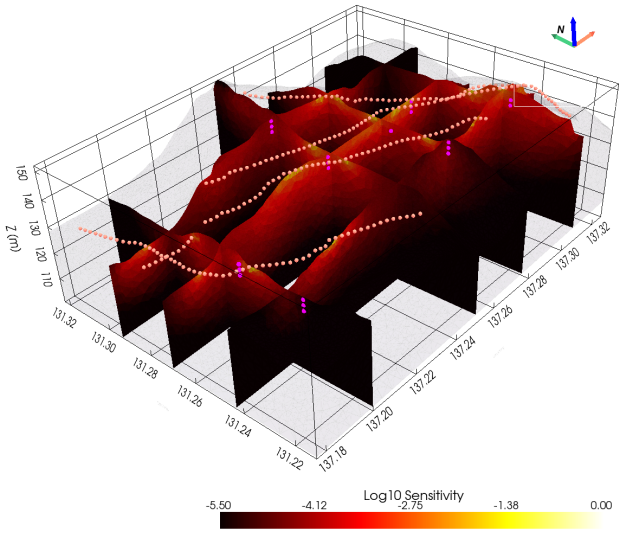

FIGURE 5.5: 3D sensitivity model associated with the inverted models of Figure 5.4. Electrodes used in the acquisitions are shown in the heap ground surface as small pink dots. Sampling location is indicated with the magenta spheres.

FIGURE 5.6: Sampling across the slag heap and collection of S03_5, S04_5 and S08_3 (see location in Figure 3, pink dots).

Figure 5.7 also shows an overview of the SIP measurements through the magnitude of the resistivity $|\rho|$ (Fig. 5.7c), the real and imaginary components of the conductivity, σ' and σ'' (Figs. 5.7e and 5.7f), and the phase ϕ (Fig. 5.7d). We also included the SIP spectra of a water bearing column. Note that σ' increases with the frequency and σ'' displays a peak for most of the samples. In terms of the phase, we found that most of the samples are characterized by a peak of varying magnitudes, centered at around 1 Hz. This behavior has been reported before in iron slags, e.g., Florsch et al. (2011). S06 and S02 present the largest polarization magnitude through σ'' similar to the displayed largest chargeability.

Granulometry and XRF analysis

We compared the mass distribution of the samples at several size particles, from 65 μm to 40 mm, with the concentration of different elements (Fig. 5.8). On average, we observed that the mass of all samples was slightly higher in the particle sizes of 65 μm and from 10-40 mm. In terms of elements distribution, we noted that the calcium was distributed homogeneously in all the particle sizes for most of the subsamples although on average, the largest Ca concentration is observed in the particles of 10 mm. Secondly, the largest Fe concentrations could be observed at the particle sizes > 1 mm and the same pattern was observed for Mn. Lastly, only three samples presented larger concentrations of Si, which was homogeneously distributed over all particle sizes.

5.4.3 Multivariate statistical analysis

Geochemical variables

Focusing on the elements with the largest weight concentrations (Si, Ca and Fe), we observed that Fe is largely correlated with Cr, V and Mn and negatively correlated with Al. Ca presents strong positive correlations with Sr and Mn, and negative correlations with Si, Ti and K. Si on the other hand, is largely correlated with Ti, K and Al and negatively correlated with Ca and Mn. This may indicate that the Fe group has a low concentration of Al and the Si group may have a low Ca content. Finally, note that some elements do not have pairwise strong correlations nor correlations with the elements above mentioned, these are Ni, Cu, S and Zn. The Pearson's correlation matrix between pairs of chemical elements concentrations is presented in Figure 5.9.

Geochemical, lab-based and field-based geophysical variables

Figure 5.10 includes correlations between 1) the chemical elements which are considered indicators of different types of slags (see section above), 2) resistivity and chargeability laboratory measurements indicated as ρ_{lab} and m_{lab} (see section 5.3.2), 3) the SIP measurements, specifically, the values of the real and imaginary components of the conductivity and the maximum magnitude of the phase observed at the polarization peak, as well as the frequency of the phase peak or critical frequency, i.e., σ'_{peak}, σ''_{peak}, $|\phi_{peak}|$ and f_{peak} respectively, and 4) the values of resistivity ρ and chargeability m of the 3D inverted models (volume-averaged values centered at the sampling location). The yellow squares indicate the elements which are part of the critical raw material list of EU for 2023 (Grohol and Veeh, 2023).

First, we can note that the measurements of resistivity in the lab (ρ_{lab}) and in the field (ρ) present strong correlations (>0.7) with the Si group previously identified. Then, the values of m_{lab} present large correlation with the Fe group with Fe (0.65), Mn (0.84), V (0.93) and Cr (0.82), while the values of chargeability from the field present a large correlation coefficient only with V. Regarding the SIP parameters, we did not observe correlations between σ'_{peak} nor σ''_{peak} and chemical elements, but large coefficients were observed between $|\phi_{peak}|$ and the Fe group: Fe (0.75), Mn (0.83), V (0.93) and Cr (0.74). Lastly, there were no strong correlations between the SIP parameters and the concentrations of chemical elements in addition to those observed with m_{lab}.

As noted before, the values of ρ_{lab} and ρ present a strong positive correlation with the elements of the Si group (Si-Ti-K). Additionally, m_{lab} and m presented high correlations with the chemical elements of the group Fe, in particular m_{lab}, probably due to the sensed volume. The comparison between laboratory and field measurements, shows strong positive correlations (0.72) between ρ_{lab} - ρ and m_{lab} – m, which integrates the different sampled volume and the field and lab conditions. The discrepancy gives an idea of the scale and inversion effects on the validity of laboratory-derived petrophysical relationships, e.g., Benoit et al. (2019). In terms of the SIP parameters, note that there is a correlation of 0.82 between the imaginary and real components of the conductivity, which is a behavior that has been observed for several materials (Flores-Orozco et al., 2020). Although it is expected that the frequency peak is correlated with the particle size, this was not observed (results not presented here). Note that the samples do not have a predominant particle size (see section 5.3.2) which may explains the broad peaks in the phase spectra. Here, we included f_{peak} in the correlation matrix to study if variations in the composition of the slags could be discriminated through peak shifts in the phase spectra. However, no strong correlations were obtained with the geochemical variables.

There were two analyses that are not included in the correlation matrix of Figure 5.10. First, we studied the correlations between the positions at which the samples were collected (x, y, z) and the geochemical and geophysical variables, however, no relations were found. This means that there are no preferential zones of similar composition within the heap (laterally nor vertically at least at the sampling resolution used here). Additionally, we fitted a double Cole-Cole model (Cole and Cole, 1941; Pelton et al., 1978) to the SIP phase spectra and studied the correlations between the spectral parameters (i.e., m, τ, ρ) and the geochemical variables to determine its ability to resolve composition variations. Nevertheless, no additional correlations were found, in addition to the complex conductivity parameters presented here.

In the following, we analyze the scatterplots of the ρ_{lab} - m_{lab} together with the concentration of some chemical elements with which the largest correlations were observed (i.e., Fe, Si and Mn) to identify groups or clusters of different composition. For comparison with the complex conductivities from SIP we will work with the conductivities σ_{lab} ($1/\rho_{lab}$). These scatterplots are displayed in Fig. 5.11a-c, with colorbars representing the average content of Mn, Fe and Si. We showed these elements due to the large correlations observed with the geophysical properties in Fig. 5.10 and their average concentration > 1 wt. %. First, we can note that the samples S04_5 and S05_3 can be identified with small chargeability values and small conductivities as well as large values of Si (likely to belong to the Si group mentioned in section 5.4.3). The remaining samples present intermediate to large concentrations of Fe and Mn and a small content of Si. Within this group, three clusters are observed. A cluster with the samples of largest chargeability and conductivity values (i.e., S02_3, S02_5, S06_1, S06_3, S06_5); another cluster with values $m_{lab} < 70$ mV/V and intermediate Fe-Mn content, i.e., S01_1, S01_3, S01_5, S03_1, S03_3, S03_5, S04_1, S04_3, S07_1, S07_3, S07_5, S08_5; lastly, a small cluster with $m_{lab} > 70$mV/V, i.e., S02_1, S08_1, S08_3 (see Table 5.1). Nonetheless, the boundary of the last two groups is not clear as large concentrations of Fe-Mn can be observed for broad ranges of conductivities.

For comparison, we also analyzed the crossplots of σ''_{peak} vs σ'_{peak} and the average concentration of Mn and Fe (Figures 5.11d-e). Similar to the ERT/IP measurements we can also observe that the samples attributed to Group 1 present the smallest values of σ''_{peak} and have low concentrations of Mn and Fe. Then, we can observe that the samples constituting groups 2, 3 and 4 are distributed along different linear relations σ''_{peak} - σ'_{peak} as shown through the fittings of linear models displayed in Figures 5.11d-e. We computed the coefficient of determination of these regressions and obtained R^2 = 0.98, R^2 = 0.93, and R^2 = 0.85 for the linear fittings in Group 2, 3 and 4 respectively. This supports the definition of the four groups and the attributed samples, as each of these linear models may represent different types of materials (through different phases, $\phi \approx \sigma''_{peak}/\sigma'_{peak}$).

Afterwards, we carried out an unsupervised learning approach to group the samples from the time-domain lab measurements. Note that previous grouping was done integrating geochemical data while this approach only used geophysical parameters and can be obtained without samples. We applied a hierarchical clustering to previously standardized data, assuming four clusters and a single linkage as the metric criteria, i.e., minimizes distance between the closest observations of clusters pairs (Pedregosa et al., 2011). The results show that the clustering and the previous

TABLE 5.1: Samples identified in each group from chemical analysis and geophysical lab measurements.

Group identifier	Samples	σ_{lab} (mS/m)	m_{lab} (mV/V)	Dominant concentration
Group 1	S04_5, S05_3	< 20	< 20	Si
Group 2	S02_3, S02_5, S06_1, S06_3, S06_5	> 20	> 100	Fe-Mn
Group 3	S01_1, S01_3, S01_5, S03_1, S03_3, S03_5, S04_1, S04_3, S07_1, S07_3, S07_5, S08_5	> 14	< 90 > 20	Intermediate Fe-Mn
Group 4	S02_1, S08_1, S08_3	< 25	> 70	Intermediate Fe-Mn

geophysical-geochemical grouping (Table 5.1) converge to similar group identification, which validates the proposed grouping. However, as the clustering minimizes the distance between the closest observations of pairs of groups, it can be sensitive to the initial model or the initial number of clusters (see Figure 5.12).

Principal component analysis (PCA)

We applied PCA to the previously standardized geochemical and geophysical data shown in the correlation matrix of Figure 5.10. The first three principal components (PC's) represent a variance of 55.35 %, 15 % and 10.22 % respectively, which add up to around 80 % of the total data variance.

First, we investigated how the samples (and clusters previously observed) were distributed in the PC's space (Figure 5.13a-b). Focusing on the plot of PC2 vs PC1, we can again identify samples S04_5 and S05_3 (Group 1) as outliers which largely represent the data variance along PC1. Then, the samples with the largest values in the PC2 axis agree with the samples of largest chargeability and conductivity measurements (Group 2). In contrast, the samples with the smallest values in the PC2 axis constitute Group 3 and intermediate values in the PC2 axis correspond to Group 4. Overall, we can note that there are no overlaps of groups' samples.

Additionally, we computed the linear correlations between the PC's and the original variables using the correlation circles (Figure 5.13c-e) for the first three PC's. Squared loadings are additionally presented in Figure 5.14. Note that PC1 presents strong correlations with most of the variables, e.g., positive large correlation with Si, Al, ρ_{lab}, ρ and negative correlations with Fe, Ca, Mn, m_{lab}, $|\phi_{peak}|$. PC2 is predominantly related to the field resistivity and chargeability although the correlation coefficients with all variables are overall low. Lastly, PC3 is mainly related to the

laboratory measurements of complex conductivity (σ''_{peak}, σ'_{peak}, f_{peak}) with which it is strongly correlated.

5.4.4 KDE's and probabilistic classification of field data

For visualization, we computed the 2D KDE's at a regular grid in the range of the inverted resistivity and chargeability models, based on the functions fitted with the volume-averaged field data (see Figure 5.15a-d). The bandwidth of each group was estimated using Scott's rule. However, as the data distribution of Group 1 was over-smoothed, we decreased h from 0.56 to 0.3. On the other hand, the distribution of Group 3 was strongly influenced by the outliers, therefore, we slightly increased h from 0.19 to 0.3. This allowed to smooth the estimates increasing the covariance of the data distribution. In addition, these values of h led to classification results which are overall in line with the proportion of the groups 1-3 (or prior probabilities).

Then, we computed the 2D KDE's $f_{KDE}(\mathbf{y}|A_i)$ (see Eq. 5.1) and the joint conditional probabilities $P(A_i|\mathbf{y})$ at the whole field data domain, for each group. The prior probability values $P(A_i)$ were estimated from the number of lab samples belonging to each group, these are 9 %, 22 %, 54 % and 13 % for groups 1- 4 respectively.

Figure 5.15e-f also shows the classification of the field data, based on the largest joint conditional probabilities, as well as the volume-averaged field data (ρ, m) from which the 2D KDE's were built. In Figure 5.15e the maximum transparencies represent the smallest probabilities of 33 % and in Figure 5.15f we plot only the data with probability values larger than 50 %. Note that the smallest probabilities of classification are distributed in the boundaries of the groups.

5.4.5 Estimation of volumes

Figure 5.16a-b shows the classification of the data along the same sections displayed before for the inverted models and the corresponding joint conditional probabilities with which each group or class was assigned. The maximum probability values are 1, 0.95, 1 and 0.85 for groups 1-4 while the minimum value with which the groups were selected was around 0.3.

Figure 5.16c-f shows the volumes of each group. Considering the corresponding cells volumes weighted with the corresponding probability value (see Eq. 5.2), the estimated volumes of groups 1-4 are respectively: 3.66×10^3 m^3, 1.81×10^4 m^3, 1.653×10^5 m^3 and 48×10^3 m^3. Note that these volumes exclude the cells of the inverted models where the sensitivity is less than 10- 5.5 and take into account the probability values, resulting in a total heap's volume of 235×10^3 m^3.

The volume of Group 1 represents the minority of the heap and it is mostly composed of Si, Ti and K (largely construction and demolition residues). The material of Group 2 is mostly concentrated on the east of the heap and scattered deposits distributed westwards. The material in this category presents the largest concentrations of Mn, Fe, V and Cr and it represents the most interesting volume for potential recovery. Then, the volume of Group 3 represents most of the slag heap material and it is distributed along the whole heap. Lastly, the intermediate volume of Group 4 is concentrated in the east of the heap and has scattered deposits westwards of the heap. As mentioned before, Groups 3 and 4 present very similar geophysical and geochemical properties, yet the chargeability measured in samples of Group 4 are slightly larger than the ones in Group 3. Furthermore, the elements of Group 4 present in general, a larger concentration of Mn and possibly a larger concentration of quicklime (due to the strong correlation Mn-Ca). Due to the relatively low iron concentration in groups 3 and 4, these volumes can be potentially reused for road construction.

5.5 Discussion

The integrated approach we followed seems suitable to quantitatively interpret geophysical field data using a probabilistic classification, according to a physics-based clustering from lab data. In the following, we describe the findings and limitations of the elements of this methodology.

First, geoelectric methods have proved useful to derive insights into the composition of metallurgical deposits, even in intermediate-to-low concentrations of metals. As in practice field acquisitions are tailored to be cost and time-efficient, ERT and time-domain IP represent suitable methods to be used in the field for a “rapid” investigation of metallurgical deposits (Martínez et al., 2019; Rey et al., 2020; Vásconez-Maza et al., 2021), in comparison with SIP field measurements which are still challenging.

Second, the targeted sampling was designed to cover most of the lateral and vertical (shallow) variations of the inverted models. Therefore, here we assume that the 22 samples collected at different positions (x, y, z) represent ground truth data enough to capture the physical and chemical properties of the slag heap overall. Note that in the literature we can find sampling to be challenging and often samples are collected at surface, at several sites and/or at few locations (x, y) (Florsch et al., 2011; Inzoli et al., 2016; Martin et al., 2021).

Both geophysical laboratory measurements and geochemical analysis could show

a variation in the composition of slags in the samples. Overall, resistivity measurements were useful to identify different types of materials (slags and crushed bricks) and chargeability measurements could additionally resolve between different types of slags. SIP measurements support these findings with a varying phase magnitude as indicator of different types of slags, which is not observed in the residues with crushed bricks.

Regarding the multivariate statistical analysis, first, we distinguished chemical elements of interest and inferred the composition of different types of slags through the correlation study of the elements' concentrations. Then, in the correlation study between geochemical and geophysical variables we identified the geophysical parameters that resolved variations of the chemical elements. We observed a linear relation between m_{lab} and the concentrations of Fe, Mn, V and Cr - similar as in Florsch et al. (2011)- and also strong correlations between ρ_{lab} and Si, K and Ti.

In terms of SIP parameters, the amplitude of the phase at the frequency peak $|\phi_{peak}|$ also presented a strong correlation with the Fe, Mn, V and Cr content. In the correlation matrix we also included the field measurements of resistivity and chargeability. While the resistivity values presented strong correlations with Si, Ca and Ti (as observed for the laboratory measurements) the chargeability was corelated only with vanadium. Furthermore, the correlations of ρ_{lab} - ρ and $m_{lab} - m$ showed the scale difference derived from the comparison between "punctual" measurements directly from the samples and co-located volume-averaged data from inverted models. Although the correlation coefficients are relatively large ($\approx$0.7) and the field data may capture the variations observed in the laboratory measurements, the regularization effect of the inversion should still be considered. The aim of the methodology at this step was to derive and support a physical-chemical-based clustering using the laboratory measurements. The identification of 4 groups was mostly based on different resistivity and chargeability ranges as well as the concentration of Fe, Mn and Si (Figure 5.11a-c). A geophysics-based clustering leads to the same grouping as the geochemical-based one. This was supported first, with the complex conductivity at the relaxation frequency (i.e., different groups are associated with different phases, see Figure 5.11d-e), a hierarchical clustering and PCA, where the groups are clearly distinguished in the PC2-PC1 space.

Then, we modeled the 2D KDE's using the volume-averaged field data collocated with the sampling for each lab-based group previously identified. Afterwards we estimated the KDE's at the whole domain of the inverted field data and computed joint conditional probabilities. The classification of the field data is strongly influenced by the selection of the bandwidth h in the definition of the KDE's. Yet, we observed

that the two-step estimation of h represents a suitable alternative in presence of few data, i.e., the Scott's rule performs an automatic bandwidth estimation which can be tunned according to the level of noise we want to integrate in the model (which can be based on prior information). Furthermore, this selection of bandwidth also ensures that the classification of the data keeps the proportion of the prior probabilities established from the sampling. Lastly, the computation of joint conditional probabilities allowed to derive the uncertainty of the classification, which is of interest as for reserve classification.

Finally, the total volume estimated here is likely to represent a minimum threshold value. First, because the inverted models do not show the boundary between the slags and the host geology, whose natural level has been reported at around 115 m (but which could be deeper if natural soil was removed before the deposition of the slags). Secondly, we included only the areas of the inverted models with a sensitivity larger than $10^{-5.5}$. Nonetheless, the calculated volumes integrate the uncertainty of the classification, which can lead to more accurate quantifications to support remediation strategies especially in terms of resource recovery.

5.6 Conclusion

In this contribution we present an integrated approach to quantitatively interpret geophysical field data in terms of chemical composition using a probabilistic classification. It ultimately allows to estimate the volumes of each class considering only parts of the inverted models that are sufficiently reliable (trough sensitivity) and integrating the uncertainty of the classification. We illustrate this approach investigating a slag heap with residues from steel works and blast furnaces. Based on the statistical analysis of the geochemical and geophysical lab data, we identified 4 classes or groups from the 22 samples collected at different positions of the heap. Group 1 corresponds to the inert waste with the largest concentration of Si, Ti and K; Group 2 represents the slags with the largest concentrations of Fe, Mn, Cr and V, which in turn represents the most interesting volume in terms of recovery; Group 3 and 4 refer to the materials with an intermediate Fe-Mn concentrations but the materials of Group 4 present a range of larger resistivities, which could be an indicator of a different type of slag. Overall, we observe that defining elements of this methodology are: 1) a representative targeted sampling based on the results of the geophysical survey, to better infer prior probabilities and 2) the bandwidth selection for the definition of the KDE's, where the examination of the geophysical volume-averaged field data distribution is considered. Lastly, the integrated methodology can be adapted according to the feature to investigate at the field scale. Thus, laboratory measurements can include

mineralogical analysis to interpret the field data in terms of mineral composition, or pedological descriptions, borehole-logs, back-scattered images, etc.

5.7 Data and materials availability

Codes and data necessary to reproduce the results presented here, from statistical tools to the 3D probabilistic classification will be available once accepted for publication in: zenodo/

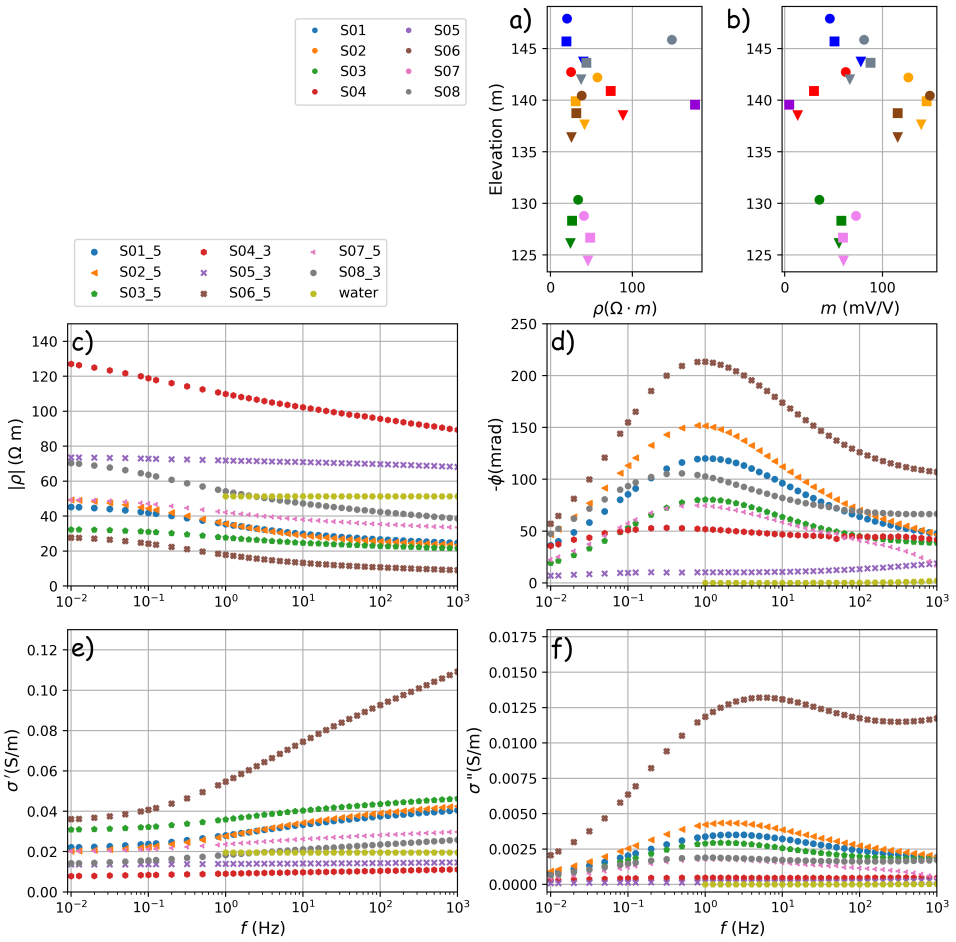

FIGURE 5.7: Geophysical lab measurement of ERT, IP and SIP. First, we present the measurements of a) resistivity and b) chargeability. Each sample is plotted with their corresponding sampling depths at 1, 3 and 5 m, which are represented with a circle, square and triangle respectively. Then, an overview of SIP spectra is presented for some samples and a column filled with water. For clarity we only plot the spectra of eight samples, each at one location (x, y) and different depths. The image presents the c) magnitude of resistivity, d) phase, e) real component of complex conductivity and f) imaginary component of the complex conductivity.

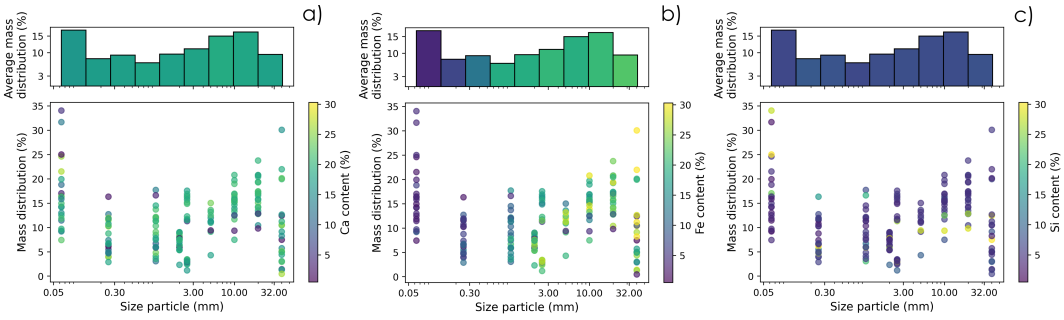

FIGURE 5.8: Particle size distribution and percentage mass distribution for all samples. Each colorbar displays a) the calcium content, b) iron content and c) silicon content.

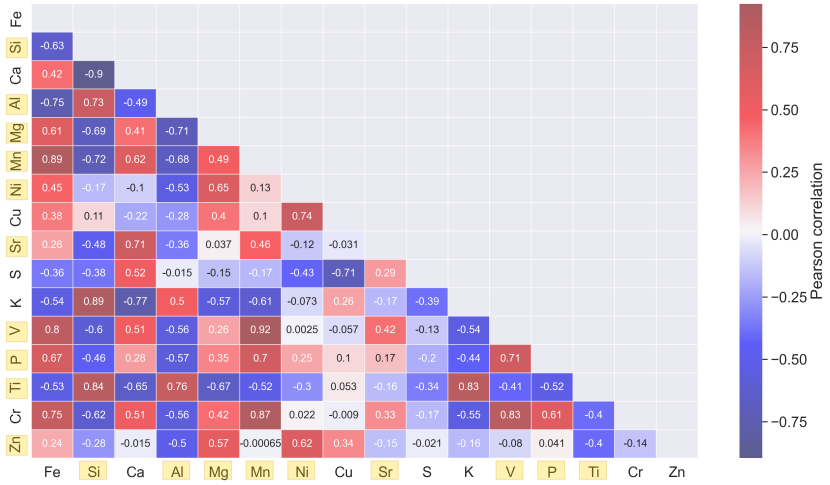

FIGURE 5.9: Particle size distribution and percentage mass distribution for all samples. Each colorbar displays a) the calcium content, b) iron content and c) silicon content.

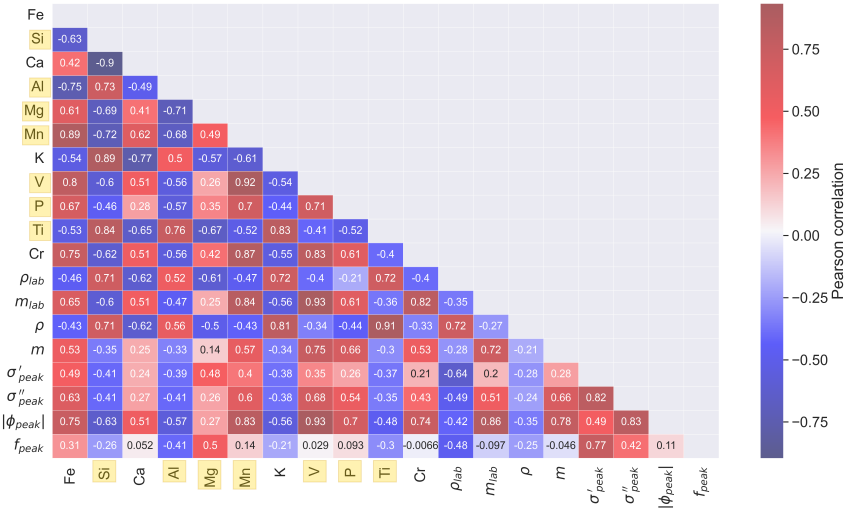

FIGURE 5.10: Matrix of Pearson's correlation coefficients using some geochemical variables and geophysical variables. Yellow squares indicate the critical raw materials of the EU 2023.

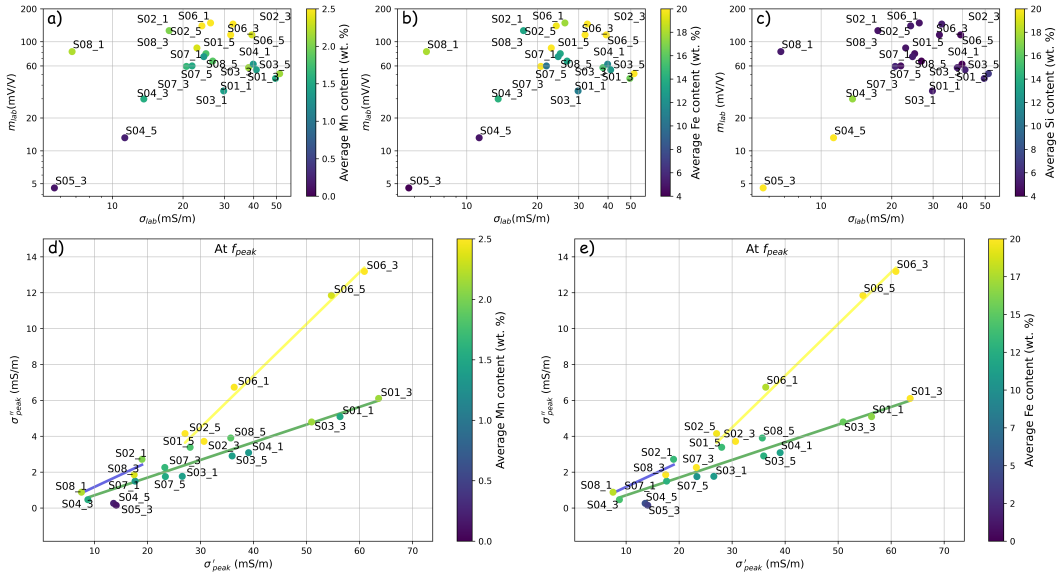

FIGURE 5.11: Crossplots of the time-domain laboratory measurements of ERT- IP and complex conductivity at the frequency peak. (a-c) Chargeability vs conductivity ($1/\rho_{lab}$) with colorbars representing the average content of a) Mn, b) Fe and c) Si. (d-e) Real vs imaginary component of the conductivity with colorbars representing the average content of d) Mn and e) Fe. Lines represent the linear regressions with samples of Group 2 (yellow), Group 3 (green) and Group 4 in blue.

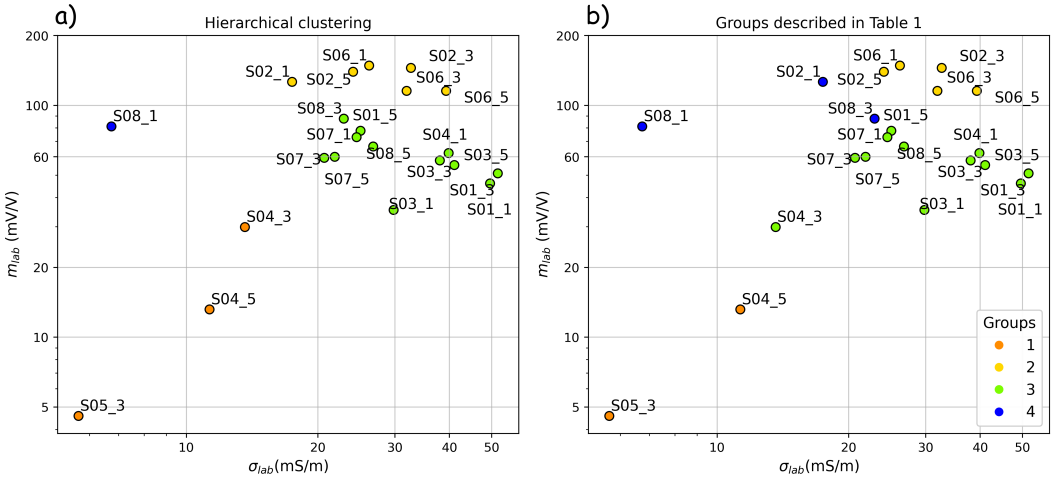

FIGURE 5.12: Groups identified using a) unsupervised clustering and b) lab measurements according to Table 5.1.

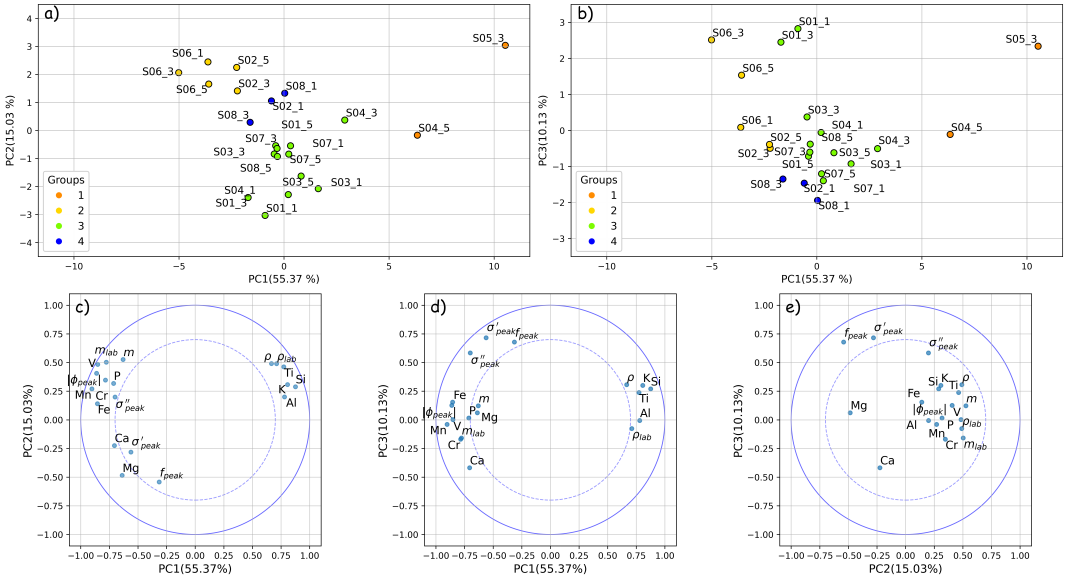

FIGURE 5.13: (a-b) Samples represented in the axis of principal components: a) PC2 vs PC1 and b) PC3 vs PC1. (c-e) Correlation coefficients between the variables and c) PC2 vs PC1, d) PC3 vs PC1 and e) PC3 vs PC2. The radii of the circles represent a correlation coefficient of 0.7 and 1.

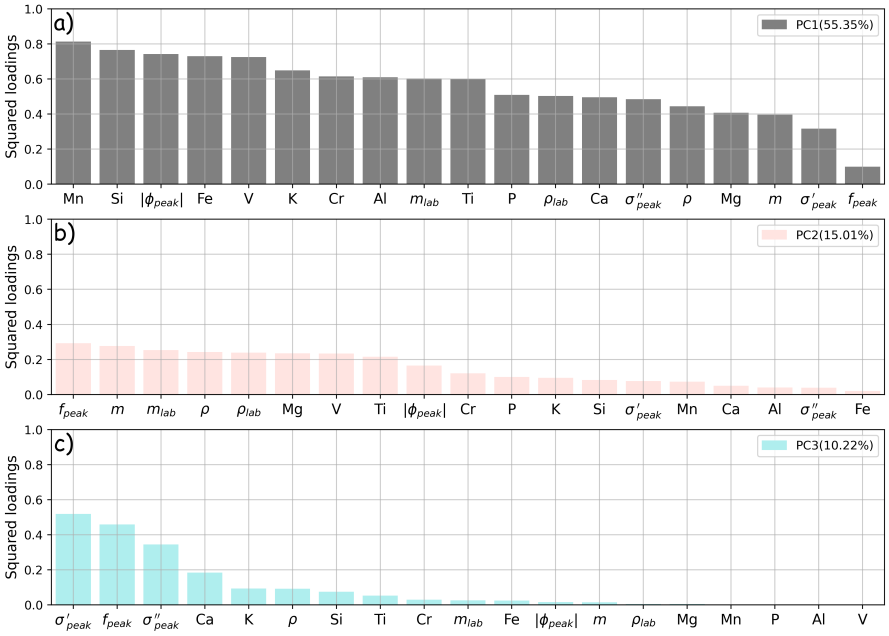

FIGURE 5.14: Squared loadings for a) PC1, b) PC2, and c) PC3. Variables are presented in decreasing values.

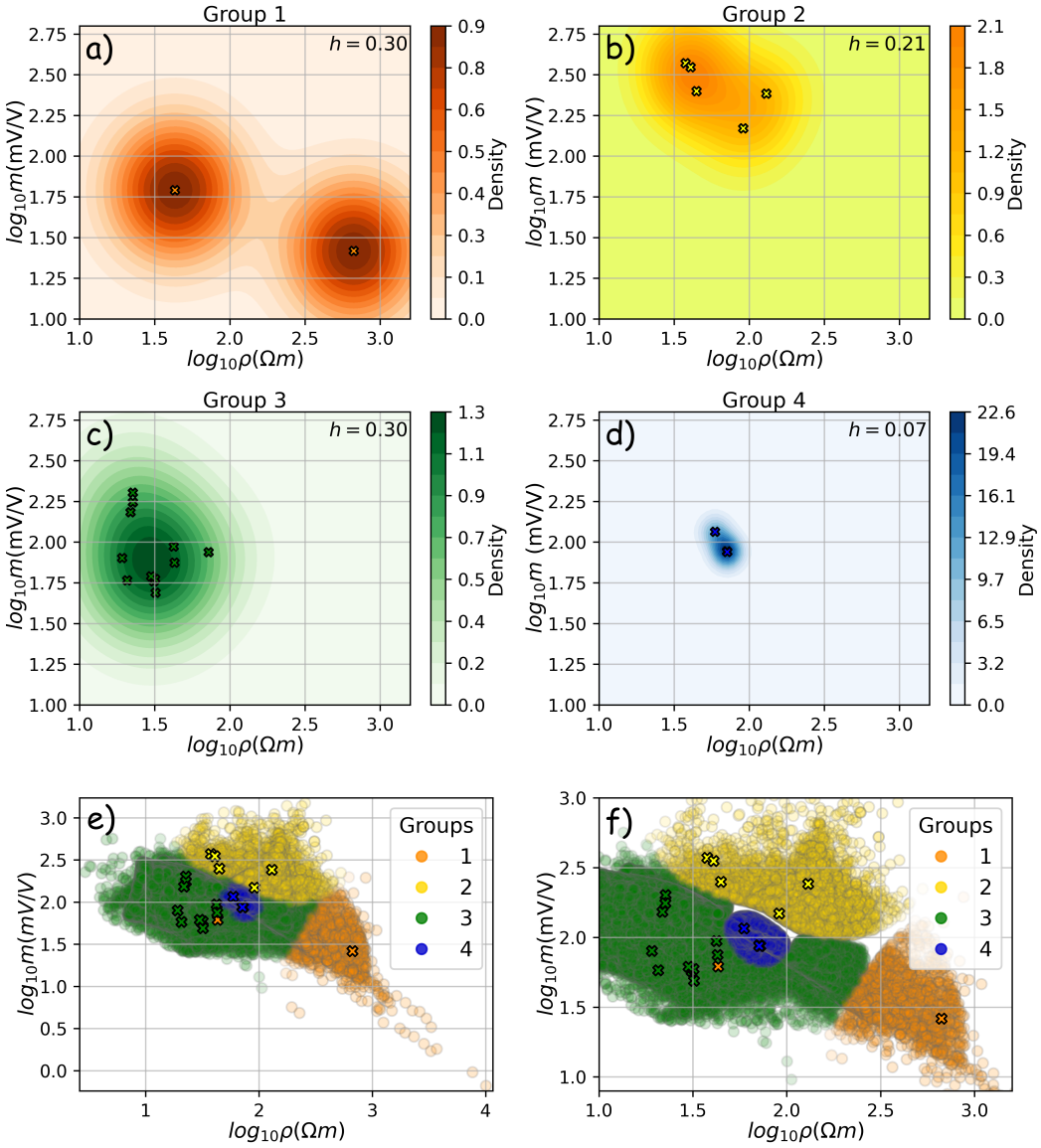

FIGURE 5.15: (a-d) Joint probability density function using 2D KDE in a regular grid together with the volume-averaged field data collocated with the sampling for each group. (e-f) Classification of the field data. The lab measurements are displayed with crosses as well as their corresponding group color. The minimum joint probability is e) 33 % (maximum transparency). We also show in f) the classification considering only joint probability values larger than 50 %, with a special effect in boundaries of groups 2-4 and 1-2.

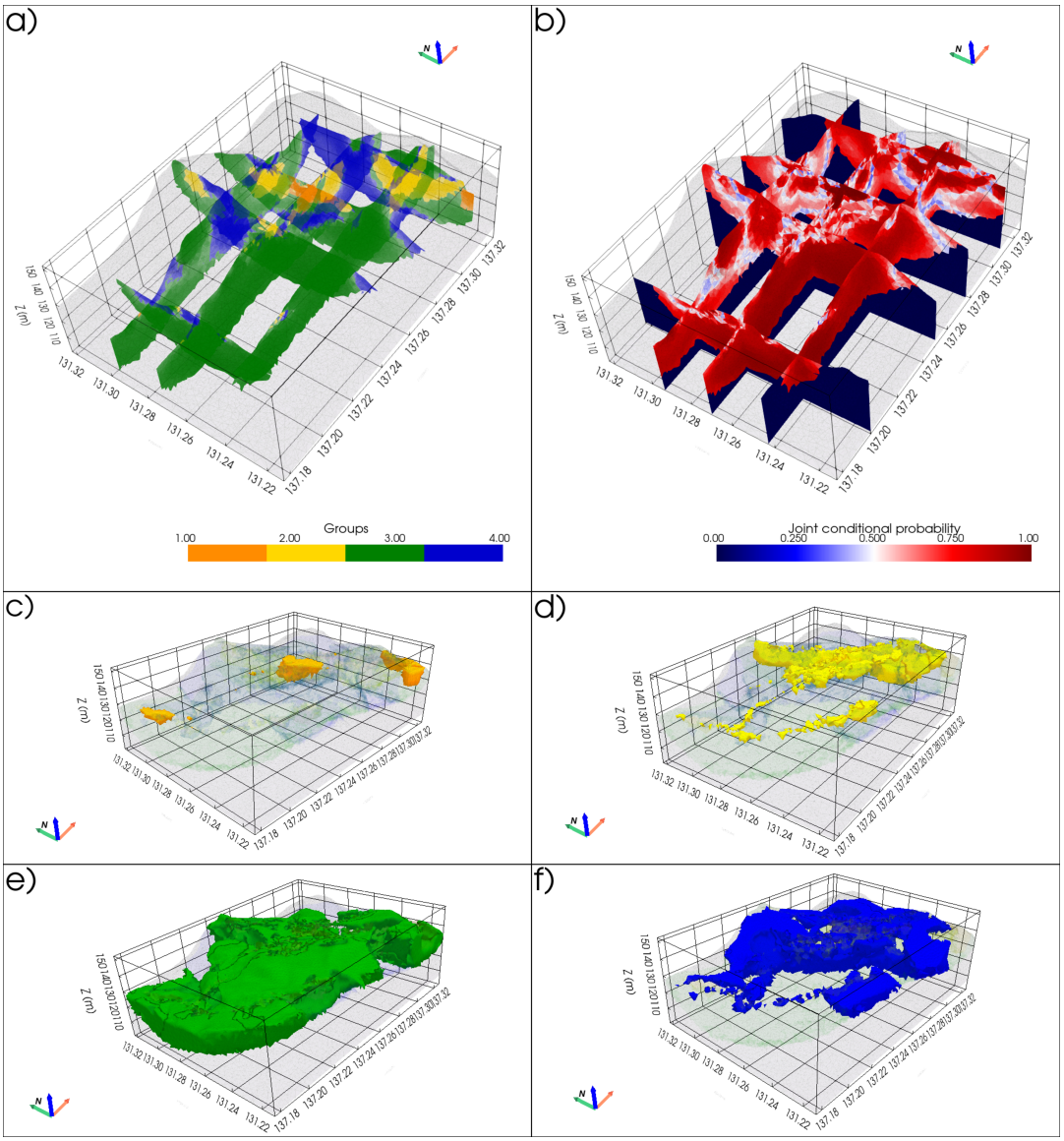

FIGURE 5.16: a) Classification of the field data. Transparency along the sections represent the resulting probability values. b) Joint conditional probability sections. Both images integrate the sensitivity threshold (>10-5.5). We also show the estimated volumes of c) group 1, d) group 2, e) group 3 and f) group 4.

Chapter 6

General conclusions and perspectives

The aim of this work was to contribute to the development of more quantitative interpretations of geophysical data applied in the characterization of anthropogenic deposits. The first part was more focused in different types of landfills within the framework of RAWFILL project, while the second part of this work is focused on metallurgical residues and deposits as part of NWE-REGENERATIS.

Based on the literature review presented in Chapter 3 and on the investigated sites during RAWFILL, we observed that the quantitative interpretation of several geophysical methods could be challenging due to factors such as the infrastructure of the landfill, the vegetation state and topography.

In general, the following conclusions can be stated with regards to the data acquisition and processing stages:

- Magnetometry and electromagnetic induction methods can be strongly affected by the metallic scraps that are often deposited in the surface of landfills. In addition, magnetic susceptibility modeling and the data inversion of both methods may be challenging in these environments.
- Seismic methods can be useful to roughly delineate the thickness of the waste deposits. Detailed investigations to image small internal structures or processes within the waste, may require more advanced data acquisition and processing, e.g., Konstantaki et al., 2016. Nonetheless, buried refractors such as concrete blocks and other types of CDW can limit the data acquisition and subsequent processing.
- Geoelectric methods can be applied under several contexts except for landfills with an upper plastic geomembrane that impedes the electrical current injection (where electromagnetic induction mapping is often used, e.g., Deidda et al. 2022, Deleersnyder et al. 2023). These methods have been largely used

in the static and dynamic characterization of landfills, e.g., leachate and gas delineation, zonation and internal structure.

In terms of data interpretation, one essential step for the calibration (and also to rely on more sophisticated machine learning approaches) is to have ground truth data from excavations of boreholes or pits. Nonetheless, in practice:

- Excavations can be limited to mitigate costs and human/environmental risks.
- It is important to carry out data interpretations with information that can be used as decision support tools in the sustainable management of the site.

The above-mentioned statements were the motivation of the work presented in Chapter 4, where we introduced a probabilistic approach for the interpretation of geoelectric data in a heterogeneous landfill. The probabilistic approach represent a suitable tool to derive quantitative interpretations through a classification based on the computation of joint conditional probabilities, given the categories or materials found in trial pits. Consequently, it allows to integrate the uncertainty in the classification or the prediction results. As illustrated with a case study, this approach is recommended in cases where the inverted models may present sharp heterogeneties and/or artifacts, and when the accessible ground truth data is limited and sparsely distributed.

The sites investigated during NWE-REGENERATIS were composed of metallurgical residues from by-products of different types of industries. Compared to the landfills investigated in RAWFILL, the deposits of each site are relatively more homogeneous and in general derived from the same processes. Although the conclusions previously mentioned are also valid in these sites, more detailed investigations are needed to derive interpretations or resource distribution models in terms of chemical composition and not only in terms of materials. Therefore, the collection of samples (ideally at different depths) and laboratory measurements are needed to calibrate geophysical data with geochemical data.

With this regard, Chapter 5 described an integrated methodology that aims to calibrate geochemical and geophysical data at lab scale, and extrapolate this link to the geophysical field data. We illustrated the methodology using ERT and IP to investigate a slag heap with materials derived from steel works and blast furnaces. At lab scale we used also ERT, IP and in addition SIP. Similarly to Chapter 4 the interpretation was based on a probabilistic classification, but in this case, we used 2D KDE's as density functions and the categories were defined using a geophysical-geochemical based grouping of the lab data. This methodology illustrates how we can integrate lab and field measurements to develop a probabilistic classification in terms of the

chemical composition of the materials, with the ultimate objective of their volume estimation. This approach, which considers only zones of the inverted models reliable enough, allows to integrate uncertainty in the classification (interpretation) and consequently in the estimation of volumes.

6.1 Perspectives

The method of induced polarization represents a promising tool to characterize several types of landfills and metallurgical residues for static investigations and the study of dynamic processes within the residues.

- As indicated by Flores-Orozco et al. (2020), the method is suitable to image biogeochemical active zones (and hence it can be used as indicator of microbiological activity), since the polarization effect can resolve organic matter variations.
- It has proved useful for the characterization of metallurgical residues due to the strong polarization that metallic particles experience under the influence of an electric field. As has been shown through petrophysical modeling and experimental data, there is a linear relationship between the observed chargeability and both the volume fraction of metallic particles as well as the chargeability of the background material. Hence the ability of the method to infer on the concentration of metallic minerals in unconsolidated materials (Revil et al., 2022).
- In addition, IP has also proven useful in applications studying the dynamic behavior of metallurgical residues, although mostly at laboratory scale. An important extension of the presented work is to investigate how the polarization signal of metallurgical residues is affected under different levels of water content/saturation, e.g., Martin et al. (2022). Furthermore, it has been suggested that oxidation-reduction reactions and precipitation-adsorption of secondary minerals can modify the surface of the investigated metallic particles, which in turn change the IP signatures (Placencia-Gómez et al., 2015). A better knowledge of the dynamic processes within these residues can lead to a more accurate identification and quantification of metallic materials using geoelectric methods.

Lastly, the probabilistic approach of Chapter 4 and the methodology presented in Chapter 5 can be extended to multiple data sources and can be used for field data

interpretation in 3D. Furthermore, the definition of classes or categories can be tailored to investigate parameters of interest which have been measured in situ (through boreholes) or in the lab (after the collection of samples) such as water content and mineralogical composition. In the case presented in Chapter 5 we interpret field data based on XRF analysis, but if more detailed lab studies are carried out, for instance mineralogical analysis, the final interpretation could potentially be done in terms of types of minerals forms. This may represent meaningful information for the site management. Oppositely, when excavations or ground truth data are limited in depth (compared to the thickness of the landfill or deposit), the interpretation in these zones have to be inferred.

Bibliography

Abdulrahman, Abdullahi, Mohd Nawawi, Rosli Saad, Asad Siraj Abu-Rizaiza, Mohd Suffian Yusoff, Amin Esmail Khalil, and Kehinde Saheed Ishola (2016). "Characterization of active and closed landfill sites using 2D resistivity/IP imaging: case studies in Penang, Malaysia". In: *Environmental Earth Sciences* 75, pp. 1–17.

Abreu, AES, OCB Gandolfo, and Orêncio Monje Vilar (2016). "Characterizing a Brazilian sanitary landfill using geophysical seismic techniques". In: *Waste Management* 53, pp. 116–127.

Alam, Md Iftekhar, Andrew Katumwehe, Khumo Leseane, Fathiya Al-Hadhrami, Brooke Briand, Daniel Morse, Sam Wei, and Estella Atekwana (2018). "Imaging landfill leachate plume boundaries using electrical-resistivity inversion, spontaneous potential, EM 34 and Geochemical Analysis: A case study on Norman Landfill". In: *SEG International Exposition and Annual Meeting*. SEG, SEG–2018.

Archie, Gustave E (1942). "The electrical resistivity log as an aid in determining some reservoir characteristics". In: *Transactions of the AIME* 146.01, pp. 54–62.

Asare, Michael Opare and Jerry Owusu Afriyie (2021). "Ancient mining and metallurgy as the origin of Cu, Ag, Pb, Hg, and Zn contamination in soils: a review". In: *Water, Air, & Soil Pollution* 232.6, p. 240.

Aster, Richard C, Brian Borchers, and Clifford H Thurber (2018). *Parameter estimation and inverse problems*. Elsevier.

Aszemi, Nurshazlyn Mohd and PDD Dominic (2019). "Hyperparameter optimization in convolutional neural network using genetic algorithms". In: *International Journal of Advanced Computer Science and Applications* 10.6.

Audebert, Marine, Rémi Clément, N Touze-Foltz, T Günther, S Moreau, and C Duquennoi (2014). "Time-lapse ERT interpretation methodology for leachate injection monitoring based on multiple inversions and a clustering strategy (MICS)". In: *Journal of Applied Geophysics* 111, pp. 320–333.

Baasch, Benjamin, Hendrik Müller, and Tilo von Dobeneck (2018). "Predictive modelling of grain-size distributions from marine electromagnetic profiling data using end-member analysis and a radial basis function network". In: *Geophysical Journal International* 214.1, pp. 460–473.

Baawain, Mahad S, Ahmed M Al-Futaisi, A Ebrahimi, and Hamid Omidvarborna (2018). "Characterizing leachate contamination in a landfill site using Time Domain Electromagnetic (TDEM) imaging". In: *Journal of Applied Geophysics* 151, pp. 73–81.

Balbarini, Nicola, Vinni Rønde, Pradip Maurya, Gianluca Fiandaca, Ingelise Møller, Knud Erik Klint, Anders V Christiansen, Philip J Binning, and Poul L Bjerg (2018). "Geophysics-based contaminant mass discharge quantification downgradient of a landfill and a former pharmaceutical factory". In: *Water Resources Research* 54.8, pp. 5436–5456.

Balia, Roberto et al. (2018). "Old municipal and industrial waste landfills: some examples of possible contribution of geophysical survey techniques for their assessment before reclamation". In: *Detritus* 1, pp. 110–115.

Beaujean, Jean, Frédéric Nguyen, A Kemna, A Antonsson, and P Engesgaard (2014). "Calibration of seawater intrusion models: Inverse parameter estimation using surface electrical resistivity tomography and borehole data". In: *Water Resources Research* 50.8, pp. 6828–6849.

Benoit, Sien, Gert Ghysels, Kevin Gommers, Thomas Hermans, Frederic Nguyen, and Marijke Huysmans (2019). "Characterization of spatially variable riverbed hydraulic conductivity using electrical resistivity tomography and induced polarization". In: *Hydrogeology journal* 27.1.

Bhattacharya, P (2012). "Direct current geoelectric sounding: Principles and interpretation". In.

Binley, Andrew and Andreas Kemna (2005). "DC resistivity and induced polarization methods". In: *Hydrogeophysics*, pp. 129–156.

Binley, Andrew and Lee Slater (2020). *Resistivity and induced polarization: Theory and applications to the near-surface earth*. Cambridge University Press.

Bobe, Christin, Ellen Van De Vijver, Johannes Keller, Daan Hanssens, Marc Van Meirvenne, and Philippe De Smedt (2020). "Probabilistic 1-D inversion of frequency-domain electromagnetic data using a Kalman ensemble generator". In: *IEEE Transactions on Geoscience and Remote Sensing* 58.5, pp. 3287–3297.

Bortnikova, Svetlana Borisovna, Vladimir Vladimirovich Olenchenko, Olga Lukinichna Gaskova, Konstantin Ivanovich Chernii, Anna Yurevna Devyatova, and Dmitrii Olegovich Kucher (2017). "Evidence of trace element emission during the combustion of sulfide-bearing metallurgical slags". In: *Applied geochemistry* 78, pp. 105–115.

Brenguier, Florent, Aurélien Mordret, Richard Lynch, Roméo Courbis, Xander Campbell, Pierre Boué, Malgorzata Chmiel, Shujuan Mao, Shujuan Mao, Tomoya Takano, et al. (2019). "Monitoring of fields using body and surface waves reconstructed

from passive seismic ambient noise". In: *SEG International Exposition and Annual Meeting*. SEG, D043S104R007.

Bücker, Matthias Benedikt (2019). "Pore-Scale Modelling of Induced-Polarization Mechanisms in Geologic Materials". PhD thesis. Universitäts-und Landesbibliothek Bonn.

Butler, Dwain K (2005). *Near-surface geophysics*. Society of Exploration Geophysicists.

Campbell, RB, CA Bower, and LA Richards (1949). "Change of electrical conductivity with temperature and the relation of osmotic pressure to electrical conductivity and ion concentration for soil extracts". In: *Soil Science Society of America Journal* 13.C, pp. 66–69.

Canters, Frank (1997). "Evaluating the uncertainty of area estimates derived from fuuy land-cover classification". In: *Photogramm. Eng. Remote Sens* 63.4, pp. 403–414.

Carpenter, Philip J and Krishna R Reddy (2016). "Ground-Penetrating Radar (GPR) surveys and geophysical well logs at a leachate-recirculation landfill, Northern Illinois". In: *Geo-Chicago 2016*, pp. 150–161.

Carpenter, Philip J, Krishna R Reddy, and Michael D Thompson (2013). "Dynamic properties of municipal solid waste in a bioreactor cell at orchard hills landfill, Illinois, USA". In: *7th International Conference on Case Histories in Geotechnical Engineering*.

Cartwright, Keros and Murray R McComas (1968). "Geophysical Surveys in the Vicinity of Sanitary Landfills in Northeastern Illinois a". In: *Groundwater* 6.5, pp. 23–30.

Caterina, David, Jean Beaujean, Tanguy Robert, and Frédéric Nguyen (2013). "A comparison study of different image appraisal tools for electrical resistivity tomography". In: *Near Surface Geophysics* 11.6, pp. 639–658.

Caterina, David, Thomas Hermans, and Frédéric Nguyen (2014). "Case studies of incorporation of prior information in electrical resistivity tomography: comparison of different approaches". In: *Near Surface Geophysics* 12.4, pp. 451–465.

Caterina, David, Itzel Isunza Manrique, Cornelia Inauen, Arnaud Watlet, Ben Dashwood, Renaud De Rijdt, Gaël Dumont, Jonathan Chambers, and Frédéric Nguyen (2019). "Contribution of geophysical methods to the study of old landfills: A case study in Onoz (Belgium)". In: *17th International waste management and landfill symposium*.

Cavalcante Fraga, Luis H, Cyril Schamper, Cécile Noël, Roger Guérin, and Fayçal Rejiba (2019). "Geometrical characterization of urban fill by integrating the multi-receiver electromagnetic induction method and electrical resistivity tomography:

A case study in Poitiers, France". In: *European Journal of Soil Science* 70.5, pp. 1012–1024.

Chambers, Jonathan E, Oliver Kuras, Philip I Meldrum, Richard D Ogilvy, and Jonathan Hollands (2006). "Electrical resistivity tomography applied to geologic, hydrogeologic, and engineering investigations at a former waste-disposal site". In: *Geophysics* 71.6, B231–B239.

Chasseriau, Pierrick and Michel Chouteau (2003). "3D gravity inversion using a model of parameter covariance". In: *Journal of applied geophysics* 52.1, pp. 59–74.

Choudhury, Deepankar and Purnanand Savoikar (2009). "Simplified method to characterize municipal solid waste properties under seismic conditions". In: *Waste management* 29.2, pp. 924–933.

Clement, Remi, Marine Audebert, Simon Loisel, and Sylvain Moreau (2018). "Straightforward assessment of horizontal leachate injection system using frequency domain electromagnetic induction method". In: *Environmental Research and Technology* 1.2, pp. 13–17.

Cole, Kenneth S and Robert H Cole (1941). "Dispersion and absorption in dielectrics I. Alternating current characteristics". In: *The Journal of chemical physics* 9.4, pp. 341–351.

Conrad, Schlumberger (1939). *Method and apparatus for identifying the nature of the formations in a bore hole*. US Patent 2,165,013.

Cortizas, Antonio Martínez, Lourdes López-Merino, Richard Bindler, Tim Mighall, and Malin E Kylander (2016). "Early atmospheric metal pollution provides evidence for Chalcolithic/Bronze Age mining and metallurgy in Southwestern Europe". In: *Science of the Total Environment* 545, pp. 398–406.

Costa, Alyne Moraes, Raquel Greice de Souza Marotta Alfaia, and Juacyara Carbonelli Campos (2019). "Landfill leachate treatment in Brazil–An overview". In: *Journal of environmental management* 232, pp. 110–116.

Costall, AR, BD Harris, B Teo, R Schaa, FM Wagner, and JP Pigois (2020). "Groundwater throughflow and seawater intrusion in high quality coastal aquifers". In: *Scientific reports* 10.1, pp. 1–33.

Cracknell, Matthew J and Anya M Reading (2014). "Geological mapping using remote sensing data: A comparison of five machine learning algorithms, their response to variations in the spatial distribution of training data and the use of explicit spatial information". In: *Computers & Geosciences* 63, pp. 22–33.

Czepiel, Peter, Ellen Douglas, Robert Harriss, and Patrick Crill (1996). "Measurements of N2O from composted organic wastes". In: *Environmental Science & Technology* 30.8, pp. 2519–2525.

Dahlin, Torleif, Virginie Leroux, and Johan Nissen (2002). "Measuring techniques in induced polarisation imaging". In: *Journal of Applied Geophysics* 50.3, pp. 279–298.

Dahlin, Torleif and Bing Zhou (2004). "A numerical comparison of 2D resistivity imaging with 10 electrode arrays". In: *Geophysical prospecting* 52.5, pp. 379–398.

— (2006). "Multiple-gradient array measurements for multichannel 2D resistivity imaging". In: *Near Surface Geophysics* 4.2, pp. 113–123.

De Pasquale, Giulia, Niklas Linde, Joseph Doetsch, and W Steven Holbrook (2019). "Probabilistic inference of subsurface heterogeneity and interface geometry using geophysical data". In: *Geophysical Journal International* 217.2, pp. 816–831.

Deidda, Gian Piero, Mahjoub Himi, Ilaria Barone, Giorgio Cassiani, and Albert Casas Ponsati (2022). "Frequency-domain electromagnetic mapping of an abandoned waste disposal site: A case in Sardinia (Italy)". In: *Remote Sensing* 14.4, p. 878.

Deleersnyder, Wouter, Abdoulie Bah, Guillaume Blanchy, Thomas Hermans, and Ellen Van De Vijver (2023). "Estimating the Volume of Recoverable Materials from a Former Gypsum Landfill Using Frequency-Domain Electromagnetics". In: *NSG2023 29th European Meeting of Environmental and Engineering Geophysics*. Vol. 2023. 1. European Association of Geoscientists & Engineers, pp. 1–5.

Delforge, Damien, Arnaud Watlet, Olivier Kaufmann, Michel Van Camp, and Marnik Vanclooster (2021). "Time-series clustering approaches for subsurface zonation and hydrofacies detection using a real time-lapse electrical resistivity dataset". In: *Journal of Applied Geophysics* 184, p. 104203.

Dewar, Noah and Rosemary Knight (2020). "Estimation of the top of the saturated zone from airborne electromagnetic data". In: *Geophysics* 85.5, EN63–EN76.

Dino, Giovanna Antonella, Alessandro Cavallo, Alessandra Faraudello, Rossi Piercarlo, and Susanna Mancini (2021). "Raw materials supply: Kaolin and quartz from ore deposits and recycling activities. The example of the Monte Bracco area (Piedmont, Northern Italy)". In: *Resources Policy* 74, p. 102413.

Dramsch, Jesper Sören (2020). "70 years of machine learning in geoscience in review". In: *Advances in geophysics* 61, pp. 1–55.

Dumont, Gaël, Tamara Pilawski, Phidias Dzaomuho-Lenieregue, Serge Hiligsmann, Frank Delvigne, Philippe Thonart, Tanguy Robert, Frédéric Nguyen, and Thomas Hermans (2016). "Gravimetric water distribution assessment from geoelectrical methods (ERT and EMI) in municipal solid waste landfill". In: *Waste management* 55, pp. 129–140.

Dumont, Gaël, Tanguy Robert, Nicolas Marck, and Frédéric Nguyen (2017). "Assessment of multiple geophysical techniques for the characterization of municipal waste deposit sites". In: *Journal of Applied Geophysics* 145, pp. 74–83.

Dumont, Gaël, Tanguy Robert, and Frédéric Nguyen (2018). "Electrical resistivity tomography and distributed temperature sensing monitoring to assess the efficiency of horizontal recirculation drains on retrofit bioreactor landfills". In: *Geophysics* 83.2, B13–B23.

Elis, Vagner Roberto, Andrea Teixeira Ustra, Marlon Cabrera Hidalgo-Gato, Osni José Pejon, and Francisco Yukio Hiodo (2016). "Application of induced polarization and resistivity to the environmental investigation of an old waste disposal area". In: *Environmental Earth Sciences* 75, pp. 1–13.

Epov, MI, NV Yurkevich, SB Bortnikova, Yu G Karin, and OP Saeva (2017). "Analysis of mine waste by geocheimical and geophysical methods (a case study of the mine tailing dump of the Salair ore-processing plant)". In: *Russian Geology and Geophysics* 58.12, pp. 1543–1552.

Feng, Shi-Jin, Zhen-Bai Bai, Ben-Yi Cao, Shi-Feng Lu, and Shu-Gang Ai (2017a). "The use of electrical resistivity tomography and borehole to characterize leachate distribution in Laogang landfill, China". In: *Environmental Science and Pollution Research* 24, pp. 20811–20817.

Feng, Shi-Jin, Shi-Feng Lu, HX Chen, Wen-Ding Fu, and Fan Lü (2017b). "Three-dimensional modelling of coupled leachate and gas flow in bioreactor landfills". In: *Computers and Geotechnics* 84, pp. 138–151.

Feng, Shi-Jin, Yong Zhao, Xiao-Lei Zhang, and Zhen-Bai Bai (2020). "Leachate leakage investigation, assessment and engineering countermeasures for tunneling underneath a MSW landfill". In: *Engineering Geology* 265, p. 105447.

Feng, Shi-Jin, Qi-Teng Zheng, and HX Chen (2017c). "Unsaturated flow parameters of municipal solid waste". In: *Waste Management* 63, pp. 107–121.

Fernandez, Perrine M, Andrew Binley, Esther Bloem, and Helen K French (2019). "Laboratory spectral induced polarisation signatures associated with iron and manganese oxide dissolution because of anaerobic degradation". In: *Journal of contaminant hydrology* 221, pp. 1–10.

Fiandaca, G, PK Maurya, Nicola Balbarini, A Hördt, AV Christiansen, N Foged, Poul Løgstrup Bjerg, and E Auken (2018). "Permeability estimation directly from logging-while-drilling induced polarization data". In: *Water Resources Research* 54.4, pp. 2851–2870.

Fiandaca, Gianluca, Esben Auken, Anders Vest Christiansen, and Aurélie Gazoty (2012). "Time-domain-induced polarization: Full-decay forward modeling and

1D laterally constrained inversion of Cole-Cole parameters". In: *Geophysics* 77.3, E213–E225.

Flores-Orozco, A, J Gallistl, M Steiner, C Brandstätter, and J Fellner (2020). "Mapping biogeochemically active zones in landfills with induced polarization imaging: The Heferlbach landfill". In: *Waste Management* 107, pp. 121–132.

Florsch, Nicolas, M Llubes, and F Téreygeol (2012). "Induced polarization 3D tomography of an archaeological direct reduction slag heap". In: *Near Surface Geophysics* 10.6, pp. 567–574.

Florsch, Nicolas, M Llubes, F Téreygeol, A Ghorbani, and P Roblet (2011). "Quantification of slag heap volumes and masses through the use of induced polarization: application to the Castel-Minier site". In: *Journal of Archaeological Science* 38.2, pp. 438–451.

Fossum, Kristian, Sergey Alyaev, Jan Tveranger, and Ahmed H Elsheikh (2022). "Verification of a real-time ensemble-based method for updating earth model based on GAN". In: *Journal of Computational Science* 65, p. 101876.

Frid, Vladimir, Dmitri Doudkinski, Gady Liskevich, Efim Shafran, Arie Averbakh, Nikolay Korostishevsky, and Larisa Prihodko (2010). "Geophysical-geochemical investigation of fire-prone landfills". In: *Environmental Earth Sciences* 60, pp. 787–798.

Frid, Vladimir, Itay Sharabi, Michael Frid, and Arie Averbakh (2017). "Leachate detection via statistical analysis of electrical resistivity and induced polarization data at a waste disposal site (Northern Israel)". In: *Environmental Earth Sciences* 76.6, p. 233.

Fu, Qi, Dan Niu, Zengliang Zang, Junhao Huang, and Li Diao (2019). "Multi-stations' weather prediction based on hybrid model using 1D CNN and Bi-LSTM". In: *2019 Chinese control conference (CCC)*. IEEE, pp. 3771–3775.

Gahegan, Mark (2000). "On the application of inductive machine learning tools to geographical analysis". In: *Geographical analysis* 32.2, pp. 113–139.

Gal, Yarin and Zoubin Ghahramani (2016). "Dropout as a bayesian approximation: Representing model uncertainty in deep learning". In: *international conference on machine learning*. PMLR, pp. 1050–1059.

Gazoty, Aurélie, Gianluca Fiandaca, J Pedersen, Esben Auken, and Anders Vest Christiansen (2012). "Mapping of landfills using time-domain spectral induced polarization data: the Eskelund case study". In: *Near Surface Geophysics* 10.6, pp. 575–586.

Georgaki, Irene, Pantelis Soupios, N Sakkas, F Ververidis, E Trantas, F Vallianatos, and T Manios (2008). "Evaluating the use of electrical resistivity imaging technique for improving CH4 and CO2 emission rate estimations in landfills". In: *Science of the total environment* 389.2-3, pp. 522–531.

Giang, NV, K Kochanek, NT Vu, and NB Duan (2018). "Landfill leachate assessment by hydrological and geophysical data: case study NamSon, Hanoi, Vietnam". In: *Journal of material cycles and waste management* 20, pp. 1648–1662.

Goodfellow, Ian, Yoshua Bengio, and Aaron Courville (2016). *Deep learning*. MIT press.

Grohol, M and C Veeh (2023). "Study on the Critical Raw Materials for the EU". In: *Final Report*.

Günther, Thomas, Carsten Rücker, and Klaus Spitzer (2006). "Three-dimensional modelling and inversion of DC resistivity data incorporating topography—II. Inversion". In: *Geophysical Journal International* 166.2, pp. 506–517.

Helene, Lívia Portes Innocenti and César Augusto Moreira (2021). "Analysis of leachate generation dynamics in a closed municipal solid waste landfill by means of geophysical data (DC resistivity and self-potential methods)". In: *Pure and Applied Geophysics* 178.4, pp. 1355–1367.

Hellman, Kristofer, Mathias Ronczka, Thomas Günther, Marcus Wennermark, Carsten Rücker, and Torleif Dahlin (2017). "Structurally coupled inversion of ERT and refraction seismic data combined with cluster-based model integration". In: *Journal of Applied Geophysics* 143, pp. 169–181.

Hellmann, Bettina, Laszlo Zelles, Ansa Palojarvi, and Quingyun Bai (1997). "Emission of climate-relevant trace gases and succession of microbial communities during open-windrow composting". In: *Applied and environmental microbiology* 63.3, pp. 1011–1018.

Hermans, Thomas and James Irving (2017). "Facies discrimination with electrical resistivity tomography using a probabilistic methodology: effect of sensitivity and regularisation". In: *Near Surface Geophysics* 15.1, pp. 13–25.

Hermans, Thomas, Frédéric Nguyen, and Jef Caers (2015). "Uncertainty in training image-based inversion of hydraulic head data constrained to ERT data: Workflow and case study". In: *Water Resources Research* 51.7, pp. 5332–5352.

Hermans, Thomas, Frédéric Nguyen, Tanguy Robert, and Andre Revil (2014). "Geophysical methods for monitoring temperature changes in shallow low enthalpy geothermal systems". In: *Energies* 7.7, pp. 5083–5118.

Hermans, Thomas, Alexander Vandenbohede, Luc Lebbe, and Frédéric Nguyen (2012). "A shallow geothermal experiment in a sandy aquifer monitored using electric resistivity tomography". In: *Geophysics* 77.1, B11–B21.

Hernández Parrodi, Juan Carlos, Cristina García López, Bastian Küppers, Karoline Raulf, Daniel Vollprecht, Thomas Pretz, Roland Pomberger, et al. (2019a). "Case study on enhanced landfill mining at Mont-Saint-Guibert landfill in Belgium: Characterization and potential of fine fractions". In: *Detritus* 8.December, pp. 47–61.

Hernández Parrodi, Juan Carlos, Hugo Lucas, Marco Gigantino, Giovanna Sauve, John L Esguerra, Paul Einhäupl, Daniel Vollprecht, Roland Pomberger, Bernd Friedrich, Karel Van Acker, et al. (2019b). "Integration of resource recovery into current waste management through (enhanced) landfill mining". In: *Detritus* 8, pp. 141–156.

Høyer, A-S, KES Klint, G Fiandaca, PK Maurya, AV Christiansen, N Balbarini, PL Bjerg, TB Hansen, and I Møller (2019). "Development of a high-resolution 3D geological model for landfill leachate risk assessment". In: *Engineering Geology* 249, pp. 45–59.

Inauen, Cornelia M, Abigail Brooks, David Caterina, Jonathan E Chambers, Ben Dashwood, Adrien Dimech, Dave A Gunn, Itzel Isunza Manrique, Oliver Neal, Xavier Piquet, et al. (2020). "Combining an integrated geophysical survey into a landfill model: A case study from Emersons Green, UK". In: *EGU General Assembly Conference Abstracts*, p. 21855.

Inzoli, Silvia, Mauro Giudici, and Johan Alexander Huisman (2016). "Estimation of sediment texture from spectral induced polarisation data using cluster and principal component analysis". In: *Near Surface Geophysics* 14.5, pp. 433–447.

Isunza Manrique, Itzel, David Caterina, Thomas Hermans, and Frederic Nguyen (2019a). "Probabilistic joint interpretation of geoelectrical and passive source seismic data for landfill characterization". In: *AGU fall meeting*.

Isunza Manrique, Itzel, David Caterina, Frederic Nguyen, and Thomas Hermans (2023). "Quantitative interpretation of geoelectric inverted data with a robust probabilistic approach". In: *Geophysics* 88.3, KS73–KS88.

Isunza Manrique, Itzel, David Caterina, Ellen Van De Vijver, Gaël Dumont, and Frederic Nguyen (2019b). "Assessment of geophysics as a characterization and monitoring tool in the dynamic landfill management (DLM) context: opportunities and challenges". In: *Sardinia Symposium 2019: the 17th International Waste Management and Landfill Symposium*. CISA Publisher.

Ivančan, Tajana Sekelj and Tena Karavidović (2021). "Archaeological Record of Iron Metallurgy Along the Drava River". In: *Interdisciplinary Research into Iron Metallurgy along the Drava River in Croatia: The TransFER Project*, p. 43.

Izydorczyk, Grzegorz, Katarzyna Mikula, Dawid Skrzypczak, Konstantinos Moustakas, Anna Witek-Krowiak, and Katarzyna Chojnacka (2021). "Potential environmental pollution from copper metallurgy and methods of management". In: *Environmental Research* 197, p. 111050.

Jacome, Maria, Vincenzo Costanzo-Alvarez, Milagrosa Aldana, Pamela Patraskovic, Chris Drielsma, Daniela Galatro, and Cristina Amon (2021). "A methodology to characterize a sanitary landfill combining, through a numerical approach, a geoelectrical survey with methane point-source concentrations". In: *Environmental Technology & Innovation* 21, p. 101225.

Jiang, Guoyan, Xuejun Qiao, Xiaoqiang Wang, Renqi Lu, Lin Liu, Hongfeng Yang, Yuanda Su, Lili Song, Baoshan Wang, and Teng-fong Wong (2020). "GPS observed horizontal ground extension at the Hutubi (China) underground gas storage facility and its application to geomechanical modeling for induced seismicity". In: *Earth and Planetary Science Letters* 530, p. 115943.

Johansson, Sara, Anders Lindskog, Gianluca Fiandaca, and Torleif Dahlin (2020). "Spectral induced polarization of limestones: time domain field data, frequency domain laboratory data and physicochemical rock properties". In: *Geophysical Journal International* 220.2, pp. 928–950.

Johansson, Sara, Charlotte Sparrenbom, Gianluca Fiandaca, Anders Lindskog, Per-Ivar Olsson, Torleif Dahlin, and Håkan Rosqvist (2017). "Investigations of a Cretaceous limestone with spectral induced polarization and scanning electron microscopy". In: *Geophysical Journal International* 208.2, pp. 954–972.

Jones, Peter Tom, Daneel Geysen, Yves Tielemans, Steven Van Passel, Yiannis Pontikes, Bart Blanpain, Mieke Quaghebeur, and Nanne Hoekstra (2013). "Enhanced Landfill Mining in view of multiple resource recovery: a critical review". In: *Journal of Cleaner Production*. Special Volume: Urban and Landfill Mining 55, pp. 45–55. ISSN: 0959-6526. DOI: 10.1016/j.jclepro.2012.05.021.

Jones, Peter Tom, Eddy Wille, and James Krook (2018). "2nd ELFM Seminar in the European Parliament: 5 Lessons Learned. Why we need to develop a broad Dynamic Landfill Management strategy and vision for Europe's 500,000 landfills". In: *Policy Brief, EU Training Network for Resource Recovery through Enhanced Landfill.(December 2018)*, pp. 1–12.

Jouen, Thomas (2018). "Caractérisation de l'évolution de l'état de biodégradation des massifs de déchets non dangereux en post-exploitation: Application de méthodes géophysiques". PhD thesis. Paris, Institut agronomique, vétérinaire et forestier de France.

Journel, AG (2002). "Combining knowledge from diverse sources: An alternative to traditional data independence hypotheses". In: *Mathematical geology* 34, pp. 573–596.

Júnior, José Tavares Araruna, Patrício José Moreira Pires, Débora Lopes Pilotto Domingues, Tácio Mauro, and Pereira de Campos (2016). "The use of ground penetrating radar in municipal solid waste landfill geotechnical investigation". In: *Journal of Civil Engineering and Architecture* 10, pp. 822–827.

Kaipio, Jari P, Ville Kolehmainen, Marko Vauhkonen, and Erkki Somersalo (1999). "Inverse problems with structural prior information". In: *Inverse problems* 15.3, p. 713.

Keller, George V (1988). "Rock and mineral properties". In: *Electromagnetic methods in applied geophysics* 1, pp. 13–52.

Kemna, Andreas (2000). *Tomographic inversion of complex resistivity: Theory and application*. Der Andere Verlag.

Kessouri, Pauline, Alexander Furman, Johan Alexander Huisman, Tina Martin, Adrian Mellage, Dimitrios Ntarlagiannis, Matthias Bücker, Solomon Ehosioke, Perrine Fernandez, Adrian Flores-Orozco, et al. (2019). "Induced polarization applied to biogeophysics: recent advances and future prospects". In: *Near Surface Geophysics* 17.6, pp. 595–621.

Kessouri, Pauline, Tim Johnson, Frederick D Day-Lewis, Chen Wang, Dimitrios Ntarlagiannis, and Lee D Slater (2022). "Post-remediation geophysical assessment: Investigating long-term electrical geophysical signatures resulting from bioremediation at a chlorinated solvent contaminated site". In: *Journal of environmental management* 302, p. 113944.

Kiberu, Johnmary (2002). "Induced Polarization and Resistivity Measurements on a Suite of Near Surface Soil Sampless and Their Empirical Relationship to Selected Measured Engineering Parameters". In: ITC.

Konstantaki, Laura Amalia, Ranajit Ghose, Deyan Draganov, Giovanni Diaferia, and Timo Heimovaara (2015). "Characterization of a heterogeneous landfill using seismic and electrical resistivity dataGeophysical characterization of a landfill". In: *Geophysics* 80.1, EN13–EN25.

Konstantaki, Laura Amalia, Ranajit Ghose, Deyan Draganov, and Timo Heimovaara (2016). "Wet and gassy zones in a municipal landfill from P-and S-wave velocity fieldsWet and gassy zones in a landfill". In: *Geophysics* 81.6, EN75–EN86.

LaBrecque, Douglas J, Michela Miletto, William Daily, Aberlardo Ramirez, and Earle Owen (1996). "The effects of noise on Occam's inversion of resistivity tomography data". In: *Geophysics* 61.2, pp. 538–548.

Lévy, L, PK Maurya, Svetlana Byrdina, Jean Vandemeulebrouck, Freysteinn Sigmundsson, Knútur Árnason, Tullio Ricci, Damien Deldicque, M Roger, Benoit Gibert, et al. (2019). "Electrical resistivity tomography and time-domain induced polarization field investigations of geothermal areas at Krafla, Iceland: comparison to borehole and laboratory frequency-domain electrical observations". In: *Geophysical Journal International* 218.3, pp. 1469–1489.

Linde, Niklas, David Ginsbourger, James Irving, Fabio Nobile, and Arnaud Doucet (2017). "On uncertainty quantification in hydrogeology and hydrogeophysics". In: *Advances in Water Resources* 110, pp. 166–181.

Linde, Niklas, Philippe Renard, Tapan Mukerji, and Jef Caers (2015). "Geological realism in hydrogeological and geophysical inverse modeling: A review". In: *Advances in Water Resources* 86, pp. 86–101.

Lionheart, William RB (2004). "EIT reconstruction algorithms: pitfalls, challenges and recent developments". In: *Physiological measurement* 25.1, p. 125.

Liu, Lu, Yujin Liu, Tao Li, Yi He, Yue Du, and Yi Luo (2021). "Inversion of vehicle-induced signals based on seismic interferometry and recurrent neural networksInversion of vehicle-induced signals". In: *Geophysics* 86.3, Q37–Q45.

Loke, Meng Heng (1997). "Res2DINV software user's manual". In: *University Sains Malaysia, Penang*.

— (2003). "Rapid 2D Resistivity & IP Inversion using the least-squares method". In: *Geotomo Software. Manual*.

— (2004). "Tutorial: 2-D and 3-D electrical imaging surveys". In.

Lopez-Alvis, Jorge, Eric Laloy, Frédéric Nguyen, and Thomas Hermans (2021). "Deep generative models in inversion: The impact of the generator's nonlinearity and development of a new approach based on a variational autoencoder". In: *Computers & Geosciences* 152, p. 104762.

Lopez-Alvis, Jorge, Frederic Nguyen, MC Looms, and Thomas Hermans (2022). "Geophysical inversion using a variational autoencoder to model an assembled spatial prior uncertainty". In: *Journal of Geophysical Research: Solid Earth* 127.3, e2021JB022581.

Lysdahl, Asgeir Kydland, Craig William Christensen, Andreas Aspmo Pfaffhuber, Malte Vöge, Lars Andresen, Guro Huun Skurdal, and Martin Panzner (2022). "Integrated bedrock model combining airborne geophysics and sparse drillings based on an artificial neural network". In: *Engineering Geology* 297, p. 106484.

Machiels, Lieven, Mika Paajanen, Peter Tom Jones, Päivi Kinnunen, and Koen Binnemans (2022). "Near-zero-waste recycling of low-grade sulphidic mining waste for critical-metal, mineral and construction raw-material production in a circular economy". In.

Magiera, Tadeusz, Bogdan Żogała, Marcin Szuszkiewicz, Jolanta Pierwoła, and Maria Magdalena Szuszkiewicz (2019). "Combination of different geophysical techniques for the location of historical waste in the Izery Mountains (SW Poland)". In: *Science of the Total Environment* 682, pp. 226–238.

Mao, Deqiang, André Revil, and John Hinton (2016). "Induced polarization response of porous media with metallic particles—Part 4: Detection of metallic and nonmetallic targets in time-domain-induced polarization tomographySandbox experiments of IP". In: *Geophysics* 81.4, pp. D359–D375.

Martin, Tina, Thomas Günther, Andreas Weller, and Kerstin Kuhn (2021). "Classification of slag material by spectral induced polarization laboratory and field measurements". In: *Journal of Applied Geophysics* 194, p. 104439.

Martin, Tina, Kerstin Kuhn, Thomas Günther, and Rudolf Kniess (2020). "Geophysical exploration of a historical stamp mill dump for the volume estimation of valuable residues". In: *Journal of Environmental and Engineering Geophysics* 25.2, pp. 275–286.

Martin, Tina, Andreas Weller, and Laura Behling (2022). "Desaturation effects of pyrite–sand mixtures on induced polarization signals". In: *Geophysical Journal International* 228.1, pp. 275–290.

Martínez, Julián, Javier Rey, Senén Sandoval, Mª Camen Hidalgo, and Rosendo Mendoza (2019). "Geophysical prospecting using ERT and IP techniques to locate Galena veins". In: *Remote Sensing* 11.24, p. 2923.

Martínez-Segura, Marcos A, Marco D Vásconez-Maza, and María C García-Nieto (2020). "Volumetric characterisation of waste deposits generated during the production of fertiliser derived from phosphoric rock by using LiDAR and electrical resistivity tomography". In: *Science of The Total Environment* 716, p. 137076.

Maurya, PK, VK Rønde, G Fiandaca, Nicola Balbarini, E Auken, Poul Løgstrup Bjerg, and AV Christiansen (2017). "Detailed landfill leachate plume mapping using 2D and 3D electrical resistivity tomography-with correlation to ionic strength measured in screens". In: *Journal of Applied Geophysics* 138, pp. 1–8.

Memon, Mushtaq Ahmed (2010). "Integrated solid waste management based on the 3R approach". In: *Journal of Material Cycles and Waste Management* 12, pp. 30–40.

Mendecki, Maciej J, Rafał Warchulski, Monika Szczuka, Dorota Środek, and Jolanta Pierwoła (2020). "Geophysical and petrological studies of the former lead smelting waste dump in Sławków, Poland". In: *Journal of Applied Geophysics* 179, p. 104080.

Menke, William (2018). *Geophysical data analysis: Discrete inverse theory*. Academic press.

Miao, Lei, Gangqing Yang, Tao Tao, and Yongzhen Peng (2019). "Recent advances in nitrogen removal from landfill leachate using biological treatments–A review". In: *Journal of environmental management* 235, pp. 178–185.

Mirecki, June E and William S Parks (1994). "Leachate geochemistry at a municipal landfill, Memphis, Tennessee". In: *Groundwater* 32.3, pp. 390–398.

Misra, S, C Torres-Verdín, A Revil, J Rasmus, and D Homan (2016). "Interfacial polarization of disseminated conductive minerals in absence of redox-active species—Part 1: Mechanistic model and validationInterfacial polarization of conductive inclusions". In: *Geophysics* 81.2, E139–E157.

Moghadas, Davood and Annika Badorreck (2019). "Machine learning to estimate soil moisture from geophysical measurements of electrical conductivity". In: *Near Surface Geophysics* 17.2, pp. 181–195.

Mollaret, Coline, Florian M Wagner, Christin Hilbich, Cristian Scapozza, and Christian Hauck (2020). "Petrophysical joint inversion applied to alpine permafrost field sites to image subsurface ice, water, air, and rock contents". In: *Frontiers in Earth Science* 8, p. 85.

Moreau, Sylvain, M Bergeron, and Rémi Clement (2012). "Evolution of electrical resistivity measurements during process of waste biodegradation". In: *Near Surface Geoscience 2012–18th European Meeting of Environmental and Engineering Geophysics*. EAGE Publications BV, cp–306.

Moreau, Sylvain, Thomas Jouen, Julien Grossin-Debattista, Simon Loisel, Laurent Mazéas, and Rémi Clément (2019). "Six years temperature monitoring using fibre-optic sensors in a bioreactor landfill". In: *Geosciences* 9.10, p. 426.

Moreira, César Augusto, Evandro Gomes Dos Santos, Lenon Melo Ilha, and Renata Paes (2019). "Recognition of sulfides zones in Marble Mine through comparative analysis of electrical tomography arrangements". In: *Pure and Applied Geophysics* 176, pp. 4907–4920.

Moreira, César Augusto, Lívia Portes Innocenti Helene, Paulo Nogara, and Lenon Melo Ilha (2018). "Analysis of leaks from geomembrane in a sanitary landfill through models of electrical resistivity tomography in South Brazil". In: *Environmental earth sciences* 77, pp. 1–9.

Mutafela, Richard Nasilele, Etzar Gomez Lopez, Torleif Dahlin, Fabio Kaczala, Marcia Marques, Yahya Jani, and William Hogland (2020). "Geophysical investigation of glass 'hotspots' in glass dumps as potential secondary raw material sources". In: *Waste management* 106, pp. 213–225.

Naudet, V, A Revil, J-Y Bottero, and P Bégassat (2003). "Relationship between self-potential (SP) signals and redox conditions in contaminated groundwater". In: *Geophysical research letters* 30.21.

Naudet, Véronique, Jean-Christophe Gourry, Jean-François Girard, and Jacques Deparis (2012). "Geoelectrical characterization of the internal structure and biodegradation of an old Municipal Solid Waste". In: *Second Workshop on geophysical measurements at landfills*.

Neculau, Claudia, Renaud De Rijdt, Eddy Wille, and RAWFILL Team (2019). "RAWFILL PROJECT: INNOVATIVE CHARACTERIZATION OF LANDFILLS AND SMART DECISION-MAKING AS PART OF THE CIRCULAR ECONOMY, THROUGH LANDFILL MINING OPERATIONS". In: *Sardinia Symposium 2019: the 17th International Waste Management and Landfill Symposium*. CISA Publisher.

Neyamadpour, Ahmad (2019). "3D monitoring of volumetric water content using electrical resistivity tomography in municipal solid waste landfill". In: *Environmental Earth Sciences* 78.14, p. 426.

Nguyen, Frédéric, Ranajit Ghose, Itzel Isunza Manrique, Tanguy Robert, and Gael Dumont (2018). "Managing past landfills for future site development: A review of the contribution of geophysical methods". In: *4th International Symposium on Enhanced Landfill Mining*.

Nguyen, Frederic, Andreas Kemna, Tanguy Robert, and Thomas Hermans (2016). "Data-driven selection of the minimum-gradient support parameter in time-lapse focused electric imaging". In: *Geophysics* 81.1, A1–A5.

Oldenburg, Douglas W and Yaoguo Li (1994). "Inversion of induced polarization data". In: *Geophysics* 59.9, pp. 1327–1341.

Orozco, Adrián Flores, Andreas Kemna, and Egon Zimmermann (2012). "Data error quantification in spectral induced polarization imaging". In: *Geophysics* 77.3, E227–E237.

Paasche, Hendrik, Jens Tronicke, Klaus Holliger, Alan G Green, and Hansruedi Maurer (2006). "Integration of diverse physical-property models: Subsurface zonation and petrophysical parameter estimation based on fuzzy c-means cluster analyses". In: *Geophysics* 71.3, H33–H44.

Parsekian, Andrew D, Dario Grana, Felipe dos Anjos Neves, Mark S Pleasants, Mark Seyfried, Bryan G Moravec, Jon Chorover, Anthony M Moraes, Natalie Y Smeltz, John H Westenhoff, et al. (2021). "Hydrogeophysical comparison of hillslope critical zone architecture for different geologic substrates". In: *Geophysics* 86.5, WB29–WB49.

Pedregosa, Fabian, Gaël Varoquaux, Alexandre Gramfort, Vincent Michel, Bertrand Thirion, Olivier Grisel, Mathieu Blondel, Peter Prettenhofer, Ron Weiss, Vincent Dubourg, et al. (2011). "Scikit-learn: Machine learning in Python". In: *the Journal of machine Learning research* 12, pp. 2825–2830.

Pelton, W Hallof, SH Ward, PG Hallof, WR Sill, and P Hi Nelson (1978). "Mineral discrimination and removal of inductive coupling with multifrequency IP". In: *Geophysics* 43.3, pp. 588–609.

Piana Agostinetti, Nicola and Thomas Bodin (2018). "Flexible coupling in joint inversions: a Bayesian structure decoupling algorithm". In: *Journal of Geophysical Research: Solid Earth* 123.10, pp. 8798–8826.

Piegari, Ester, Giorgio De Donno, Davide Melegari, and Valeria Paoletti (2023). "A machine learning-based approach for mapping leachate contamination using geoelectrical methods". In: *Waste Management* 157, pp. 121–129.

Pierwoła, Jolanta, Marcin Szuszkiewicz, Jerzy Cabala, Krzysztof Jochymczyk, Bogdan Żogała, and Tadeusz Magiera (2020). "Integrated geophysical and geochemical methods applied for recognition of acid waste drainage (AWD) from Zn-Pb post-flotation tailing pile (Olkusz, southern Poland)". In: *Environmental Science and Pollution Research* 27, pp. 16731–16744.

Placencia-Gómez, Edmundo, Annika Parviainen, Lee Slater, and Jussi Leveinen (2015). "Spectral induced polarization (SIP) response of mine tailings". In: *Journal of Contaminant Hydrology* 173, pp. 8–24.

Potdar, Kedar, Taher S Pardawala, and Chinmay D Pai (2017). "A comparative study of categorical variable encoding techniques for neural network classifiers". In: *International journal of computer applications* 175.4, pp. 7–9.

Qi, Youzheng, Abdellahi Soueid Ahmed, André Revil, Ahmad Ghorbani, Feras Abdulsamad, Nicolas Florsch, and Jeremy Bonnenfant (2018). "Induced polarization response of porous media with metallic particles—Part 7: Detection and quantification of buried slag heaps". In: *Geophysics* 83.5, E277–E291.

Qiao, Chunyu, Mehdi Khanzadeh Moradllo, Hope Hall, M Tyler Ley, and W Jason Weiss (2019). "Electrical resistivity and formation factor of air-entrained concrete". In: *ACI Materials Journal* 116.3, pp. 85–93.

RAWFILL (2020). *Landfill characterization: the landfill of Onoz (Wallonia, Belgium)*. https://vb.nweurope.eu/media/10049/onoz_draft_website-version.pdf.

Ray, Anandaroop, Sam Kaplan, John Washbourne, and Uwe Albertin (2018). "Low frequency full waveform seismic inversion within a tree based Bayesian framework". In: *Geophysical Journal International* 212.1, pp. 522–542.

Revil, A and Nicolas Florsch (2010). "Determination of permeability from spectral induced polarization in granular media". In: *Geophysical Journal International* 181.3, pp. 1480–1498.

Revil, André, Nicolas Florsch, and Deqiang Mao (2015). "Induced polarization response of porous media with metallic particles—Part 1: A theory for disseminated semiconductors". In: *Geophysics* 80.5, pp. D525–D538.

Revil, André, Pierre Vaudelet, Zhaoyang Su, and Rujun Chen (2022). "Induced polarization as a tool to assess mineral deposits: A review". In: *Minerals* 12.5, p. 571.

Rey, J, J Martínez, M Hidalgo, R Mendoza, and S Sandoval (2020). "Assessment of tailings ponds by a combination of electrical (ERT and ip) and hydrochemical techniques (linares, Southern Spain)". In: *Mine Water Environ* 40, pp. 298–307.

Reynolds, John M (2011). *An introduction to applied and environmental geophysics*. John Wiley & Sons.

Robert, Tanguy, Alain Dassargues, Serge Brouyère, Olivier Kaufmann, Vincent Hallet, and Frédéric Nguyen (2011). "Assessing the contribution of electrical resistivity tomography (ERT) and self-potential (SP) methods for a water well drilling program in fractured/karstified limestones". In: *Journal of Applied Geophysics* 75.1, pp. 42–53.

Romero-Ruiz, Alejandro, Niklas Linde, Thomas Keller, and Dani Or (2018). "A review of geophysical methods for soil structure characterization". In: *Reviews of Geophysics* 56.4, pp. 672–697.

Ronczka, Mathias, Thomas Voß, and Thomas Günther (2015). "Cost-efficient imaging and monitoring of saltwater in a shallow aquifer by using long electrode ERT". In: *Journal of Applied Geophysics* 122, pp. 202–209.

Rücker, Carsten, Thomas Günther, and Florian M Wagner (2017). "pyGIMLi: An open-source library for modelling and inversion in geophysics". In: *Computers & Geosciences* 109, pp. 106–123.

Rucker, Dale F, Nigel Crook, Jeffrey Winterton, Michael McNeill, Chris A Baldyga, Gillian Noonan, and James B Fink (2014). "Real-time electrical monitoring of reagent delivery during a subsurface amendment experiment". In: *Near Surface Geophysics* 12.1, pp. 151–163.

Rucker, Dale F, Michael McNeill, Al Schindler, and Gillian Noonan (2009). "Monitoring of a secondary recovery application of leachate injection into a heap". In: *Hydrometallurgy* 99.3-4, pp. 238–248.

Sabor, Kawtar, Damien Jougnot, Roger Guerin, Barthélémy Steck, Jean-Marie Henault, Louis Apffel, and Denis Vautrin (2021). "A data mining approach for improved interpretation of ERT inverted sections using the DBSCAN clustering algorithm". In: *Geophysical Journal International* 225.2, pp. 1304–1318.

Saneiyan, Sina, Dimitrios Ntarlagiannis, Juliette Ohan, Junghwoon Lee, Frederick Colwell, and Susan Burns (2019). "Induced polarization as a monitoring tool for

in-situ microbial induced carbonate precipitation (MICP) processes". In: *Ecological engineering* 127, pp. 36–47.

Sauve, Giovanna and Karel Van Acker (2020). "The environmental impacts of municipal solid waste landfills in Europe: A life cycle assessment of proper reference cases to support decision making". In: *Journal of environmental management* 261, p. 110216.

Scheidt, Céline, Lewis Li, and Jef Caers (2018). *Quantifying uncertainty in subsurface systems*. Vol. 236. John Wiley & Sons.

Sciarra, A., B. Cantucci, V. Sapia, R. De Ritis, T. Ricci, R. Civico, G. Galli, D. Cinti, and M. Coltorti (2021). "Geochemical and geoelectrical characterization of the Terre Calde di Medolla (Emilia-Romagna, northern Italy) and relations with 2012 seismic sequence". In: *Journal of Geochemical Exploration* 221, p. 106678. ISSN: 0375-6742. DOI: 10.1016/j.gexplo.2020.106678.

Scott, David W (2015). *Multivariate density estimation: theory, practice, and visualization*. John Wiley & Sons.

Seigel, Harold O (1959). "Mathematical formulation and type curves for induced polarization". In: *Geophysics* 24.3, pp. 547–565.

Sethurajan, Manivannan, Eric D van Hullebusch, and Yarlagadda V Nancharaiah (2018). "Biotechnology in the management and resource recovery from metal bearing solid wastes: Recent advances". In: *Journal of Environmental Management* 211, pp. 138–153.

Shen, Siliang, Yunmin Chen, Liangtong Zhan, Haijian Xie, Abdelmalek Bouazza, Feiyu He, and Xinru Zuo (2018). "Methane hotspot localization and visualization at a large-scale Xi'an landfill in China: effective tool for landfill gas management". In: *Journal of environmental management* 225, pp. 232–241.

Slater, Lee, AM Binley, William Daily, and Richard Johnson (2000). "Cross-hole electrical imaging of a controlled saline tracer injection". In: *Journal of applied geophysics* 44.2-3, pp. 85–102.

Slater, Lee and Andrew Binley (2021). "Advancing hydrological process understanding from long-term resistivity monitoring systems". In: *Wiley Interdisciplinary Reviews: Water* 8.3, e1513.

Slater, Lee, Dimitrios Ntarlagiannis, Yves R Personna, and Susan Hubbard (2007). "Pore-scale spectral induced polarization signatures associated with FeS biomineral transformations". In: *Geophysical Research Letters* 34.21.

Soupios, Pantelis and Dimitrios Ntarlagiannis (2017). "Characterization and monitoring of solid waste disposal sites using geophysical methods: Current applications and novel trends". In: *Modelling trends in solid and hazardous waste management*, pp. 75–103.

Sun, Huaifeng, Ming Cheng, Chuanxi Su, Haiyan Li, Guodong Zhao, Maoxin Su, Shucai Li, Bo Zhang, Lewen Zhang, and Kai Li (2017). "Characterization of shallow karst using electrical resistivity imaging in a limestone mining area". In: *Environmental earth sciences* 76, pp. 1–9.

Sun, Xiaochen, Xu Qian, Changxin Nai, Ya Xu, Yuqiang Liu, Guangyuan Yao, and Lu Dong (2023). "LDI-MVFNet: A Multi-view fusion deep network for leachate distribution imaging". In: *Waste Management* 157, pp. 180–189.

Tal, Adi, Yishai Weinstein, Matthieu Baïsset, Arik Golan, and Yoseph Yechieli (2019). "High resolution monitoring of seawater intrusion in a multi-aquifer system-implementation of a new downhole geophysical tool". In: *Water* 11.9, p. 1877.

Telford, William Murray, Lloyd P Geldart, and Robert E Sheriff (1990). *Applied geophysics*. Cambridge university press.

TerrameterLS2 (2016). *User Manual Terrameter LS2*. English. ABEM-MALA. 126 pp. Forthcoming.

Thibaut, Robin, Thomas Kremer, Annie Royen, Bun Kim Ngun, Frédéric Nguyen, and Thomas Hermans (2021). "A new workflow to incorporate prior information in minimum gradient support (MGS) inversion of electrical resistivity and induced polarization data". In: *Journal of Applied Geophysics* 187, p. 104286.

Van De Vijver, Ellen, Christin Bobe, Daan Hanssens, Philippe De Smedt, and Marc Van Meirvenne (2019). "Representative sampling of landfills: a robust procedure for selecting trench locations based on electromagnetic induction survey data". In: *AGU Fall Meeting Abstracts*. Vol. 2019, NS24A–06.

Van De Vijver, Ellen, David Caterina, Itzel Isunza Manrique, Christin Bobe, and Frédéric Nguyen (2020). "Geophysical surveys for unlocking landfill resources: from past applications to future developments". In: *AGU fall meeting*.

Van De Vijver, Ellen, Itzel Isunza Manrique, Christin Bobe, David Caterina, Thomas Hermans, Eddy Wille, and Frédéric Nguyen (2021). "Geophysics in support of dynamic landfill management: Moving beyond the challenges". In: *SEG/AAPG/SEPM First International Meeting for Applied Geoscience & Energy*. OnePetro.

Van Hoorde, Maurits, Thomas Hermans, Gaël Dumont, and Frédéric Nguyen (2017). "3D electrical resistivity tomography of karstified formations using cross-line measurements". In: *Engineering geology* 220, pp. 123–132.

Vareda, João P, Artur JM Valente, and Luisa Durães (2019). "Assessment of heavy metal pollution from anthropogenic activities and remediation strategies: A review". In: *Journal of environmental management* 246, pp. 101–118.

Vásconez-Maza, Marco D, María C Bueso, Angel Faz, JA Acosta, and Marcos A Martínez-Segura (2021). "Assessing the behaviour of heavy metals in abandoned

phosphogypsum deposits combining electrical resistivity tomography and multivariate analysis". In: *Journal of Environmental Management* 278, p. 111517.

Vásconez-Maza, Marco D, Marcos A Martínez-Segura, María C Bueso, Ángel Faz, M Cristina Garcia-Nieto, María Gabarrón, and José A Acosta (2019). "Predicting spatial distribution of heavy metals in an abandoned phosphogypsum pond combining geochemistry, electrical resistivity tomography and statistical methods". In: *Journal of hazardous materials* 374, pp. 392–400.

Virtanen, Pauli, Ralf Gommers, Travis E Oliphant, Matt Haberland, Tyler Reddy, David Cournapeau, Evgeni Burovski, Pearu Peterson, Warren Weckesser, Jonathan Bright, et al. (2020). "SciPy 1.0: fundamental algorithms for scientific computing in Python". In: *Nature methods* 17.3, pp. 261–272.

Vollprecht, Daniel, Christin Bobe, Roman Stiegler, Ellen Van De Vijver, Tanja Wolfsberger, Bastian Küppers, and Robert Scholger (2019). "Relating magnetic properties of municipal solid waste constituents to iron content: implications for enhanced landfill mining". In: *Detritus* 8, pp. 31–46.

Vollprecht, Daniel, Lieven Machiels, and Peter Tom Jones (2021). "The EU training network for resource recovery through enhanced landfill mining—a review". In: *Processes* 9.2, p. 394.

Wagner, Florian M. and Bernd U. Wiese (2018). "Fully coupled inversion on a multiphysical reservoir model – Part II: The Ketzin CO2 storage reservoir". In: *International Journal of Greenhouse Gas Control* 75, pp. 273–281. ISSN: 1750-5836. DOI: 10.1016/j.ijggc.2018.04.009.

Wang, Jie, Xiaopei Zhang, and Lizhi Du (2017). "A laboratory study of the correlation between the thermal conductivity and electrical resistivity of soil". In: *Journal of Applied Geophysics* 145, pp. 12–16.

Wang, Zhen, Haibin Di, Muhammad Amir Shafiq, Yazeed Alaudah, and Ghassan AlRegib (2018). "Successful leveraging of image processing and machine learning in seismic structural interpretation: A review". In: *The Leading Edge* 37.6, pp. 451–461.

Wellmann, J. Florian, Miguel de la Varga, Ruth E. Murdie, Klaus Gessner, and Mark Jessell (2018). "Uncertainty estimation for a geological model of the Sandstone greenstone belt, Western Australia – insights from integrated geological and geophysical inversion in a Bayesian inference framework". In: *Geological Society, London, Special Publications* 453.1. Publisher: Geological Society of London Section: Development of more rigorous 3D Earth models, pp. 41–56. DOI: 10.1144/SP453.12.

Whiteley, JS, JE Chambers, Sebastian Uhlemann, Paul B Wilkinson, and JM Kendall (2019). "Geophysical monitoring of moisture-induced landslides: A review". In: *Reviews of Geophysics* 57.1, pp. 106–145.

Whiteley, JS, A Watlet, S Uhlemann, P Wilkinson, JP Boyd, C Jordan, JM Kendall, and JE Chambers (2021). "Rapid characterisation of landslide heterogeneity using unsupervised classification of electrical resistivity and seismic refraction surveys". In: *Engineering Geology* 290, p. 106189.

Wijesekara, SSRMDHR, Sonia S Mayakaduwa, AR Siriwardana, Nalin De Silva, BFA Basnayake, Ken Kawamoto, and Meththika Vithanage (2014). "Fate and transport of pollutants through a municipal solid waste landfill leachate in Sri Lanka". In: *Environmental earth sciences* 72, pp. 1707–1719.

Williams, Christopher KI and David Barber (1998). "Bayesian classification with Gaussian processes". In: *IEEE Transactions on pattern analysis and machine intelligence* 20.12, pp. 1342–1351.

Williams, Paul T (2005). *Waste treatment and disposal*. John Wiley & Sons.

Wong, J (1979). "An electrochemical model of the induced-polarization phenomenon in disseminated sulfide ores". In: *Geophysics* 44.7, pp. 1245–1265.

Wong, J and DW Strangway (1981). "Induced polarization in disseminated sulfide ores containing elongated mineralization". In: *Geophysics* 46.9, pp. 1258–1268.

Yannah, Mero, Kristine Martens, Marc Van Camp, and Kristine Walraevens (2017). "Geophysical exploration of an old dumpsite in the perspective of enhanced landfill mining in Kermt area, Belgium". In: *Bulletin of Engineering Geology and the Environment* 78, pp. 55–67.

Yin, Ke, Huanhuan Tong, Apostolos Giannis, Jing-Yuan Wang, and Victor W-C Chang (2017). "Multiple geophysical surveys for old landfill monitoring in Singapore". In: *Environmental monitoring and assessment* 189, pp. 1–13.

Yu, Hao, Guoxiong Chen, and Hanming Gu (2020). "A machine learning methodology for multivariate pore-pressure prediction". In: *Computers & Geosciences* 143, p. 104548.

Yu, Siwei and Jianwei Ma (2021). "Deep learning for geophysics: Current and future trends". In: *Reviews of Geophysics* 59.3, e2021RG000742.

Zhan, Liang-tong, Hui Xu, Xiao-ming Jiang, Ji-wu Lan, Yun-min Chen, and Zhenying Zhang (2019). "Use of electrical resistivity tomography for detecting the distribution of leachate and gas in a large-scale MSW landfill cell". In: *Environmental Science and Pollution Research* 26, pp. 20325–20343.

Zhang, Yangxi, Lifei Wei, Qikai Lu, Yanfei Zhong, Ziran Yuan, Zhengxiang Wang, Zhongqiang Li, and Yujing Yang (2023). "Mapping soil available copper content

in the mine tailings pond with combined simulated annealing deep neural network and UAV hyperspectral images". In: *Environmental Pollution*, p. 120962.

Žibret, Gorazd, Bruno Lemiere, Ana-Maria Mendez, Carlo Cormio, Danielle Sinnett, Peter Cleall, Katalin Szabó, and M Teresa Carvalho (2020). "National mineral waste databases as an information source for assessing material recovery potential from mine waste, tailings and metallurgical waste". In: *Minerals* 10.5, p. 446.

Zimmermann, E, JA Huisman, A Kemna, J Berwix, W Glaas, H Meier, B Wolters, and O Esser (2010). "Advanced electrical impedance tomography system with high phase accuracy". In: *Proceedings of the 6th World Congress on industrial process tomography (WCIPT6), Beijing, China*, pp. 583–591.

Zimmermann, E, A Kemna, J Berwix, W Glaas, HM Münch, and JA Huisman (2008). "A high-accuracy impedance spectrometer for measuring sediments with low polarizability". In: *Measurement Science and Technology* 19.10, p. 105603.